



### Advances in Solar Evaporator Materials for Freshwater Generation

Journal:	<i>Journal of Materials Chemistry A</i>
Manuscript ID	TA-REV-06-2019-006034.R1
Article Type:	Review Article
Date Submitted by the Author:	16-Aug-2019
Complete List of Authors:	<p>Cao, Sisi; Washington University, Department of Mechanical Aerospace and Structural Engineering          Jiang, Qisheng; Washington University, Department of Mechanical Aerospace and Structural Engineering          Wu, Xuanhao; Washington University in Saint Louis, Energy, Environmental &amp; Chemical Engineering          Ghim, Deoukchen; Washington University,          Derami, Hamed; Washington University, Department of Mechanical Aerospace and Structural Engineering          Chou, Ping I; Washington University in Saint Louis, Energy, Environmental &amp; Chemical Engineering          Jun, Young-Shin; Washington University, Energy, Environment and Chemical Engineering          Singamaneni, Srikanth; Washington University, Department of Mechanical Aerospace and Structural Engineering</p>

# Advances in Solar Evaporator Materials for Freshwater Generation

Sisi Cao,<sup>1</sup> Qisheng Jiang,<sup>1</sup> Xuanhao Wu,<sup>2</sup> Deoukchen Ghim,<sup>2</sup> Hamed Gholami Derami,<sup>1</sup> Ping I  
Chou,<sup>2</sup> Young-Shin Jun,<sup>\*2</sup> Srikanth Singamaneni<sup>\*1</sup>

<sup>1</sup>*Department of Mechanical Engineering and Materials Science, Institute of Materials  
Science and Engineering, Washington University in St. Louis, St. Louis, Missouri 63130,  
United States*

<sup>2</sup>*Department of Energy, Environmental and Chemical Engineering, Washington  
University in St. Louis, Saint Louis, Missouri 63130, United States*

## Abstract

To alleviate the scarcity of clean water, solar steam generation, which utilizes the green and abundant resources of the Earth, has attracted considerable attention and been recognized as a sustainable technology to purify seawater and wastewater. Within the past five to seven years, building on remarkable advances in the synthesis of nanoscale photothermal materials, significant progress has been made in the design and fabrication of solar evaporators. Here, we comprehensively review the materials and structures of the three key components of solar evaporators: solar absorbers, substrates (*i.e.*, support layers), and water collectors, towards efficient harvesting of sunlight, thermal management, and water transportation, interfacial evaporation, and collection. In particular, we discuss the design principles of water collectors for solar-driven evaporation, which are in early stages of development at present. Furthermore, bio-inspired water collectors provide exciting opportunities for the design and realization of efficient water harvesting from solar steam. Finally, we introduce photothermal-enhanced membrane distillation (PMD), a promising alternate technique involving solar-driven interfacial evaporation for producing clean water. PMD combines solar energy and membrane distillation, which facilitates efficient water purification and collection. In this review, we discussed the design guidelines and recent development of this solar-driven water purification. This review provides

26 useful insights into the materials choice and structure optimization to realize enhanced solar  
27 evaporators towards freshwater generation.

28 \*To whom correspondence should be addressed: [ysjun@wustl.edu](mailto:ysjun@wustl.edu)(YJ) and  
29 [singamaneni@wustl.edu](mailto:singamaneni@wustl.edu) (SS).

## 30        **1. Introduction**

31        Although 70% of Earth's surface is covered with water, only 3% of it is freshwater.<sup>1-3</sup> According to  
32        a 2019 report from World Wildlife Fund, 1.1 billion people worldwide have limited access to fresh  
33        water, and 2.4 billion people are exposed to water-borne diseases, which are closely related to  
34        inadequate sanitation.<sup>4</sup> The scarcity of freshwater is one of biggest threats to the sustained growth  
35        of the world economy, and the situation has been exacerbated by the environmental pollution,  
36        agriculture and population growth, and socioeconomic development. In response, by 2018, more  
37        than 20,000 water desalination plants had been constructed all over the world, which can  
38        generate 104.7 million m<sup>3</sup> water every day.<sup>5, 6</sup> Current technologies for water purification include  
39        reverse osmosis (RO)<sup>7-10</sup>, electrodialysis<sup>11, 12</sup>, thermal distillation via heating bulk water, and  
40        membrane distillation (MD).<sup>13-15</sup> However, most of these involve high energy consumption, which  
41        increases the emission of greenhouse gases.

42               To meet the pressing need for fresh water at minimal energy cost, solar steam generation  
43        has been proposed and its application in water desalination has been widely investigated in recent  
44        years (Figure 1). More than 2000 years ago, the Greek philosopher Aristotle presented the idea  
45        of using solar energy to evaporate saline water and obtaining freshwater by condensing the  
46        generated vapor.<sup>16</sup> Because it is powered by an abundant and economically friendly resource,  
47        solar evaporation does not have harmful effects on the environment. Moreover, recent advances  
48        in nanoscale photothermal materials, which can effectively capture sunlight and convert light to  
49        heat, make solar-assisted evaporation one of most appealing technologies for purifying seawater  
50        or wastewater. Further, significant progress in novel evaporator designs has led to solar  
51        evaporators whose efficiency exceeds 90% when combined with highly efficient photothermal  
52        materials. Traditionally, solar evaporation has involved dispersing solar absorbers into the bulk  
53        water for volumetric heating. Due to the significant heat loss associated with this approach,<sup>17-19</sup>  
54        interfacial heating by confining solar absorbers to the air/water interface was proposed in the early

55 2010s to improve the solar evaporation efficiency.<sup>20</sup> A typical double-layer interfacial solar  
56 evaporator comprises a solar absorber layer and a supporting substrate.<sup>21, 22</sup> Under solar  
57 irradiation, the solar absorber layer converts the light to heat that increases the surface  
58 temperature. Bulk water is continuously pumped up to contact hot surface via water pathways  
59 within the substrate through capillary force and evaporation takes place at the confined high  
60 temperature zone. Apart from transporting water, the substrate also acts as a thermal barrier to  
61 reduce the heat conduction loss from the solar absorber layer to the underlying bulk water,  
62 significantly increasing the evaporation efficiency. Finally, water is harvested by condensing the  
63 vapor, coalescing water droplets and transporting the water droplets for collection.

64 Evaporation efficiency, a critical criterion for evaluating the performance of a solar  
65 evaporator, is defined as the ratio of the thermal energy stored in the generated vapor to the total  
66 energy of the irradiating light,  $\eta = \frac{\dot{m}h_{LV}}{Q_s A}$ , where  $\dot{m}$  represents the evaporation flux of water,  $h_{LV}$  refers  
67 to total evaporation enthalpy change, which includes sensible heat and phase change from liquid  
68 to vapor,  $Q_s$  is the power density of the light irradiation, and  $A$  is the illuminated area.<sup>23</sup> Three  
69 important factors affect the evaporation efficiency,  $\eta$ : solar light absorption, thermal management,  
70 and water transportation. In the past few years, significant efforts have been dedicated to  
71 designing and realizing advanced materials and optimal evaporator designs to maximize  
72 evaporation efficiency. In this context, photothermal materials are designed to achieve broadband  
73 absorption of sunlight, and efficient conversion of the light into heat. In addition, the supporting  
74 substrate is designed to minimize heat dissipation from the photothermal layer to the bulk water,  
75 to maintain high temperature at the evaporative surface, and simultaneously to supply adequate  
76 water for evaporation.

77 Herein, we review recent developments in materials design, synthesis and engineering of  
78 three key components of solar evaporators: solar absorbers, substrates, and water collectors  
79 (Figure 2). We present guidelines for materials selection and interfacial evaporator design for

80 achieving highly efficient solar light harvesting, optimal thermal management, and high water  
81 transportation, all ultimately leading to high evaporation efficiencies. We also discuss the structure,  
82 surface, and interfacial aspects of water collectors that are critical to harvest the evaporated water.  
83 Firstly, we explore and compare various kinds of solar absorbers, classified by their different  
84 photothermal mechanisms. The structure designs of these photothermal materials to maximize  
85 light absorption and produce thermal energy are discussed. Then, we outline the design principles  
86 for substrates to provide thermal confinement and supply water to the solar absorber layer.  
87 Different types of substrate materials with low thermal conductivity and interconnected porous  
88 structure are presented, and advanced configurations are introduced, including 1D/2D water  
89 pathway structures and salt-rejection systems. We highlight the importance of the efficient  
90 collection of water from the steam produced by the interfacial evaporator. In particular, we point  
91 out various extraordinary water collectors in nature and discuss corresponding bio-inspired water  
92 collectors for highly efficient water harvesting in solar evaporators. Finally, we discuss  
93 photothermal membrane distillation, which enables facile water harvesting.

## 94 **2. Materials selection for solar absorbers and substrates**

95 For past decades, the performance of solar evaporator has been significantly improved by the  
96 advancement in materials science of solar absorbers and supporting substrates. Numerous  
97 efforts have been made to develop new materials and engineer the existing materials. Various  
98 solar absorbers are explored to achieve high light absorption and thermal energy harvesting.  
99 Simultaneously, new substrates were investigated to achieve efficient thermal management and  
100 water transportation. In what follows, we focus on the principles and strategies of materials  
101 selection of solar absorbers and substrates for realizing interfacial evaporators with high  
102 evaporation efficiency.

## 103            **2.1. Solar absorbers**

104    The photothermal effect describes a direct energy conversion process where light energy incident  
105    on a material is transformed to thermal energy (heat).<sup>24, 25</sup> Upon sunlight illumination,  
106    photothermal materials can absorb the photons and photoexcitation takes place, in which mobile  
107    charge carriers are driven by the light-induced electric field.<sup>26, 27</sup> The energy gained by the carriers  
108    is subsequently converted into heat. One key feature of photothermal materials is their broadband  
109    light absorption because the solar spectrum ranges from 280 nm to 2500 nm at sea level.<sup>28-30</sup>  
110    Hence, an ideal photothermal material would absorb solar light over the entire spectrum, ensuring  
111    a high thermal energy output.

112            A variety of photothermal materials exhibit high light absorption, including plasmonic  
113    nanomaterials, semiconductors, polymers, and nanocarbon materials. These solar absorbers  
114    mainly rely on three kinds of photoexcitation: plasmonic local heating of noble metal nanoparticles,  
115    non-radiative relaxation of electron-holes of semiconductors, and thermal vibration of organic  
116    molecules of polymers and nanocarbon materials. Here, we discuss the different types of  
117    photothermal materials and highlight their photothermal efficiency, long-term stability,  
118    environmental impact, scalability, and economic aspects.

### 119            **2.1.1. Plasmonic nanostructures**

120    The photothermal effect of noble metal nanoparticles is ascribed to the excitation of localized  
121    surface plasmons under light irradiation (Figure 3A).<sup>31</sup> When the frequency of incident light  
122    matches the localized surface plasmon resonance (LSPR) frequency of the metal nanoparticles,  
123    electrons exhibit collective coherent oscillation.<sup>32, 33</sup> LSPR decays either radiatively, resulting in  
124    light scattering, or non-radiatively, by generating hot electrons with very high kinetic energy that  
125    are eventually converted to heat. Various types of plasmonic nanoparticles have been utilized for  
126    solar evaporators, such as Au,<sup>34, 35</sup> Ag,<sup>36</sup> CuS,<sup>37</sup> Cu,<sup>38, 39</sup> Al,<sup>40</sup> and Pd<sup>41</sup> nanoparticles.

127 Au nanostructures have been widely explored for lots of applications, owing to their  
128 chemical stability, ease of synthesis, and facile tunability of size, shape, and optical properties.  
129 Halas and co-workers performed a detailed investigation how vapor forms on the surface of Au  
130 nanosphere under light illumination,<sup>42</sup> and demonstrated solar evaporation with Au nanosphere-  
131 enabled volumetric heating.<sup>17</sup> Although the steam generation efficiency was only 24%, their  
132 finding opened up possibilities for Au nanostructure-based solar evaporators. To obtain high  
133 evaporation efficiency, one design with a self-floating film composed of Au nanoparticles at the  
134 air-water interface was employed for localized heating (Figure 3C).<sup>43</sup> Under 532 nm laser  
135 illumination at a power density of  $10.18 \text{ W}\cdot\text{cm}^{-2}$ , the evaporation efficiency for this interfacial  
136 heating evaporator (44%) was significantly higher than that achieved by volumetric heating.  
137 Advancing beyond the two-dimensional (2D) architecture, a three-dimensional (3D) plasmonic  
138 biofoam, realized by immobilizing Au nanorods on bacterial nanocellulose (BNC), enhanced the  
139 evaporation efficiency to 76.3% upon irradiation by a 808 nm laser at a power density of  $5.1 \text{ W}\cdot\text{cm}^{-2}$   
140 (Figure 3D).<sup>10</sup>

141 The main obstacle preventing Au nanoparticles from achieving broadband absorption is  
142 the inherent narrow extinction bandwidth of their LSPR. The typical full width at half maximum for  
143 Au nanorods ranges from 100 nm to 200 nm; for Au nanospheres, it ranges from 60 nm to 110  
144 nm.<sup>10, 44, 45</sup> The LSPR wavelength of plasmonic nanostructures is determined by the composition,  
145 size, shape, and coupling distance of plasmonic nanostructures (Figure 3B).<sup>44, 46, 47</sup> Self-  
146 aggregated Au nanowire bundle array structures with a wide range of nanoscale gaps exhibited  
147 ultrabroadband light absorption of 91% at 400-2500 nm, and their solar evaporation efficiency  
148 was up to 57% at a light intensity of  $20 \text{ kW}\cdot\text{m}^{-2}$ .<sup>48</sup> An alternative strategy to expand absorbance  
149 is to employ Au nanoparticles with a wide distribution of sizes and shapes. Such Au nanoparticles  
150 were deposited on an  $\text{Al}_2\text{O}_3$  nanoporous substrate (Figure 3E).<sup>49</sup> In this study, light absorbance  
151 was calculated to be ~99% across the wavelength ranging from 400 nm to 10  $\mu\text{m}$ , and 90%

152 evaporation efficiency was noted under solar irradiation at a power density of 4 kW·m<sup>-2</sup>.  
153 Fratolocchi and co-workers fabricated Au nanostructures by connecting a nanorod to a  
154 nanosphere on a filter paper, and the coupled plasmon resonance of these nanostructures  
155 resulted in a broadband absorption.<sup>50</sup> Consequently, the solar evaporation efficiency reached 87%  
156 at a light intensity of 2.3 kW·m<sup>-2</sup>.

157 Other advantages of plasmonic nanostructures are their long-term stability and  
158 recyclability. Au nanoparticle-based solar evaporator have exhibited superior recyclability of 98%  
159 in saline environments, and wood integrated with plasmonic Pd nanoparticles displayed  
160 remarkable stability after cycling for 144 hours in solar steam generation.<sup>41, 50</sup> Excellent  
161 recyclability also alleviates the burden on the environment. Moreover, most plasmonic  
162 nanostructures are synthesized by wet chemistry, so they can be produced on a large scale,  
163 suggesting that interfacial evaporators can also be produced on a large scale. However, the noble  
164 metals are expensive, which limits their real-world applications.

### 165 **2.1.2. Semiconductors**

166 The bandgap energy of semiconductors determines their light-to-heat conversion.<sup>51</sup> When the  
167 energy of incident light is higher than that of the semiconductor bandgap, the light is absorbed  
168 and electron-hole pairs are generated (Figure 3F). For a semiconductor with a narrow bandgap,  
169 the above-bandgap electron-hole pairs relax to the band edges, and the extra energy is non-  
170 radiatively released in the form of phonons that are converted to heat. However, for a broad  
171 bandgap, the electron-hole pairs recombine near the bandgap edges, releasing photons and  
172 lowering the photothermal efficiency. Semiconductors with narrow bandgaps have been  
173 extensively explored for solar steam generation. Examples include black titania<sup>52-54</sup>, MoS<sub>2</sub><sup>55-58</sup>,  
174 Ti<sub>3</sub>O<sub>4</sub> nanoparticles<sup>54</sup>, oxygen-deficient MoO<sub>3</sub> quantum dots<sup>59</sup>, and Fe<sub>3</sub>O<sub>4</sub><sup>60</sup>. An appealing  
175 approach to improve optical properties is reducing the size of bulk materials to nanoscale, which  
176 favors the light scattering among nanoparticles. Over the whole solar spectrum, bulk Ti<sub>2</sub>O<sub>3</sub>

177 displayed 85.5% light absorption, whereas 400 nm nanoparticles displayed a total absorption of  
178 92.5% (Figure 3G).<sup>61</sup> Chemically exfoliated MoS<sub>2</sub> nanosheets absorbed 96% of incident light after  
179 incorporation into a BNC aerogel, whereas bulk MoS<sub>2</sub> absorbed 90% of the light (Figure 3H).<sup>56</sup>  
180 For semiconductors with wide bandgaps, narrowing the bandgap through doping is a common  
181 way to improve the light absorption.<sup>62, 63</sup> TiO<sub>2</sub> can absorb UV light only at wavelengths lower than  
182 400 nm, corresponding to the intrinsic large bandgap (~3 eV). In contrast, black titania, partially  
183 reduced titanium oxide from Ti<sup>4+</sup> into Ti<sup>3+</sup> by introducing oxygen vacancies, endowed narrow  
184 bandgap and realized 96% light absorption.<sup>54</sup> These semiconductors are non-toxic and stable in  
185 aqueous environments. However, for most semiconductors with wide bandgaps, doping requires  
186 treatment at high temperatures ranging from 200 °C ~ 600 °C, which increases the synthesis cost.

### 187 **2.1.3. Nanocarbon materials**

188 The photothermal effect of nanocarbon materials stems from their lattice vibrations upon light  
189 illumination (Figure 3I). The loosely-held electrons in the  $\pi$  orbital of carbon materials are excited  
190 by a small energy input and jump to the  $\pi^*$  orbital.<sup>64</sup> Heat is generated when the excited electrons  
191 relax to the ground state. Diverse nanocarbon materials have been explored, such as graphite<sup>65</sup>,  
192 carbon nanotubes (CNT)<sup>66-68</sup>, graphene oxide (GO) /reduced graphene oxide (rGO)<sup>69-73</sup>, and  
193 carbon black<sup>74</sup>.

194 Nanocarbon materials can absorb sunlight over a broad spectrum, and the universal  
195 strategy for improving optical absorption is to tailor their structures. GO/rGO is a widely studied  
196 carbonaceous material for solar evaporation, owing to its good hydrophilic surface and the large  
197 surface area of the 2D flake structure.<sup>75</sup> It is generally assembled into a porous structure to  
198 augment light capture (Figure 3K). For example, a compact rGO film fabricated by vacuum  
199 filtration exhibited 13% diffuse reflection,<sup>76</sup> whereas the reflectance for rGO foam was only  
200 2.5%.<sup>22</sup> Various 2D and 3D configurations have been developed for solar evaporation. A  
201 membrane composed of vertically aligned rGO nanosheets was realized using antifreeze-

202 assisted freezing technique, and the run-through channels were favorable for light absorption  
203 during solar evaporation.<sup>77</sup> In other work, a concentrated GO-based solution with sufficiently high  
204 shear elastic modulus and shear yield strength acted as an ideal 3D printing ink, and a  
205 sophisticated GO aerogel built by 3D printing possessed high porosity, up to 97.3%.<sup>78</sup> This well-  
206 designed porous structure allowed broadband solar absorption higher than 97%. Another  
207 advantage of a GO/rGO-based evaporator is the feasibility of its large-scale fabrication. A large  
208 area of rGO hydrogel can be fabricated by a surfactant-foaming sol-gel method, which effectively  
209 disrupts and reconstructs the GO liquid crystals in dispersions via microbubble templates.<sup>79</sup> After  
210 simple freezing and air drying, a bulk aerogel with a structure-intact size of about 1 m<sup>2</sup> was  
211 fabricated (Figure 3J1). The large scale open-porous structure exhibited high solar-thermal  
212 conversion and decent mechanical properties (Figure 3J2), which make it an attractive candidate  
213 for large-scale solar evaporation.

214 Compared with plasmonic nanoparticles and semiconductors, nanocarbon materials  
215 exhibit broadband absorption and the cost of their synthesis is much lower. Combining the merits  
216 of abundance, chemical stability, non-toxicity, facile synthesis, and scalability, they have emerged  
217 as one of the most widely investigated photothermal materials for solar evaporation.

#### 218 **2.1.4. Polymers**

219 The light-to-heat conversion of polymers is also attributed to the energy released when the excited  
220 electrons in the lowest unoccupied molecular orbital (LUMO) relax to the highest occupied  
221 molecular orbital (HOMO). Polypyrrole (PPy)<sup>80-85</sup> and polydopamine (PDA)<sup>86-90</sup> are the most well  
222 studied photothermal polymers for solar evaporation, due to their broadband absorption, low cost,  
223 ease of synthesis, and remarkable biocompatibility. A distinctive characteristic of polymers is their  
224 flexibility, which enables their deposition on various substrates with curved structure that aids in  
225 solar energy harvesting. PPy can be facilely coated by chemical vapor deposition polymerization  
226 on air-laid paper,<sup>80</sup> by in situ solution-phase polymerization on cotton fabric and polypropylene

227 mesh,<sup>81, 82</sup> and by electro-polymerization on stainless steel mesh (Figure 3L).<sup>83</sup> The PPy coating  
228 was stable and offered over 90% broad-spectrum absorption of solar light. Inspired by the  
229 adhesive protein in mussels, PDA with a structure similar to eumelanin is well-known for its  
230 versatile adhesion on almost all substrates via self-polymerization of dopamine in alkaline  
231 solution.<sup>91</sup> A homogeneous PDA coating formed on a wood surface and carbonized the cotton  
232 fabric could absorb almost all the light in the UV-visible region and the majority of the light in the  
233 NIR region.<sup>86, 88</sup> The hydrophilic nature of PDA ensures adequate water to contact the hot surface  
234 zone for evaporation, and the rough surface of the PDA layer further contributes to the light  
235 harvesting. As an alternative to depositing a PDA layer on various substrates, PDA microspheres  
236 were synthesized for solar evaporation, and the size was optimized to improve the light  
237 absorption.<sup>90</sup> After integration with BNC aerogel, the resulting PDA/BNC bilayer structure  
238 exhibited up to 98% light absorption over the range from 450 nm to 750 nm (Figure 3M).  
239 Compared to most other photothermal materials discussed above, the biocompatibility, low  
240 toxicity and biodegradable nature of PDA make it an environmentally-benign material, and its  
241 versatile adhesion enables it to be potentially deployed on large scales in aqueous environments  
242 with minimal effect on the ecosystem.<sup>90, 92</sup> However, this presumption is yet to be comprehensively  
243 investigated.

244         The performance of different solar absorbers, their efficiency, long-term stability, toxicity,  
245 and cost are listed in Table 1. Their performance is closely related to the intrinsic material  
246 properties and optimization of their structures. Although some photothermal materials cannot be  
247 directly compared, the list here provides an overview of the advantages and disadvantages of  
248 these materials to guide researchers in choosing photothermal materials for solar absorber layers  
249 for enhanced solar energy harvesting. For real-world applications, it is also important to note that  
250 performance and cost need to be balanced for economic viability.

251 **Table 1. Solar evaporation efficiency of photothermal materials under different light intensities, long term stability,**  
 252 **environmental impacts, scalability, and material costs.**

Materials		Membrane processes	Solar-evaporation efficiency	Light intensity	Stability	Environmental impacts	Scalability	Photothermal material cost*
Plasmonic metals	Self-assembled Au-NPs- Anodized aluminum oxide (AAO) <sup>49</sup>	Solar steam generation	90%	4 kW·m <sup>-2</sup>	-	-	-	384\$/g
	Au nanowire with AAO widening <sup>48</sup>		57%	20 kW·m <sup>-2</sup>	-	-	-	384\$/g
	AuNR/BNC aerogel <sup>10</sup>		76.3%	51 kW·m <sup>-2</sup>	Mechanically stable	No toxicity	Scalable	384\$/g
	Self-assembly AuNPs film <sup>43</sup>		87%	2.3 kW·m <sup>-2</sup>	Stable after using for 3 weeks	No toxicity	Scalable	384\$/g
	AuNR/AuNS/Paper <sup>50</sup>		87%	2.3 kW·m <sup>-2</sup>	Stable after using for 3 weeks	No toxicity	Scalable	384\$/g
	Pd NPs/wood <sup>41</sup>		85%	10 kW·m <sup>-2</sup>	Stable performance after 144 h	No toxicity	Scalable	1394\$/g

	Ag-NPs-PVDF <sup>36</sup>	Photothermal vacuum membrane distillation	29.6%	$23.2 \times 10^3 \text{ Jm}^{-2}\cdot\text{s}^{-1}$	Stable performance after 7 days (10 h/day)	-	-	12.34\$/g
Semiconductors	Narrow-bandgap $\text{Ti}_2\text{O}_3$ NPs <sup>61</sup>	Solar steam generation	-	$1 \text{ kW}\cdot\text{m}^{-2}$	Stable performance after 25 cycles (1h/cycle)	-	-	5.47\$/g
	$\text{MoS}_2$ /BNC bilayer aerogel <sup>56</sup>		81%	$5.35 \text{ kW}\cdot\text{m}^{-2}$	Stable performance over 20 cycles (15 min/cycle)	Lower cytotoxicity than graphene derivatives and carbon nanotubes	Scalable	-
	Black $\text{TiO}_x$ coated stainless steel mesh <sup>93</sup>		50%	$1 \text{ kW}\cdot\text{m}^{-2}$	Chemically stable	Low toxicity	-	5.47\$/g
	Black titania film <sup>54</sup>		70.9%	$1 \text{ kW}\cdot\text{m}^{-2}$	Stable performance over 10 cycles (5h/cycle)	Low toxicity	-	5.47\$/g

Nanocarbon materials	3D-printing GO/CNT/CNF evaporator <sup>78</sup>	Solar steam generation	85.6%	1 kW·m <sup>-2</sup>	Mechanically stable	No toxicity	-	452\$/g
	Graphene foil supported porous graphene sponge <sup>94</sup>		89.6%	1kW·m <sup>-2</sup>	-	-	Scalable	602\$/g
	Hierarchical graphene foam <sup>71</sup>		91.4%	1 kW·m <sup>-2</sup>	Stable performance over 20 cycles (1.5 h/cycle)	-	Scalable	-
	3D graphene material <sup>95</sup>		87%	1 kW·m <sup>-2</sup>	Stable performance over 20 cycles (2 h/cycle)	-	Scalable	122\$/g
	GO-Based Aerogel <sup>72</sup>		83%	1 kW·m <sup>-2</sup>	-	-	-	122\$/g
	GO film on cellulose-wrapped polystyrene foam <sup>96</sup>		80%	1 kW·m <sup>-2</sup>	Stable performance over 10 cycles (1h/cycle)	-	Scalable	122\$/g
	Wood-GO composite <sup>97</sup>		83%	12 kW·m <sup>-2</sup>	Stable performance over 6 cycles (1000s/cycle)	-	Scalable	122\$/g

	RGO/BNC <sup>22</sup>		83%	10 kW·m <sup>-2</sup>	Stable performance over 8 cycles (900s/cycle)	-	-	580\$/g
	Vertically aligned graphene sheets <sup>77</sup>		94.2%	4 kW·m <sup>-2</sup>	-	-	Scalable	580\$/g
	RGO with PVA network hydrogel <sup>69</sup>		95%	1 kW·m <sup>-2</sup>	Stable performance over 96 h	-	Scalable	580\$/g
	RGO with polystyrene membrane <sup>98</sup>		83%	1 kW·m <sup>-2</sup>	Stable performance over 4 cycles (4.5 h/cycle)	-	-	580\$/g
	CNT nanofluid <sup>99</sup>		45%	10 kW·m <sup>-2</sup>	Stable adsorption intensity over 14 days	-	-	673\$/g
	CNT/silica porous structure <sup>100</sup>		82%	1 kW·m <sup>-2</sup>	-	-	-	673\$/g
	Vertically aligned CNT arrays <sup>101</sup>		90%	15 kW·m <sup>-2</sup>	-	-	-	673\$/g
	Exfoliated graphite/carbon foam <sup>21</sup>		85%	10 kW·m <sup>-2</sup>	-	-	-	1.9\$/g

	Carbon black coated cellulose/polystyrene foam <sup>102</sup>		100%	1 kW·m <sup>-2</sup>	-	-	Scalable	48.4\$/g
	Flame-treated wood <sup>103</sup>		72%	1 kW·m <sup>-2</sup>	Stable performance after 1 h ultrasonic treatment	-	Scalable	-
	Carbonized mushrooms <sup>104</sup>		78%	1 kW·m <sup>-2</sup>	Stable performance over 8 cycles (6h/cycle)	-	-	-
	Carbonized daikon <sup>105</sup>		85.9%	1 kW·m <sup>-2</sup>	Stable performance over 10 cycles	-	Scalable	-
	Carbonized lotus seedpods <sup>106</sup>		86.5%	1 kW·m <sup>-2</sup>	Stable performance over 10 cycles (6h/cycle)	-	-	-
	Carbon black NPs <sup>107</sup>		Photothermal DCMD	74.6%	1.3 kW·m <sup>-2</sup>	Stable performance over 1 h	-	-
Polymers	PPy-coated air-laid paper <sup>80</sup>	Solar steam generation	82.3%	1 kW·m <sup>-2</sup>	Stable performance over 30 cycles	No toxicity	Scalable	-
	PPy-coated stainless-steel mesh <sup>83</sup>		58%	1 kW·m <sup>-2</sup>	Stable performance over 100 h	-	-	-

	PDA-filled BNC <sup>90</sup>		78%	1 kW·m <sup>-2</sup>	Stable performance over 20 cycles (15 min/cycle)	Low toxic, biocompatible, and biodegradable PDA and BNC	Scalable	6.8\$/g
	PDA-coated wood <sup>86</sup>		87%	1 kW·m <sup>-2</sup>	Durable performance over 10 cycles (1h/cycle)	Biocompatible and biodegradable	Scalable	6.8\$/g
	FTCS-PDA-PVDF membrane <sup>108</sup>	Photothermal DCMD	45%	0.75 kW·m <sup>-2</sup>	Stable performance over 10 cycles (1 h/cycle)	Low toxic, biocompatible, and biodegradable PDA	Scalable	6.8\$/g

253 \*Costs for raw photothermal materials were based on information from Sigma-Aldrich and are not the cost for building an entire solar  
 254 evaporator. This information is intended only to provide a guideline and relative comparison rather than the absolute market price.

## 255            **2.2.    Substrate materials**

256    After the validation of integrating supporting substrates for enhanced solar evaporation, bilayer  
257    solar evaporators have been widely explored for solar steam generation. Generally, the bottom  
258    layer provides a mechanically stable support, thermal management, and water transportation to  
259    the top solar absorber layer. Thermal management is essential for high efficiency of solar steam  
260    generation. When the temperature of the solar absorber layer rises upon light irradiation, the heat  
261    loss by thermal radiation, convection and conduction to a surrounding medium occurs, which  
262    significantly lowers the evaporation efficiency. To avoid the large thermal loss in a conventional  
263    bulk heating apparatus (Figure 4A), a floating solar absorber layer has been constructed for  
264    interfacial evaporation (Figure 4B). For example, thin film by self-assembly gold nanoparticles,  
265    carbon nanoparticles incorporated with iron oxide or magnetic microspheres floated on the  
266    interface of water and air, yielding evaporation rate much higher than that of bulk heating by  
267    dispersing photothermal agents in the whole reservoir.<sup>43, 60, 109</sup> Although the interfacial heating  
268    solar evaporation utilizes thermal energy more efficiently, heat conduction from the hot zone to  
269    the underlying bulk water lowers the steam generation performance. To further mitigate the heat  
270    loss from the photothermal layer to the underlying bulk water, substrates acting as heat barriers  
271    can be utilized, which confine the thermal energy to the evaporative surface and improve the  
272    steam generation efficiency (Figure 4C). Chen and co-workers developed a double-layer solar  
273    steam generator consisting of graphite layers as solar absorbers and carbon foam as a thermally  
274    insulating substrate (Figure 4E-G).<sup>21</sup> The carbon foam had low thermal conductivity, which  
275    suppressed thermal dissipation from the hot surface region. The carbon foam also reduced the  
276    contact area between the water and the hot zone, which further confined the heat to the  
277    evaporative surface. After incorporation of the thermal insulator, the efficiency of the solar  
278    evaporators increased from 65% to 85% under 10 sun irradiation (power density of 10 kW·m<sup>-2</sup>)

279 (Figure 4J). This pioneering work has attracted wide attention to the design of substrates with  
280 good thermal insulation to improve solar steam generation.

281 Besides the thermal management, another important consideration for substrates is  
282 supplying sufficient water to the solar absorber layers for evaporation. Water transportation relies  
283 on capillary force, so the substrate is usually constructed into an interconnected porous structure  
284 to provide sufficient channels for water pumping. The capillary force is determined by the wet  
285 properties of the pores and the pore size. To further facilitate water transportation, the water flow  
286 channel is usually designed with hydrophilic materials. Ideal substrates can wick enough water to  
287 the photothermal layer to convert heat to vapor and provide excellent thermal insulation  
288 simultaneously. Below, we summarize recent progress in substrates materials with superior  
289 thermal insulation and water transportation abilities.

290 Synthetic polymers such as polystyrene (PS)<sup>96, 110</sup>, polyurethane (PU)<sup>111-113</sup>, and  
291 polyvinylidene fluoride (PVDF)<sup>114, 115</sup> are excellent choices for supporting layers because their low  
292 thermal conductivity, commercial availability and low density makes them float on the water  
293 surface (Figure 5B). With simple physical or chemical approaches, photothermal materials can  
294 be readily deposited on synthetic polymer layers to generate a bilayered solar evaporator (Figure  
295 5A). Despite their facile design and preparation, synthetic polymers barely satisfy the increasing  
296 structural and material requirements for supporting layers in nano- or micro-scale.

297 Inorganic materials with hierarchical porous structures, low thermal conductivity, high  
298 aqueous stability, and low light absorption have been exploited as supporting substrates for solar  
299 evaporators (Figure 6). Nanoporous anodic aluminum oxide (AAO) is an attractive candidate as  
300 a supporting material for loading photothermal materials due to its low thermal conductivity and  
301 columnar pores that can maximize the interaction between light and photothermal materials.<sup>40, 48,</sup>  
302 <sup>49, 116, 117</sup> The hierarchical pores serve as channels for water transportation as well as templates  
303 for loading solar absorbers in the upper regions. For example, Au nanoparticles (Figure 6A) and

304 Al nanoparticles were deposited on a nanoporous template (NPT), and this porous plasmonic  
305 membrane enabled over 96% light absorption and over 90% steam generation efficiency under  
306 concentrated light.<sup>40, 49</sup> The merit of the AAO membrane is its fine control over the sizes and  
307 periodicity of the pores, achieved by various techniques. Padilla and co-workers employed a pore-  
308 widening technique to make a vertically aligned nanowire array by wet etching the ordered  
309 hexagonal nanopores of an AAO membrane. Subsequent drying resulted in self-aggregated  
310 nanowire bundles, which possessed varying nanoscale gaps as well as microscale funnel  
311 structures (Figure 6B).<sup>48</sup> After black Au film was deposited on the bundles, the plasmonic  
312 membrane with a multiscale porous structure achieved an evaporation efficiency of 57% under a  
313 light intensity of 20 kW·m<sup>-2</sup>. Other substrate materials have also been explored. Hydrophilic  
314 microporous silica substrates with low thermal conductivity have been demonstrated to offer water  
315 pumping, thermal insulation, and mechanical support for a thin layer of CNT serving as a  
316 photothermal layer, and this bilayered evaporator achieved a solar thermal efficiency of 82%  
317 (Figure 6C).<sup>100</sup> Considering the high temperature caused by photothermal materials under light  
318 exposure, a thermally stable substrate formed using ultralong hydroxyapatite (HA) nanowires  
319 (Figure 6F) was employed to support CNT for solar steam generation (Figure 6E).<sup>118</sup> The intrinsic  
320 low thermal conductivity reduced heat loss from the solar absorbers to the bulk water, and the  
321 interconnected porous network from the hydroxyapatite nanowire (HN) paper allowed sufficient  
322 water transportation (Figure 6D). This fire-resistant HN/CNT photothermal paper achieved an  
323 efficiency of 83.2% under 1 sun irradiation.

324         The usage and disposal of supporting layers made of hazardous or non-biodegradable  
325 materials can cause significant negative impact on aqueous environmental systems. Thus,  
326 cellulose-based supporting materials, which are renewable, biodegradable, and scalable, hold a  
327 great promise for future solar evaporation systems (Figure 7). Commercially available air-laid  
328 paper with low thermal conductivity, excellent hydrophilicity, and microscale pores is a convenient

329 material for a supporting substrate.<sup>34, 119-121</sup> Its high surface roughness enables easy modification  
330 with photothermal materials, such as rGO, Au nanoparticles, and Ag nanoparticles, to assemble  
331 simple solar evaporators (Figure 7A). However, mechanical strength and aqueous stability limit  
332 air-laid papers to achieve robust and scalable solar evaporators.

333 Cellulose foam, formed via bottom-up bio-fabrication (BNC foam, realized by bacteria-  
334 mediated growth) or templated fabrication, has been demonstrated to be a highly promising  
335 substrate for solar evaporation.<sup>10, 22, 56, 67, 90</sup> Singamaneni and co-workers have developed and  
336 demonstrated a novel, scalable approach for realizing BNC bilayered foams, with the top layer  
337 incorporating various photothermal materials (rGO, MoS<sub>2</sub>, Au nanoparticles, and even  
338 biodegradable PDA particles) and the bottom layer made of pristine BNC (Figure 7B). As a  
339 supporting layer, cellulose foam presents low thermal conductivity, nano- or micro-scale porosity,  
340 excellent hydrophilicity, and aqueous stability, ensuring the high performance in solar evaporators.

341 Inspired by the transpiration of trees, which relies on a distinctive porous structure to  
342 transport mass and heat, natural wood has been used to construct wood-based interfacial  
343 evaporators (Figure 7C).<sup>41, 66, 97, 103, 122</sup> Significantly, natural wood, composed mostly of cellulose,  
344 has i) a hydrophilic columnar microchannel network (Figure 7E), allowing fast water transport;  
345 and ii) excellent thermal insulation properties, ensuring heat localization. Moreover, wood-based  
346 solar evaporators can be readily realized by integrating photothermal materials, such as GO, Au  
347 nanostructures, and CNT. Alternatively, simple carbonization of the wood surface produces  
348 photothermal properties (Figure 7D). All these traits suggest that wood is a very attractive  
349 candidate as a supporting substrate for solar evaporators.<sup>123</sup>

350 Generally, intricate design and development of supporting layers with desired properties  
351 such as thermal management, water transportation, and porous structures have fostered the  
352 development of high-performance solar evaporation devices. To enable broad application of the  
353 interfacial solar evaporation technology, the utilization of renewable, environmentally friendly,

354 scalable materials is an important consideration for the design of the future solar evaporation  
355 systems.

### 356 **3. Structural optimization**

357 Advances in the design and synthesis of nanomaterials have played a critical role in the  
358 development of solar steam generators. Simultaneously, nano- or micro-fabrication has enabled  
359 rational structural designs for solar absorbers and substrates, which further boost light capture  
360 and mitigate thermal loss to the environment. Below, we discuss the evolution in the structure of  
361 the solar absorbers and supporting substrates towards high-performance solar evaporator.

#### 362 **3.1. Structural optimization of solar absorbers for efficient energy harvesting**

363 Optimal structure at the nano- and micro-scales is important to improve light and heat trapping.  
364 In most current solar evaporators, the photothermal layers are designed to be sufficiently thick to  
365 ensure negligible light transmission. At the same time, minimizing reflection is also critical to  
366 achieving high optical absorption. The refractive index of most photothermal materials is higher  
367 than 2, so their light reflection is greater than 11% according to the Fresnel equation.<sup>124</sup> To reduce  
368 light reflection, the solar absorber is generally processed into a nano- or micro-porous structure.<sup>125</sup>  
369 As light travels through this porous structure, it undergoes multiple reflections inside the walls of  
370 the pores, which maximizes light absorption by the material and consequent heat generation  
371 (Figure 8). In addition, light absorption by a flat surface exhibits strong dependence on the angle  
372 of the incident light.<sup>126</sup> Photothermal layers with nano- and micro-porous structures exhibit  
373 significantly smaller angular dependences of optical absorption and can absorb light over a wide  
374 range of incident angles.

375 After absorbing the incident light, photothermal materials convert the light to thermal  
376 energy. Ideally, the solar absorber should utilize all the heat to evaporate the seawater or  
377 wastewater. However, heat loss by conduction and radiation occurs, arising from the much higher

378 temperature of the photothermal layer compared to the surroundings (bulk water and external  
379 environment). To suppress the thermal loss, 3D macroscopic solar absorbers (e.g., 3D origami,  
380 cup and cylinder) offer a compelling strategy of enhancing energy harvesting to fast steam  
381 generation.<sup>102, 126, 127</sup> The elaborately designed geometry creates a temperature gradient along  
382 the evaporative surface, so heat flows from hotter regions to cooler regions and thus recovers  
383 heat loss. Radiated heat from the lower region can be reabsorbed by the upper region, which  
384 further mitigates thermal dissipation. Moreover, the temperature of partially evaporative surface  
385 can be even lower than the atmosphere, which allows energy acquisition from the environment.  
386 By reducing heat loss and harvesting environmental energy, 3D macroscopic solar absorbers  
387 achieve much higher evaporation efficiency than conventional planar solar absorbers.

### 388 **3.1.1. Enhanced solar absorption**

389 During light interactions with solar absorbers, reflection causes the major light loss. Constructing  
390 a 3D microporous structure is a typical route to improve light capture. The internal pores favor  
391 light reflection within the materials and thus increase light absorption. For this reason, solar  
392 absorbers are generally processed into 3D microporous structures. For example, a compact rGO  
393 film with a smooth surface exhibited high reflectance, with light absorption of only around 40%  
394 (Figure 9A). In contrast, an rGO membrane with an open porous structure exhibited over 93%  
395 light absorption (Figure 9B).<sup>77</sup>

396 A common approach to assemble 3D microporous solar absorbers is a template-assisted  
397 method. For example, Al nanoparticles deposited on a 3D porous aluminum oxide membrane  
398 absorbed over 96% of a broad solar spectrum (Figure 9C-G).<sup>40</sup> Similarly, CNT coated on porous  
399 cellulose nanofibrils aerogel achieved an absorbance of 97.5%.<sup>67</sup> Graphene foam fabricated by  
400 chemical vapor deposition on a 3D porous nickel skeleton also exhibited 90% light absorption.<sup>71</sup>

401 In addition to these rigid substrates, solvents can also serve as soft templates for  
402 fabricating 3D microporous solar absorbers. After dispersing the solar absorbers in the solvent,

403 the mixtures are frozen, and the resultant solvent crystals act as templates to organize the solar  
404 absorbers. Inorganic or organic binding agents are also added if the intrinsic interaction among  
405 solar absorbers is not strong. After evaporating the solvent, the 3D porous structures are formed.  
406 For example, rGO-based aerogel was fabricated by freeze-drying GO solution with the aid of  
407 polyvinyl alcohol (PVA) (Figure 9H-I). It exhibited high light absorption over the entire solar  
408 spectrum, with a negligible optical loss.<sup>69</sup> These 3D microstructures enhance the light harvesting,  
409 overcoming the intrinsic reflectance of solar absorbers. Future research should focus on  
410 constructing these 3D porous solar absorbers on a large scale, at a cost low enough for real-  
411 world applications.

### 412 **3.1.2. Enhanced thermal energy harvesting**

413 Current methods to increase the thermal energy output from solar absorbers mainly rely on  
414 improving light absorption. However, for conventional planar solar absorbers, the resultant high  
415 temperature of the evaporating layer inevitably causes thermal energy loss to the surrounding  
416 environment, which lowers the evaporation efficiency. Recently, 3D macroscopic solar absorbers  
417 have been proposed to mitigate radiative and convective heat loss. Further, well-designed  
418 architectures for solar absorbers could even gain energy from the surroundings, allowing an  
419 evaporation efficiency close to or even nominally higher than 100%.

420 For example, using Miura-ori tessellation, Wang and co-workers reported an innovative  
421 solar evaporator with an origami structure composed of folded and unfolded periodic pleats  
422 (Figure 10A-B).<sup>121</sup> The 3D concave structure not only improves light absorption by offering  
423 multiple reflections on the evaporative surface, but also mitigates thermal loss. Under illumination,  
424 the temperature of valley folds was higher than that of mountain folds (Figure 10D), and this  
425 temperature gradient resulted in a directional thermal flow from the hotter valley folds to the cooler  
426 mountain folds, that enabled the partial recovery of dissipated heat loss. Moreover, the radiative  
427 heat from the valley folds could be reabsorbed by the mountain parts. Therefore, the efficiency of

428 the 3D origami structure reached approximately 100% when the ratio of the  $A_{\text{active}}$  (light interactive  
429 area) /  $A_{\text{project}}$  (light projected area) was around 4.65 (Figure 10C). The planar counterpart showed  
430 an efficiency of only 71%, associated with convection and radiation losses of 10.9% and 13.5%,  
431 respectively. The same group also designed a 3D cylindrical cup-shaped solar evaporator, using  
432 mixed metal oxides as photothermal materials.<sup>127</sup> The high energy efficiency, reaching nearly 100%  
433 under 1 sun irradiation, was closely related to the 3D cup structure, as the wall of cup effectively  
434 reabsorbed the reflected light and thermal radiation from the bottom of cup and also gained extra  
435 energy from the environment, because the lip of the wall was cooler than the environment.

436 An elaborate 3D macroscopic structure not only suppresses thermal energy loss to the  
437 surroundings, but also favors directly obtaining energy from the environment. Zhu and co-workers  
438 designed a cylindrical vapor generator with a height of 10 cm and a diameter of 5.7 cm (Figure  
439 10E).<sup>102</sup> With light illumination, the higher temperature was noted on the top surface compared  
440 with environment, whereas the side surface was cooler than the atmosphere because of less  
441 absorption of solar energy (Figure 10F) and evaporative cooling effect. Thus, the side surface of  
442 the solar absorber harvested energy from the environment by convective and radiative heat  
443 transfer process (Figure 10G-K). Combining the solar energy input and extra energy gained from  
444 environment, the efficiency of this smart structure was beyond the theoretical limit value of a 100%  
445 solar-to-vapor energy transfer efficiency.

446 These unique 3D macroscopic solar absorbers, by reducing thermal dissipation and  
447 harvesting energy from their surroundings, surpass the energy efficiency of conventional 2D  
448 configurations and provide design guidelines for high-performance solar evaporators. Besides  
449 their outstanding efficiency, these macroscopic configurations were assembled with inexpensive  
450 materials using cost-effective processing methods. However, large-scale fabrication of these 3D  
451 macroscopic structures and their mechanical stability in harsh real-world environmental  
452 conditions such as wind and rain are challenges.

453           **3.2. Advanced substrate design for efficient thermal management and water**  
454           **transportation**

455 As noted above, thermal insulation and water transportation are two fundamental requirements  
456 for substrates. Substrates should supply plenty of water to the hot zone for steam generation.  
457 However, too much water to the evaporative layer leads to thermal loss via heat conduction and  
458 thus lowers the heat confinement. To further improve the solar evaporation efficiency beyond  
459 those offered by the traditional designs discussed above, outstanding substrates need to achieve  
460 a balance between thermal insulation and water transportation.

461           In addition, salt accumulation on the evaporative surface should be taken into account as  
462 it decreases water transportation and optical properties.<sup>128, 129</sup> 3~3.5% dissolved salts, such as  
463 NaCl and CaCl<sub>2</sub>, exist in seawater.<sup>130</sup> Solute concentrations increase significantly at the heating  
464 zone after water evaporation, and subsequently precipitated salt aggregates at the evaporative  
465 surface when solute concentrations saturate. The accumulated salt hampers the solar absorption  
466 because of light reflection by the salt layer, and also reduces the water supply to the evaporative  
467 surface by blocking water pathways; both of which lower the evaporation efficiency. Periodic  
468 physical cleaning increases the operational cost for the solar evaporators and poses difficulty for  
469 a large-scale operation. Developing salt-resistant structures is imperative to achieve long-term  
470 steady desalination.

471           **3.2.1. 1D/2D water pathway configurations**

472 To resolve the trade-off between heat management and water transportation, reduced  
473 dimensionality of water pathways mitigate the thermal conduction loss while maintaining sufficient  
474 capillary force to facilitate water transportation. Instead of a 3D random and interconnected  
475 microporous configuration, substrates with 1D or 2D water pathways simultaneously allow  
476 excellent thermal insulation and water transportation.<sup>96, 104, 110, 126, 130, 131</sup> Unlike conventional  
477 substrate design where the thermal insulation layer and water pathways are constructed together,

478 the thermal insulator and water supplier are two independent components in 1D/2D water  
479 pathway configurations. The hydrophilic water supplying layer directly contacts the solar absorber  
480 layer and water can only be transported through the confined hydrophilic pathways. At the same  
481 time, the thermal insulating layer separates the photothermal layer from bulk water and its low  
482 thermal conductivity can further preserve the thermal energy of solar absorbers.

483 Recently, a solar evaporator with 2D water pathways was developed (Figure 11B).<sup>96</sup> Upon  
484 floating on the water, the hydrophilic cellulose paper wrapped on the surface of PS foam got wet  
485 first and then water was pumped up to contact the top GO film for evaporation by capillary forces.  
486 PS foam physically separated the solar absorber layer from the bulk water, and the water  
487 transportation was confined within the 2D cellulose paper. Although the water contact area was  
488 reduced, the GO film could be fed with a sufficient amount of water through the cellulose paper.  
489 The low thermal conductivity of PS foam ( $\sim 0.04 \text{ W}\cdot\text{m}^{-1}\cdot\text{K}^{-1}$ ) effectively prevented the thermal  
490 conduction of heat from the evaporative surface to the bulk water. In this 2D water pathway design,  
491 owing to the balance between the thermal insulation and water transportation, the efficiency of  
492 solar steam generation reached up to 80% under 1 sun illumination. Another solar evaporator  
493 with a 2D water pathway consisted of carbon coated paper affixed to an expanded PS foam, and  
494 it displayed a high efficiency up to 88% under non-concentrated light irradiation of  $1 \text{ kW}\cdot\text{m}^{-2}$ .<sup>131</sup>

495 Solar steam generators with 1D water pathways were also suggested to further decrease  
496 the water contact area. Hu and co-workers developed a jellyfish-like solar evaporator comprising  
497 of porous carbon black/GO as solar absorbers and expanded PS foam with vertically aligned GO  
498 pillars as a substrate.<sup>110</sup> The water transportation was confined to the 1D vertically aligned  
499 microchannels within these GO pillars. Combined with the low thermal conductivity of PS matrix,  
500 which preserved the thermal energy for steam generation, the solar evaporation efficiency  
501 reached up to 87.5% under light irradiation of  $1 \text{ kW}\cdot\text{m}^{-2}$ . Zhu and co-workers developed a solar  
502 evaporator with 3D conical GO films as solar absorbers and a cotton rod as the 1D water

503 pathway.<sup>126</sup> This thermal management enabled a high efficiency of up to 85% under light  
504 irradiation of  $1 \text{ kW}\cdot\text{m}^{-2}$ . The same group carbonized a mushroom (Figure 11E), and its umbrella-  
505 shaped black pileus enabled efficient solar absorption and strong evaporation (Figure 11I).<sup>104</sup> The  
506 fibrous stem with a small cross section enabling efficient water supply confined the water path in  
507 a quasi-1D manner and led to the minimization of heat loss (Figure 11G). The supporting PS foam  
508 with a low thermal conductivity separated the solar absorber layer from the bulk water, mitigating  
509 thermal loss. This carbonized biomass utilized the intrinsic structures and achieved a high solar  
510 conversion efficiency of 78% under 1 sun illumination.

511 The common feature for these 1D/2D water pathway configurations is that the water  
512 transportation part is separated from the supporting substrates to reduce the contact areas of the  
513 evaporative surfaces with water. The water pathways are constructed by hydrophilic materials to  
514 provide adequate water for evaporation, and a thermal insulator separates the solar absorber  
515 from bulk water to allow heat confinement. Therefore, an optimal balance between water supply  
516 and thermal insulation is achieved.

### 517 **3.2.2. Salt-rejection systems for desalination**

518 Recently, several novel designs have been reported for long-term antifouling desalination.<sup>55, 83,</sup>  
519 <sup>130, 132-136</sup> The main mechanism is either to prompt multidirectional diffusion or prevent the  
520 accumulation of salt on the evaporative layer. For conventional solar evaporators, the water is  
521 continuously pumped by the bottom layer to the top hot layer, and salt gradually aggregates on  
522 the evaporative surface under this one-way diffusion. Multidirectional mass transfer on the  
523 evaporative layer can drive the dissolution of salt back to bulk water.

524 To alleviate salt clogging of the evaporative layer, Chen and co-workers fabricated a  
525 floating system, enabling horizontal mass transfer along the solar absorber layer (Figure 12A).<sup>130</sup>  
526 The insulating structure was made from a white cellulose fabric and alternating expanded PS  
527 foam (Figure 12C), which were responsible for water transportation and thermal insulation,

528 respectively. The structure of hydrophilic white fabric combined with the hydrophilic upper  
529 photothermal layer boosted in-plane diffusion on the evaporative surface and thus the dissolution  
530 of the concentrated salt back to the bulk water (Figure 12B, E). There was no salt formed on the  
531 solar evaporator after working for 7 days, but the evaporation efficiency was only around 57% in  
532 3.5% NaCl simulated seawater under 1 sun illumination, arising from the reflective light loss of 15%  
533 from the wetted solar absorber.

534 To achieve high light absorption and salt rejection simultaneously, a wood-based solar  
535 evaporator comprised of an array of channels for multidirectional mass transfer was reported  
536 (Figure 12F).<sup>134</sup> Upon solar evaporation, the drilled millimeter-scale channels had a higher water  
537 flux than the intrinsic micron-size wood channels, which resulted in the lower salt concentration  
538 in the drilled channels than that in the microchannels (Figure 12G). This in-plane concentration  
539 gradient drove the dissolution of salt in the drilled channels back to the bulk water. The steam  
540 generation efficiency of this self-regenerating evaporator remained constant at 75% during  
541 continuous testing for 100 hours in 20 wt% NaCl solution under 1 sun illumination and no salt  
542 accumulation was observed (Figure 12I), whereas a thick layer of salt was formed on the  
543 carbonized wood without drilled channels after 6 hours of operation and its performance was  
544 significantly degraded (Figure 12H).

545 Besides improving the mass transfer on the evaporative surface, Janus structure with a  
546 hydrophobic solar absorber layer and a hydrophilic water pathway can be an effective salt-  
547 rejecting design. Within this structure, water is pumped to contact the hot zone for steam formation,  
548 but salts cannot accumulate on the upper hot layer due to its hydrophobic nature. As a result,  
549 salts can only crystallize at the interface of solar absorber and substrate, which can be quickly  
550 dissolved by the continuously wicking water from the water pathways.

551 A salt-resistant Janus membrane was fabricated with a carbon black (CB) nanoparticles  
552 coating on a hydrophobic polymethylmethacrylate (PMMA) layer for light absorption and

553 hydrophilic polyacrylonitrile (PAN) as the bottom layer for water pumping.<sup>136</sup> Owing to the  
554 presence of the hydrophobic PMMA layer, the salt formation was localized at the interface of  
555 CB/PMMA and PAN layer, and was removed consequently by the wicking water. After testing in  
556 saline water for 16 days, no salt accumulation was observed on the Janus membrane and the  
557 performance remained constant. However, the efficiency was only around 52% under 1 sun  
558 illumination because of insufficient thermal insulation.

559 To improve the efficiency, Que and co-workers incorporated the Janus structure with a  
560 thermal insulator. MXene was employed as the solar absorber and the trimethoxy(1H,1H,2H,2H-  
561 perfluorodecyl) silane modification converted its intrinsic hydrophilic surface to be hydrophobic.  
562 The evaporator was comprised of a hydrophobic MXene membrane, a hydrophilic nonwoven  
563 fabric and a supporting PS foam (Figure 12J).<sup>135</sup> During membrane operation in a saline  
564 environment, no salt accumulation was detected on the hydrophobic MXene surface and the  
565 steam generation efficiency was 71% under 1 sun irradiation, and did not decay over 200 hours  
566 (Figure 12K). In contrast, a huge amount of salt deposited on a hydrophilic MXene membrane  
567 and solar evaporating performance greatly deteriorated over time. Overall, the Janus structure  
568 can reduce the crystallization of salt on the evaporative surface.<sup>137, 138</sup>

569 Although these reported structures successfully alleviate concerns regarding salt-clogging  
570 in saline environments, their evaporation efficiencies are consistently lower compared to  
571 interfacial evaporators with optimal thermal management strategies. For the structures enabling  
572 enhanced mass transfer on evaporative surface, the improved diffusion also results in increased  
573 thermal loss from the hot zone to the bulk water. In the Janus structures, less water can contact  
574 the hydrophobic solar absorbers for vapor generation. These factors contribute to the  
575 compromised evaporation efficiency for the salt-rejection designs. Hence, further improvement  
576 on the thermal management and water transportation in anti-fouling evaporators is required to  
577 achieve higher evaporation efficiency.

#### 578        **4. Water collectors**

579        Water collection is an essential part of the solar-assisted water purification, considering that  
580        production of freshwater is the ultimate goal. A poor design of a water collector can significantly  
581        lower the evaporation efficiency. In most of the reported studies, the performance of the solar  
582        evaporator is analyzed by calculating the evaporating rates in the open air. However, it does not  
583        fully represent the freshwater generation capability of the solar evaporators. Without effective  
584        water collection systems, water generation rates are low as the increased humidity and  
585        condensed water droplets lower the evaporation rates of solar steam generators. However, most  
586        of studies do not include a water collection system, due to the difficulty in designing efficient water  
587        collectors. Only very recently, some researchers have integrated water collection systems with  
588        their solar evaporating system to validate the freshwater generation under real outdoor conditions.  
589        These developments are in preliminary stages and a comprehensive quantitative analysis of  
590        freshwater generation efficiency is still missing.<sup>83</sup> Not surprisingly, a few studies indicate that the  
591        evaporation efficiency decreases after the incorporation of water collectors.<sup>84, 131, 139, 140</sup> In these  
592        studies, the efficiency of water collection from vapor is low, because highly humid environments  
593        and compromised optical absorbance after vapor condensation in the water collector deteriorate  
594        the evaporation. Comprehensive studies about designing water collectors for solar evaporation  
595        are still rare.

596               Recently, surfaces with precisely tailored wettability have been demonstrated to achieve  
597               directional water collection from the humid environment and fast water collection from vapor,  
598               showing great potential for realizing water collection for solar evaporators. Directional water  
599               collection is comprised of three steps: condensation, coalescence, and transportation, which are  
600               significantly affected by the wettability of materials.<sup>141</sup> Moreover, vapor condensation is classified  
601               in two categories: film-wise condensation (FWC) and dropwise condensation (DWC) depending  
602               on the morphology of water droplets.<sup>142, 143</sup> FWC occurs when the vapor condenses on the

603 hydrophilic surface and a continuous thin film forms, whereas discrete droplets with size ranging  
604 from micrometers to millimeters generate when condensing on the hydrophobic surface.<sup>144</sup> The  
605 amount of heat exchange during condensation is very high and DWC exhibits lower heat transfer  
606 resistance than FWC, hence DWC is a preferred mode for condensation.<sup>145</sup> Water droplets grow  
607 up by coalesce with the neighboring droplets and are removed by external force, such as gravity,  
608 after reaching certain size. Good water collectors enable the directional movement of water  
609 droplets to expedite their growth and transportation. Although water droplets inevitably scatter  
610 solar light, the excellent water collector allows fast transportation that can mitigate the negative  
611 effects. Moreover, fast condensation by DWC can avoid the high humidity built-up within the water  
612 collector, which ensures the good evaporation performance. Therefore, high-efficiency water  
613 collection can be achieved only with fine control of both physical and chemical surface properties.

614         Current water collectors in the solar steam generation are generally comprised of a  
615 chamber with a transparent and tilted roof.<sup>58</sup> The solar evaporator locates at the bottom of the  
616 chamber and the whole solar distillation device floats on the water (Figure 13). With sunlight  
617 exposure, the generated vapor condenses into water droplets on the roof of the chamber. The  
618 tilted cover can guide the transportation of water droplets to be collected. Wang and co-workers  
619 designed a self-floating solar distillation device, consisting of a light transparent plastic wall and  
620 cover (Figure 13A).<sup>83</sup> The evaporating chamber and condensing chamber were connected by the  
621 upper part, but separated by a division in the bottom. Upon sunlight irradiation, the solar absorber  
622 layer, in the bottom of evaporating chamber, evaporated the seawater. A solar-powered electrical  
623 fan equipped in the evaporating chamber could generate an air flow field and thus drive the water  
624 vapor into a condensing chamber to generate freshwater (Figure 13B). In addition, the bottom of  
625 condensing chamber was directly in contact with bulk water, which served as a cold source to  
626 expedite the condensation of vapor. The water generation rate of this solar distillation device was

627 0.15 kg·m<sup>-2</sup>·h<sup>-1</sup>. However, this work did not mention the input solar energy to the system, so that  
628 the capability of the device to purify water cannot be fully evaluated.

629         Ho and co-workers assembled a pyramid solar distillation cell and validated purification of  
630 water under natural sunlight conditions.<sup>139</sup> The pyramid model was constructed by transparent  
631 acrylic boards with a carbon sponge (CS) as the solar evaporator locating at the bottom and  
632 troughs on the sides connected with the water collection bag (Figure 13C-D). After placing it on a  
633 lake under sunlight, steam condensed on the pyramid cover and water flowed into the collection  
634 troughs (Figure 13E). The maximum freshwater generation productivity was calculated to be 0.34  
635 kg·m<sup>-2</sup>·h<sup>-1</sup> under one sun illumination. However, without water collector, the water evaporation  
636 rate was 1.15 kg·m<sup>-2</sup>·h<sup>-1</sup>, which was three times higher compared to the water collection rate. The  
637 difference was attributed to the deteriorated evaporation performance after integrating the water  
638 collector in the solar distillation cell. The water collection occurs in the sealed space, so the  
639 humidity is much higher than the open-air condition. It has been reported that the evaporation  
640 rate would decrease linearly with the increase of humidity.<sup>146</sup> Furthermore, when the vapor  
641 condenses on the cover, the resultant water droplets block the incident solar flux to the solar  
642 absorber (Figure 13F). Without fast transportation of these water droplets for collection, solar light  
643 is less available for steam generation. Hence, careful structural design and materials selection  
644 should be made to accelerate the water collection from the vapor.

645         Water sorbents can be used for vapor absorption over a wide range of humidity values.  
646 Silica gels, zeolites, and metal organic frameworks (MOFs) are three types of the most well-  
647 explored water sorbents.<sup>147</sup> Zeolites and silica gels exhibit hydrophilic absorption behaviors. For  
648 silica gels, water molecules are absorbed on the surface via forming hydrogen bonding with the  
649 hydroxyl of silanol groups, so that the presence of silanol groups governs the water uptake  
650 capability.<sup>148</sup> Zeolites are a class of crystalline aluminosilicate materials, and their high affinity to  
651 water molecules is attributed to the electrostatic charged framework and the abundance of extra-

652 framework cations. Chemical structures to increase active sites have been optimized to enhance  
653 the water absorption. An alternative method to produce more active sites is tuning the geometry  
654 of pores. However, these two kinds of materials still suffer from relatively low water uptake. The  
655 zeolites require a high temperature, more than 200 °C, to desorb the water for collection. Owing  
656 to the extraordinary specific surface area and calibrated pore size, MOFs exhibit superior vapor  
657 absorption and attract intensive attention.<sup>149, 150</sup> The water uptake happens via reversibly filling  
658 pores or irreversible capillary condensation in the center of pores.<sup>151</sup> Depending on the pore size,  
659 pore structure, chemical components, and functional groups, the water absorption behavior for  
660 MOFs is diverse. However, due to the periodic thermal energy input requirement, it is difficult to  
661 employ these materials as water sorbents in solar evaporators. Generally, water uptake of water  
662 sorbents occurs at room temperature, and subsequently heat treatment is employed to release  
663 the water. Cyclic heating and cooling significantly increase the difficulty in utilizing water sorbents  
664 for water collection in solar steam generators. Furthermore, a condenser is required to capture  
665 the released water vapor from the sorbents, which makes the water collection more complicated  
666 for the solar evaporator. Below, we further discuss advanced water collectors in terms of their  
667 performance, mechanisms and design principles.

#### 668 **4.1. Bio-inspired design to boost water collection**

669 In nature, animals and plants have evolved biological structures to survive in the arid  
670 environments.<sup>152, 153</sup> These biological structures exhibit unique surface features that are uniquely  
671 tailored to collect water from limited resources under the harsh environmental conditions.  
672 Analyzing and learning from the structures and surface chemistries of these creatures in nature,  
673 researchers have designed biomimetic materials to enable efficient water collection.<sup>154</sup> Below, we  
674 introduce three attractive models in nature, namely spider silk, desert beetle and cacti, for water  
675 collection, and review recent developments in related bio-inspired materials.

##### 676 **4.1.1. Spider silk fiber**

677 Spider silk fiber has an excellent directional water collection capability, which is attributed to the  
678 periodic spindle-knots and joints structure after wetting (Figure 14A-I).<sup>155</sup> Upon placing in a mist,  
679 water starts to condense, then the puffs on the fiber shrink into bumps, which eventually form  
680 periodic spindle-knots with continuous condensation (Figure 14A-B). The wetted spider silk fiber  
681 consists of alternating spindle-knots and joints with a diameter of 21  $\mu\text{m}$  and 6  $\mu\text{m}$ , respectively,  
682 and with a periodicity of  $\sim 90$   $\mu\text{m}$  (Figure 14K). For water collection processes, water condenses  
683 on the joints first and is subsequently transported to spindle-knots after droplets grow. The  
684 directional water movement relies on the structure-induced wettability gradient and difference in  
685 Laplace pressure. Although the chemical composition for the spindle-knots and joints is the same,  
686 the rougher surface morphology for the spindle-knots (Figure 14L-M) makes them more  
687 hydrophilic than the joints (Figure 14N-O), thus driving the water droplets moving from the less  
688 hydrophilic domains (joints) to the more hydrophilic domains (spindle-knots). The two oppositely  
689 curved and connected conical sites locating on the center and edge of the spindle-knot offer non-  
690 equilibrium Laplace pressure difference (Figure 14J), which moves the water droplets from the  
691 joints to the spindle-knots. For the silkworm silk fiber whose surface is smooth, the water collection  
692 efficiency is significantly lower.

693 Jiang and co-workers pioneered the spider silk-inspired fiber for water collection. Artificial  
694 fibers resembling the structure of wetted spider silk were fabricated to fast directional water  
695 collection by dip coating (Figure 14P).<sup>156</sup> A thin PMMA film was coated on the nylon fiber and then  
696 broke into alternating droplets after drying due to Rayleigh instability. The artificial fiber had a  
697 periodicity of 400  $\mu\text{m}$ , and the diameter of spindle-knots and joints are 44  $\mu\text{m}$  and 14  $\mu\text{m}$ ,  
698 respectively. The fabrication was also implemented in large scale; PMMA-knotted nylon fiber was  
699 demonstrated by fluid coating (Figure 14Q), and PMMA-knotted PS fiber and poly (ethylene glycol)  
700 (PEG)-knotted PS fibers were demonstrated using electrospinning/electrospraying methods

701 (Figure 14R).<sup>157-159</sup> After their exposure to moist environments, superior water condensation and  
702 directional water collection were successfully demonstrated on these bio-mimic fibers.

#### 703 **4.1.2. Desert beetles**

704 Stenocara beetles are capable of living in the Namib desert, one of the most arid areas of the  
705 world, because they have unique surface structures on their back enabling water collection from  
706 fog-laden wind (Figure 15A).<sup>160-162</sup> The bumpy back surface is comprised of hydrophilic bumps  
707 distributed on the superhydrophobic matrix (Figure 15B-C). In the morning, beetles face the wind  
708 with their tilted body to capture small water droplets from the fog. Water droplets firstly accumulate  
709 on the hydrophilic bumps after contacting. After the size of accumulated water droplets reaches  
710 a critical volume, the gravitational force overcomes the binding force in the hydrophilic region. Big  
711 water droplets detach from the bump and roll down to the beetle's mouth through the hydrophobic  
712 background.

713 Inspired by the Stenocara beetles, a variety of hydrophilic-hydrophobic micropatterned  
714 surfaces have been designed to achieve directional water collection.<sup>152, 163-165</sup> Pulsed laser  
715 deposition approach with square-patterned stainless-steel mesh as mask was adopted to  
716 construct the array of superhydrophilic Pt squares on the superhydrophobic polydimethylsiloxane  
717 (PDMS) surface (Figure 15D).<sup>166</sup> Water collection involved three steps: (i) small droplets firstly  
718 condensed immediately on the Pt-coated superhydrophilic squares after exposure to water vapor;  
719 (ii) the water droplets coalesced with the neighboring ones and accumulated to form bigger  
720 droplets; and (iii) when the size of the water droplets reached a critical value, the gravitational  
721 force caused them to roll down and be collected with concomitant removal of the droplets along  
722 the path, releasing the area for condensation (Figure 15E). The square pattern with side length  
723 of 50  $\mu\text{m}$  on the superhydrophobic substrate exhibited maximum water collection rate of 0.053  
724  $\text{kg}\cdot\text{m}^{-2}\cdot\text{h}^{-1}$ , which was higher than PDMS coated-superhydrophobic surface and Pt-nanoparticles  
725 coated superhydrophilic surface, 0.03  $\text{kg}\cdot\text{m}^{-2}\cdot\text{h}^{-1}$  and 0.04  $\text{kg}\cdot\text{m}^{-2}\cdot\text{h}^{-1}$ , respectively.

726 To further augment the directional water collection, an array of straight hydrophilic micro-  
727 tracks on the superhydrophobic silicon substrate was fabricated by stencil lithography (Figure  
728 15F).<sup>167</sup> After condensing on the hydrophobic regions, water droplets directionally migrated to the  
729 nearby hydrophilic tracks because of the difference in wettability between two domains. At the  
730 same time, hydrophilic track acted as a fast transport pathway. The water droplets on the  
731 hydrophilic track would be accumulated into one bulge, which was driven by the Laplace pressure  
732 difference. These two kinds of directional movements contributed to the outstanding water  
733 collection performance for the hybrid surface (Figure 15G). The highest efficiency of  $0.3 \text{ kg}\cdot\text{m}^{-2}\cdot\text{h}^{-1}$   
734 was observed on the substrate micropatterned with a hydrophilic track with width and spacing  
735 distance of  $300 \text{ }\mu\text{m}$  and  $3000 \text{ }\mu\text{m}$ , respectively, which was much higher than the isotropically  
736 hydrophobic ( $0.14 \text{ kg}\cdot\text{m}^{-2}\cdot\text{h}^{-1}$ ) and hydrophilic surface ( $0.07 \text{ kg}\cdot\text{m}^{-2}\cdot\text{h}^{-1}$ ) (Figure 15H).

#### 737 **4.1.3. Cacti**

738 As a prevailing plant in Chihuahua desert, Cactus *O. microdasys* possesses a unique structure  
739 of spines to capture water from fog (Figure 16A). The needle-like spines grow on the  
740 hemispherical trichomes, and their length and diameter range from  $800 \text{ }\mu\text{m}$  to  $2500 \text{ }\mu\text{m}$  and  $30$   
741  $\mu\text{m}$  to  $65 \text{ }\mu\text{m}$ , respectively (Figure 16B-C). The spines are comprised of different structural  
742 features (Figure 16D): oriented barbs in the tip (Figure 16E,H), gradient grooves in the middle  
743 (Figure 16G), and belt-structured trichomes in the base (Figure 16F).<sup>168</sup> After placing in a mist,  
744 the water droplets can gradually grow on the spines and move from tip to base (Figure 16I), even  
745 if the tip is pointed down (Figure 16L). The efficient water collection depends on the gradient of  
746 Laplace pressure and wettability along the spines (Figure 16J). The density of microgrooves on  
747 tip of spines is higher than on base, which makes the tip more hydrophobic, thus water droplets  
748 collected on tip move to the base by the surface-energy difference. The gradually decreasing  
749 curvature from tip to base of spines causes the Laplace pressure at the tip to be larger than that  
750 at the base (Figure 16K), which is another reason for the directional motion of water droplets.

751 Cacti spine-like conical micro-tips patterns were fabricated to mimic the high performance  
752 of water harvesting.<sup>169</sup> In order to overcome the limited-scale fabrication of conventional template-  
753 assisted methods,<sup>170</sup> cacti-mimicking patch was fabricated in large scale with magnetic particle-  
754 assisted molding (Figure 16O).<sup>171</sup> A mixture of magnetic particles (MPs) with PDMS was exposed  
755 to magnetic field, and MPs tended to arrange along the magnetic field (Figure 16M). Driven by  
756 the polymer-induced capillary force, the binding of the preformed primary arrays led to a micro-  
757 needle pattern on the surface (Figure 16N). Once exposed the mist, a continuous and  
758 spontaneous transportation of water droplets was noted on the surface of microtip (Figure 16Q).  
759 The Laplace difference along the conical microtip could transport the water droplets from the tip  
760 to base even with the pattern upside down (Figure 16Q). The cacti-inspired water collector was  
761 fabricated by assembling these hydrophobic microtip patches on the surface of a hydrophilic  
762 cotton sphere (Figure 16R). Water collected by micro-tip array could be absorbed by the cotton  
763 matrix, which was subsequently stored in the container. Placing in the fog with velocities of 20–  
764 30, 45–50 and 70  $\text{cm}\cdot\text{s}^{-1}$  for 10 minutes, the cacti-inspired water collector captured 2 mL, 3 mL,  
765 and 5 mL water, respectively, whereas only 0.3 mL, 0.7 mL, and 2 mL water were collected for  
766 the bare cotton spherical water collector, respectively.

767 These biomimetic designs with tailored hydrophilic and hydrophobic regions enable water  
768 collection at significantly higher efficiency than the purely hydrophilic or hydrophobic surfaces.  
769 The progress in the biomimetic water collectors is expected to inspire researchers in the solar  
770 steam generation field to design efficient water collectors based on these principles and facilitate  
771 solar evaporators into real-world applications. As noted above, fine controls over the microscale  
772 structure and spatial control of the wettability are critical to enhance the vapor condensation,  
773 droplets coalescence, and water transportation. Moreover, to maximize the solar steam  
774 production and water collection, the design principles discussed above needs to be carefully  
775 balanced with light transmission across the water collectors. We expect that in the next decade,

776 water collectors in the solar steam generators will undergo significant improvements to ultimately  
777 make the solar steam generators a compelling technology for purifying water.

## 778 **5. Water production cost analysis**

779 To realize the solar steam generation for water production, it is critical to understand the cost  
780 associated with producing water with solar steam generation using the interfacial evaporator  
781 technologies. Recently, Chen and co-workers developed the low cost solar still to collect water  
782 generated by solar steam generation.<sup>130</sup> Considering solar steam generation aims to supply  
783 drinking water at a low cost, we took the cost of materials to estimate water production cost by  
784 different solar evaporators. In addition to the cost associated with a solar evaporator, the cost for  
785 building a solar still is estimated to be  $\sim \$1.7 \cdot \text{m}^{-2}$ . The solar evaporator life span was assumed to  
786 be two years to calculate the cost, because the amount of foulant accumulated on solar still during  
787 two years would not be high enough to cause it to sink in the bulk water, according to previous  
788 study.<sup>130</sup> This represents a conservative estimate of the cost of solar evaporator.<sup>31</sup> In water  
789 collection, solar evaporation efficiency dropped significantly from 56% to 24% due to optical loss  
790 by water droplet forming on transparent windows.<sup>130</sup> Most of solar steam generation studies do  
791 not include the water collection efficiency, rather they provide only solar evaporation efficiency.  
792 We converted solar evaporation efficiency to water collection efficiency by multiplying scale factor  
793 (0.43) calculated by dividing water collection efficiency by solar evaporation efficiency in Chen  
794 group's study.<sup>130</sup> For cost analysis, solar evaporation efficiencies for different solar evaporators  
795 were converted to water collection efficiencies with the abovementioned scale factor.

796 For comparison, we chose one solar evaporator in each solar absorber section (plasmonic  
797 nanostructure, nanocarbon materials, and polymers). To avoid any price difference from supports,  
798 solar evaporators relying on cellulose supports were selected, and the unit price of cellulose  
799 supports is  $\$9.2 \cdot \text{m}^{-2}$ , obtained from Sigma-Aldrich. Also, we obtained the unit cost of raw  
800 photothermal materials from Sigma-Aldrich and accounted the amount of materials employed for

801 fabricating a solar evaporator. Finally, the total cost for a solar evaporator was estimated and  
802 listed in the Table 2.

803 To calculate the water production during the life span of a solar evaporator, we used  
804 following equation:

$$805 \quad m = \frac{\alpha * \eta * E}{\Delta H_{latent}}$$

806 where  $m$  is the water produced over two years,  $\alpha$  (0.43) is the scaling factor to convert the  
807 evaporation efficiency to the water collection efficiency,  $\eta$  is the evaporation efficiency,  $E$  is the  
808 solar energy over two years, and  $\Delta H_{latent}$  is the latent enthalpy for water. Considering the average  
809 daily solar irradiance to be around  $\sim 5 \text{ kWh} \cdot \text{m}^{-2} \cdot \text{day}^{-1}$ , we can calculate the amount of solar energy  
810 impinging on the solar evaporator over its estimated life period of two years. Considering the  
811 materials cost for a solar evaporator and the produced water amount, we calculated the unit cost  
812 to produce clean water by solar steam generation (Table 2). Clearly, material costs are important  
813 as these technological advances for real-world applications. Solar evaporation efficiency reached  
814 almost 90% for recent developed solar evaporators, indicating that there is not much room for  
815 improvement in terms of efficiency. On the other hand, more work is needed to improve the  
816 efficiency of water collection. In both cases, materials cost and efficiency needs to be considered  
817 to maximize the cost-to-benefit ratio of these devices.

818 **Table 2. Cost analysis for water production by solar steam generation. \***

Materials	solar evaporator cost ( $\text{\$}\cdot\text{m}^{-2}$ )	Solar still building cost ( $\text{\$}\cdot\text{m}^{-2}$ )	Solar evaporation efficiency	Expected water collection efficiency	Water production cost ( $\text{\$}\cdot\text{m}^{-2}\cdot\text{L}^{-1}$ )
AuNR/AuNS/Paper <sup>50</sup>	1468	1.7	87% at 2.3 $\text{kW}\cdot\text{m}^{-2}$	37.4% at 2.3 $\text{kW}\cdot\text{m}^{-2}$	0.675
RGO/BNC <sup>22</sup>	1217		83% at 10 $\text{kW}\cdot\text{m}^{-2}$	36.7% at 10 $\text{kW}\cdot\text{m}^{-2}$	0.570
PPy-coated airlaid paper <sup>80</sup>	12.6		82.3% at 1 $\text{kW}\cdot\text{m}^{-2}$	35.4% at 1 $\text{kW}\cdot\text{m}^{-2}$	0.007

819 \* The cost analysis here provides a relative comparison basis of different materials and identifies  
820 the needs for improvement rather than accurately determines the cost for solar evaporator  
821 construction.

## 822 **6. Photothermal membrane distillation (PMD)**

823 As we discussed above, solar evaporators have to address effective water collectors. To this end,  
824 integrating the interfacial solar heating with membrane distillation can be a promising alternative  
825 approach. Vapor generation in PMD is similar to solar steam generation, which occurs at the  
826 water-air interface and relies on the photothermal heating under solar illumination. The biggest  
827 difference is the structure of the evaporative interface. In the solar evaporators, the photothermal  
828 membrane is placed on the surface of the bulk water that needs to be purified. In the case of  
829 PMD, interfacial structure is reversed, and thus the generated vapor moves in an opposite  
830 direction compared to the solar evaporator (Figure 17A, B). The unique evaporative interface  
831 contributes to the facile water collection for PMD.

832 MD is a thermal-driven membrane desalination process.<sup>172</sup> In MD, the temperature  
833 difference between the hot feed water side and the cold distillate side results in a transmembrane  
834 temperature gradient, which generates a vapor pressure difference on the two sides of the  
835 membrane.<sup>173</sup> The water can thus evaporate on the hot feed side to form vapor, which transports  
836 across the microporous and hydrophobic membrane, and condenses on the cold distillate side.  
837 In conventional MD, which uses hot feed water, the membrane surface temperature gradient ( $T_{s, \text{feed}} - T_{s, \text{distillate}}$ )  
838 is always less than the temperature difference between the bulk feed and distillate  
839 ( $T_{b, \text{feed}} - T_{b, \text{distillate}}$ ). Such a phenomenon is known as the temperature polarization,<sup>174</sup> which impairs  
840 the overall MD performance via lowering the transmembrane temperature gradient and vapor flux.

841 In just the past two years, photothermal membrane distillation (PMD), which combines the  
842 MD with solar-driven heating, has gained significant interest.<sup>30, 175, 176</sup> In PMD, a hydrophobic  
843 membrane is modified with photothermal materials, which can harvest solar energy and generate  
844 localized heat on the membrane surface, thus facilitating a driving force for vapor transport (Figure  
845 18). The localized heating on membrane surface can help to increase top membrane surface  
846 temperature ( $T_{s, \text{feed}}$ ), therefore alleviating temperature polarization effects on MD performance.<sup>36,</sup>  
847 <sup>108, 177</sup>

### 848 **6.1. PMD advantages and disadvantages**

849 PMD shares most advantages of common MD configurations. PMD is operable at lower  
850 temperatures than boiling and lower pressures than RO, making it less energy intensive.<sup>178</sup> The  
851 low hydrostatic pressure on membranes helps to minimize fouling problems, making PMD suitable  
852 for hypersaline or highly polluted wastewater.<sup>172</sup> Most importantly, PMD uses solar energy, which  
853 is highly abundant, accessible, and sustainable, as the main energy source. The use of solar  
854 energy reduces the electricity input compared to conventional MD, making PMD highly suitable  
855 as a decentralized technique of clean water generation for household or remote areas.<sup>179</sup> The  
856 high membrane surface temperature helps to reduce the temperature polarization effects.

857 Meanwhile, PMD can be combined with low grade heat energy sources, such as waste heat from  
858 industrial plants, geothermal energy, or flow back water from unconventional oil and gas recovery  
859 systems.<sup>108</sup> Moreover, compared with solar steam generation, which suffers from the lack of  
860 efficient clean water collection systems, PMD can easily collect purified water using distillate  
861 pumping, vacuum or air gap systems (Figure 17B). The use of highly hydrophobic membranes in  
862 the PMD process leads to high salt rejection (commonly >99%) and minimizes the salt  
863 accumulation problems, which can potentially happen in the solar steam generation. The  
864 shortcomings of current PMD systems include a low water generation rate as compared to other  
865 commercial pressure-driven filtration processes such as RO and ultrafiltration (UF). PMD  
866 application can also be challenging when treating highly turbid water because the penetration of  
867 sunlight to membrane surface can be disrupted by particles in the water, thus requiring  
868 pretreatment process as RO and UF processes need.

## 869 **6.2. Recent materials research progress in PMD**

870 In the past two years, significant progress has been made in both configuration design and  
871 membrane modification of PMD systems. Current PMD systems can be divided into four  
872 configurations: a passive MD without pumping systems (Figure 19A), PMD in a direct contact  
873 membrane distillation system (Figure 19B), PMD in a vacuum membrane distillation system  
874 (Figure 19C), and PMD with multiple latent heat recovery systems (Figure 19D). Figure 19A  
875 depicts a PMD system without pumping systems, in which cold saline water is on top of the  
876 photothermal membrane. The vapor pressure difference across the membrane causes the vapor  
877 on the feed side of the membrane to penetrate the membrane and condense on the bottom device  
878 surface. Fujiwara and co-workers have demonstrated several PMD systems in such a  
879 configuration using anodized alumina membranes modified with azobenzene dyes.<sup>180-182</sup> Such a  
880 configuration does not require external energy and thus is suitable for portable devices, although  
881 the clean water generation rate might be small.

882 To increase the water flux, direct contact membrane distillation (DCMD) configuration  
883 has been employed (Figure 19B) in some recent works.<sup>107, 108, 177</sup> In 2017, a nanophotonics-  
884 enabled solar membrane distillation (NESMD) system was introduced.<sup>177</sup> Using carbon black (CB)  
885 NPs coated PVDF membranes, the PMD system generated a water flux of  $0.22 \text{ kg}\cdot\text{m}^{-2}\cdot\text{h}^{-1}$  under  
886  $0.7 \text{ kW}\cdot\text{m}^{-2}$  with a solar conversion efficiency of 21.45%. Theoretical models showed that along  
887 the module, NESMD system had increasing membrane surface temperature,  $\Delta T$  across  
888 membrane, and flux, while MD system had degradation in these properties (Figure 19E-G). The  
889 authors suggested that increasing NESMD unit size would help increase its distillate flux. And  
890 slower feed velocities, larger lengths and widths of the module, and higher ambient temperature  
891 can facilitate the NESMD performance. Li and co-workers also synthesized PMD membranes with  
892 carbon black nanoparticles and  $\text{SiO}_2/\text{Au}$  nanoshells, and showed a water flux increase of up to  
893 33.0% under  $1 \text{ kW}\cdot\text{m}^{-2}$  sunlight irradiation compared to a dark condition by using CB.<sup>107</sup> However,  
894 this work utilized slightly heated water ( $35 \text{ }^\circ\text{C}$ ) as the feed water, making the overall thermal  
895 efficiency to be higher (74.6%) compared to their previous work due to the lower conductive loss  
896 from the membrane surface to feed water. Thus, the applicability of the efficiency with water at  
897 room temperature cannot be evaluated directly.

898 Recently, inspired from natural systems, Jun and co-workers synthesized a simple, stable,  
899 and scalable PDA-coated PVDF membrane for efficient solar-driven PMD in DCMD configuration  
900 (Figure 19H).<sup>108</sup> The PDA-coated PVDF membrane was modified to be hydrophobic via a facile  
901 fluoro-silanization method using (tridecafluoro-1,1,2,2-tetrahydrooctyl)-trichlorosilane (FTCS),  
902 leading to a water contact angle of  $125.5^\circ$ . The FTCS-PDA-PVDF membrane achieved a water  
903 flux of  $0.49 \text{ kg}\cdot\text{m}^{-2}\cdot\text{h}^{-1}$  (45% thermal efficiency) treating 0.5 M NaCl feed water solutions ( $20 \text{ }^\circ\text{C}$ )  
904 under  $0.75 \text{ kW}\cdot\text{m}^{-2}$  solar irradiation. This performance was attributed to the broad light absorption  
905 and outstanding photothermal conversion properties of PDA. In addition, the membrane showed  
906 great wetting resistance, high salt rejection ( $>99.9\%$ ), and chemical/mechanical robustness owing

907 to the extremely stable underwater adhesion of the PDA. In this work, they also showed that fast  
908 feed flow rates decrease the PMD performance (e.g., the permeate water flux) and thermal  
909 efficiency (Figure 19I-J), which was attributed to more significant heat loss to the bulk feed water.

910 In another configuration, vacuum membrane distillation (VMD) has also been used  
911 because a vacuum system can facilitate vapor transport and collection in PMD (Figure 19C).<sup>36</sup>  
912 Politano and co-workers used silver nanoparticles (Ag NPs) as a photothermal material for PMD  
913 in a VMD system.<sup>36</sup> Prepared by phase inversion methods, Ag NPs loaded PVDF membranes  
914 achieved a high water flux ( $25.7 \text{ kg}\cdot\text{m}^{-2}\cdot\text{h}^{-1}$ ) under UV irradiation, 11 fold higher than the  
915 membrane without Ag NPs.

916 To decrease heat loss and utilize heat more efficiently, new PMD modules were also  
917 developed via multiple latent-heat recovery systems (Figure 19D). Zhou and co-workers recently  
918 developed a compact PMD system combining several layers of evaporator (PVA sponge), MD  
919 membrane (PVDF-hexafluoropropylene (HFP)), and condenser.<sup>183</sup> A commercial cermet-coated  
920 aluminum alloy substrate was used as the solar absorber. In this system, the latent heat from  
921 vapor condensation was recycled for further water evaporation. The system with two layers of  
922 PVDF-HFP membranes was demonstrated to achieve a water flux of  $1.02 \text{ kg}\cdot\text{m}^{-2}\cdot\text{h}^{-1}$  under 1  
923  $\text{kW}\cdot\text{m}^{-2}$  solar irradiation (72% solar efficiency). Chiavazzo and co-workers also reported a passive  
924 solar thermal distiller (does not require external energy),<sup>184</sup> which also consisted of multiple  
925 evaporation/condensation layers. This system produced  $1.24 \text{ kg}\cdot\text{m}^{-2}\cdot\text{h}^{-1}$  under  $0.7 \text{ kW}\cdot\text{m}^{-2}$  solar  
926 illumination when tested outdoors in the summer at Torino, Italy.

927 New PMD membranes with novel materials continue to emerge from ongoing research  
928 efforts. For example, owing to the superb light absorption and photothermal conversion properties,  
929 two-dimensional (2D) materials have also been used in recent years for PMD, including MXene<sup>185</sup>  
930 and rGO<sup>186</sup>. Chew and co-workers synthesized MXene-coated PVDF membranes, and  
931 demonstrated that the photothermal properties of MXene were beneficial in conferring a 12%

932 decrease in the energy consumed by the heater per unit volume of distillate.<sup>185</sup> Jiang and co-  
933 workers coated polytetrafluoroethylene (PTFE) membrane with GO, rGO, and PDA-rGO, and  
934 showed that these membranes achieved 28.6%, 64.3%, and 78.6% water vapor flux increase,  
935 respectively, compared with the bare PTFE membranes in PMD performance.<sup>186</sup> This better  
936 performance was attributed to the higher photothermal conversion efficiency of graphene-based  
937 materials and their low-friction pathways for the ultra-fast transport of water molecules.

938 In general, the materials selection of solar absorbers for the PMD is similar to that of solar  
939 steam generation, which is based on broadband solar absorption and high light trapping. However,  
940 the photothermal materials in PMD applications require higher underwater adhesion and  
941 mechanical stability compared to solar steam generators. Such chemical and mechanical stability  
942 is critical to minimize the possibility of these materials getting released into feed water or distillate,  
943 causing environmental concerns. Moreover, all membranes for PMD should possess high  
944 hydrophobicity to prevent the permeance of bulk water and high porosity to allow vapor  
945 penetration and high water flux.

### 946 **6.3. Challenges and future directions of PMD**

947 PMD is a promising thermally-driven membrane-based desalination technique while it still faces  
948 many challenges. The cost of membrane synthesis and module designs should be lowered to  
949 meet the needs of widespread commercial applications. While PMD can target portable, modular,  
950 household, or decentralized applications due to low electricity input and easy operation,  
951 development of advanced PMD membranes and devices are still necessary to help increase clean  
952 water generation rates and energy efficiency, thus eventually making PMD competitive with other  
953 currently available water treatment techniques and applicable in real applications.

## 954        **7. Conclusions and outlook**

955        In this review, we discussed the recent research on materials for developing highly efficient solar  
956        evaporators, involving enhanced solar light harvesting, thermal management, water  
957        transportation, and water collection. Great strides have been made in the design and synthesis  
958        of advanced materials and optimal structures for the three key components of solar evaporators:  
959        solar absorbers, substrates, and water collectors (Figure 20). This technology is a promising  
960        solution to alleviate water scarcity: it offers high energy efficiency, simplicity, and the possibility of  
961        utilizing renewable and environmentally-friendly resources. While the merits of this technology  
962        have been extensively demonstrated, there are still multiple challenges to real world application.

963                First, most current studies do not provide the analysis of cost or scalability of constructing  
964        the solar evaporators, so it is difficult to evaluate their actual potential for the real-world  
965        implementation. The costs of materials, fabrication of interfacial evaporators, and lifetime  
966        maintenance need to be comparable to or lower than those of existing desalination and  
967        wastewater treatment techniques to facilitate the transition of the technology to the real-world. In  
968        particular, scalability determines the competitiveness of these technologies in massive purification  
969        of wastewater or seawater. Future works should focus more on the developing energy efficient  
970        solar evaporators that can be easily scaled up with inexpensive materials and cost-effective  
971        processing methods.

972                Stability is also a key to long-term operation, but most studies do not provide a  
973        comprehensive insight into the robustness of interfacial evaporators in outdoor operation for an  
974        extended duration. The materials may degrade after interacting with salts and bacteria in river  
975        and seawater, and the structures may deteriorate from exposure to sunlight, heat, wind, and rain.  
976        The deterioration of the evaporators leads to lower efficiency, and the disassembled products  
977        (often nanoscale materials with unknown toxicity) are a burden on the environment. Moreover, it  
978        increases the cost associated with the replacement, maintenance, and restoration. Thus, the long-

979 term stability of solar evaporators under outdoor condition should be fully evaluated.  
980 Complementary research efforts should also focus on developing robust solar evaporators that  
981 are chemically/mechanically/thermally stable in real-world applications.

982         Additionally, a more systematic study on the environmental effects on solar evaporators  
983 is needed. During the outdoor operation, the solar-driven evaporation will be affected by diverse  
984 factors, such as air pressure, humidity, temperature, and wind. These variables complicate  
985 comparisons of the outdoor performance of current solar evaporators across different laboratories.  
986 It is important to understand the effect of these environmental factors on the solar evaporators  
987 and standardize the testing and reporting methods for objectively assessing the merits and  
988 shortcomings of interfacial evaporators using different materials and structures. As highlighted by  
989 Zhu and co-workers, standard testing methods and quantitative descriptors, such as indoor  
990 experimental parameters (e.g., ambient temperatures, humidities, and wind speeds), set-ups (e.g.,  
991 size and uniformity of light spots to solar absorbers, distances of solar absorbers to beaker lips,  
992 beaker walls, and light sources), measurement techniques (e.g., accurate measurement light  
993 intensities and evaporation temperatures), and performance evaluations (e.g., dark evaporations),  
994 should be established.<sup>187</sup>

995         While most previous reports highlight the efficiency of solar evaporation, they did not  
996 incorporate water collection into their systems or determine the freshwater production rates and  
997 efficiencies with water collection. Clearly, these factors are essential to compare solar evaporation  
998 technology with existing desalination technologies. Typically, studies merely measure the  
999 evaporation in an open and constant environment, which is significantly different from the  
1000 evaporation after integrating with water collectors. Water is usually collected within a sealed space,  
1001 and the evaporation rate is significantly different in such a highly humid environment. In addition,  
1002 vapor condenses on the water collector and the formed water droplets cause light reflection, which  
1003 further lowers the evaporation rate. Because converting saline water to freshwater is the ultimate

1004 goal of solar steam generation, future work should also focus on designing innovative water  
1005 collectors that maintain high evaporation efficiencies and high fresh water production rates.

1006           The lack of industry participation also delays the commercialization of this technique.  
1007 Researchers mainly focus on developing novel materials and structural designs to maximize the  
1008 evaporation efficiency and to a large extent overlook the real-world problems that confront with  
1009 the implementation of these technologies. Considering that great strides have been made in  
1010 evaporation efficiency through novel photothermal and support materials and novel interfacial  
1011 evaporator designs in the past few years, involving industrial partners can support fast translation  
1012 of the technology from the current stage to real applications.

1013           Despite the challenges in advancing to practical applications, the intrinsic advantages of  
1014 solar-driven evaporation make it a promising solution for addressing water scarcity around the  
1015 world. Continued innovation and advances in materials selection and engineering will remain  
1016 critical as we gear to promote these technologies from laboratory scale to large scale real-world  
1017 applications.

1018

1019

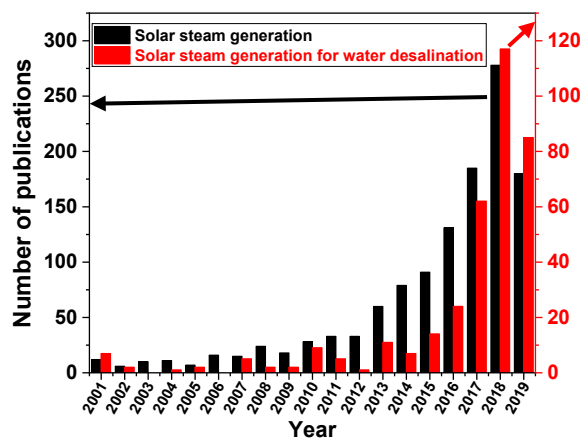
1020

1021

1022

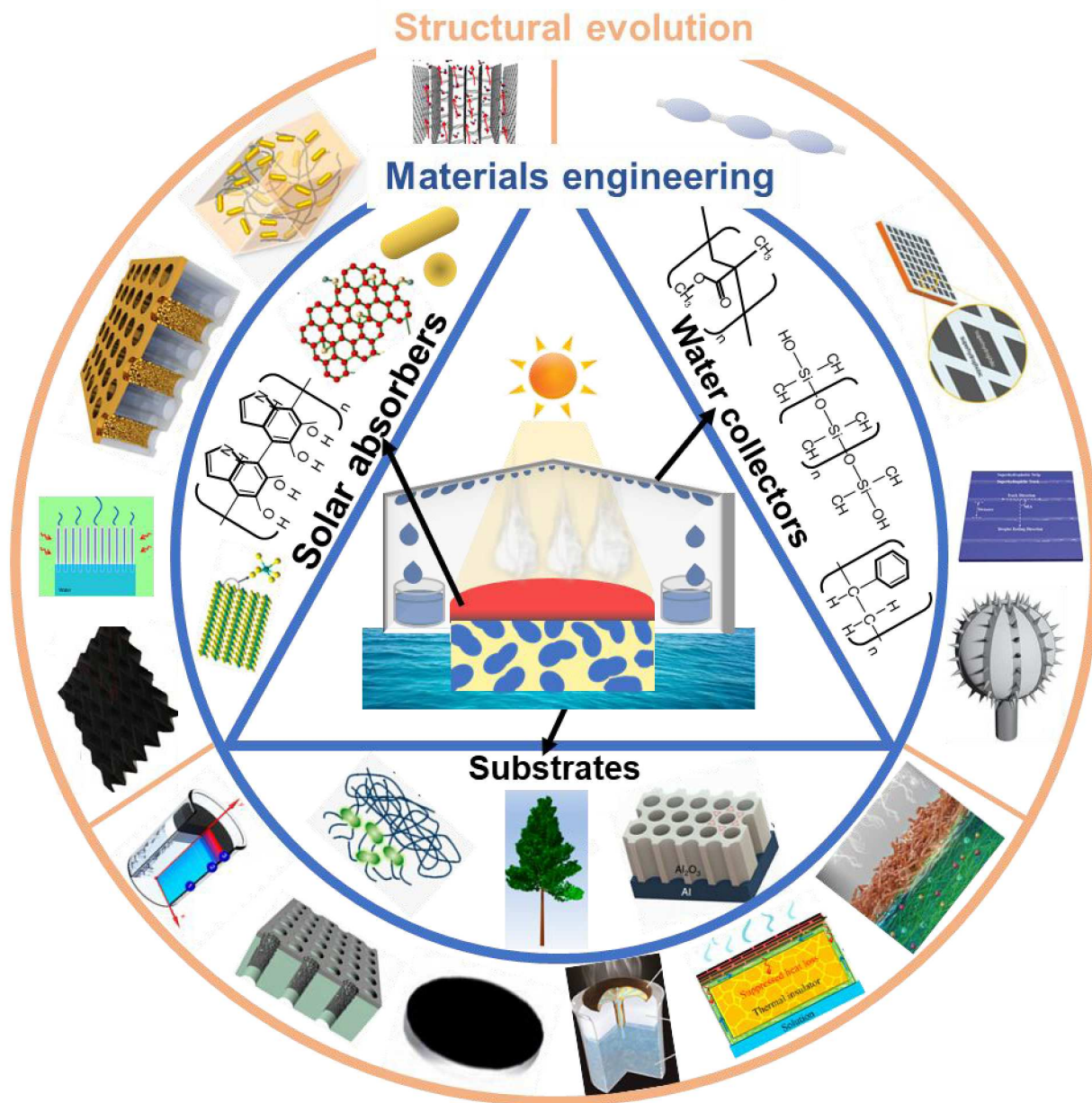
1023

1024

1025 **Figures**

1026

1027 Figure 1. Number of research articles published from 2001 to July 15, 2019 with key words of “solar steam  
1028 generation” for all applications and “solar steam generation for water desalination” highlighting the rapid  
1029 surge in research activity within the past few years (data source: Web of Science).

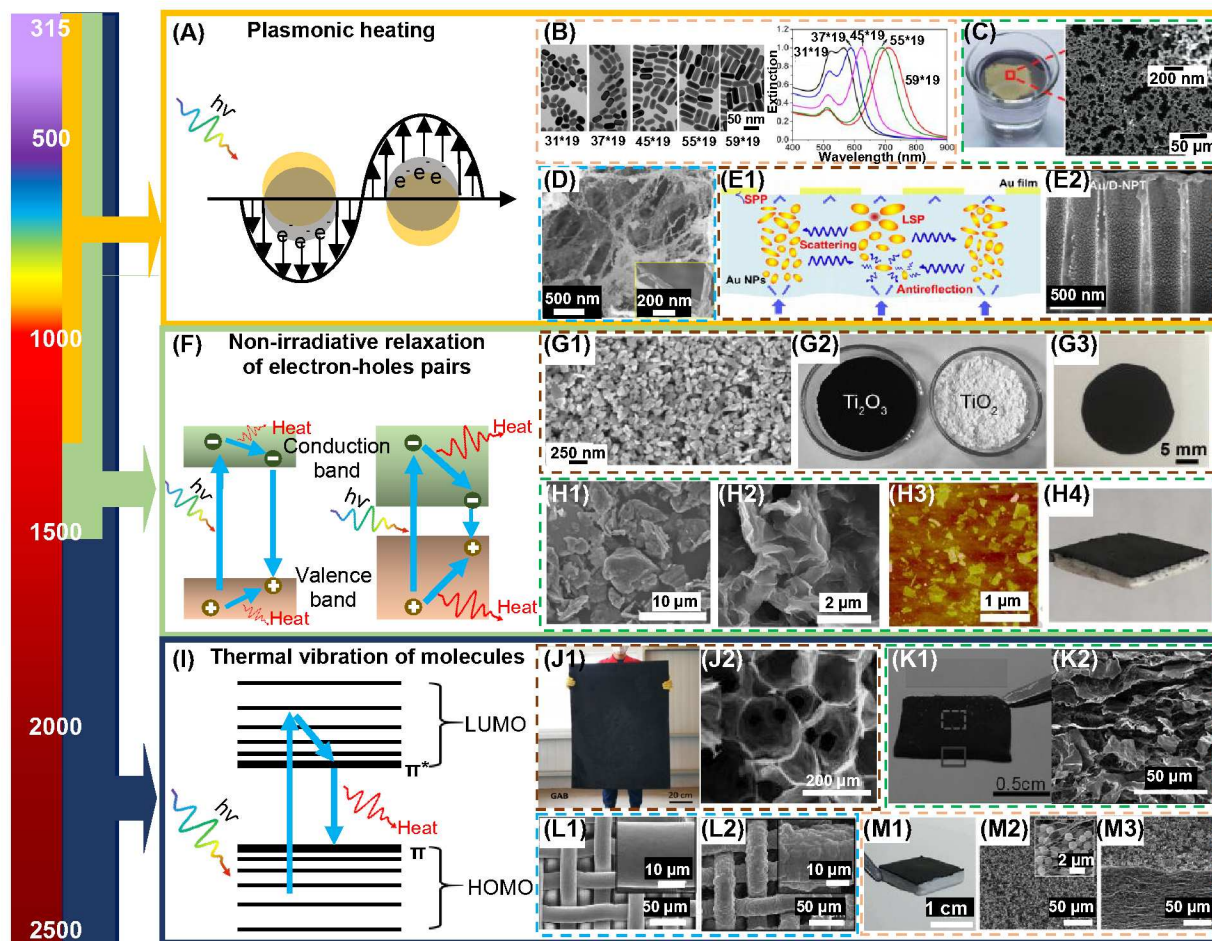


1030 Figure 2. Schematic showing the key aspects of solar steam generators described in this review. Solar  
 1031 absorbers, substrates, and water collectors are reviewed based on materials selection and structure design.  
 1032 Reproduced with permission.<sup>10, 21, 40, 49, 56, 75, 77, 90, 96, 102, 104, 121, 136, 166, 167, 171</sup> Copyright 2017 American  
 1033 Chemical Society. Copyright 2015 American Chemical Society. Copyright 2016 American Association of  
 1034 Science. Copyright 2018 Cell Press. Copyright 2018 American Chemical Society. Copyright 2016 American  
 1035 Chemical Society. Copyright 2018 Elsevier. Copyright 2016 Springer Nature Publishing AG. Copyright 2014  
 1036 Springer Nature Publishing AG. Copyright 2017 Royal Society of Chemistry. Copyright 2017 Wiley-VCH.  
 1037 Copyright 2016 National Academy of Sciences. Copyright 2018 Wiley-VCH. Copyright 2017 Wiley-VCH.  
 1038 Copyright 2017 Wiley-VCH. Copyright 2014 Wiley-VCH.

1039

1040

1041



1042

1043 Figure 3. Schematic illustration depicting the mechanism of LSPR of plasmonic nanospheres (A), non-  
 1044 irradiative relaxation of electron-holes pairs (F) and thermal vibration of organic molecules (I). (B) TEM  
 1045 images of gold nanorods (AuNR) with similar diameter and different lengths, and the corresponding  
 1046 extinction spectra of an AuNR solution. Reproduced with permission.<sup>44</sup> Copyright 2012 American Chemical  
 1047 Society. (C) Photograph of a floating film with gold nanoparticles at the air–water interface, and  
 1048 corresponding SEM images of the film under low and high magnification. Reproduced by permission.<sup>43</sup>  
 1049 Copyright 2014 Wiley-VCH. (D) Cross-section SEM image of plasmonic aerogel, revealing dense and  
 1050 uniform adsorption of AuNR on the nanofibers of BNC aerogel. Reproduced by permission.<sup>10</sup> Copyright  
 1051 2015 American Chemical Society. Schematic illustration (E1) and SEM image (E2) of cross section of the  
 1052 AAO membrane deposited with gold nanoparticles with different shapes and sizes. Reproduced with  
 1053 permission.<sup>49</sup> Copyright 2016 American Association of Science. (G) Optical properties of  $\text{Ti}_2\text{O}_3$   
 1054 nanoparticles. (G1) SEM image of the  $\text{Ti}_2\text{O}_3$  nanoparticles. (G2) Photograph of the  $\text{Ti}_2\text{O}_3$  nanoparticles (left)  
 1055 and commercially available  $\text{TiO}_2$  powders (right). (G3) Photograph of  $\text{Ti}_2\text{O}_3$  nanoparticles deposited on  
 1056 cellulose membrane. Reproduced with permission.<sup>61</sup> Copyright 2017 Wiley-VCH. (H) Size effect on optical  
 1057 properties of  $\text{MoS}_2$ . SEM images of bulk  $\text{MoS}_2$  (H1) and chemically exfoliated  $\text{MoS}_2$  (ce- $\text{MoS}_2$ ) (H2). (H3)  
 1058 AFM image of ce- $\text{MoS}_2$  nanosheets deposited onto a silicon substrate. (H4) Optical image of ce- $\text{MoS}_2$ /BNC  
 1059 aerogel. Reproduced with permission.<sup>56</sup> Copyright 2018 Elsevier. Photograph (J1) and corresponding  
 1060 cross-section SEM image (J2) of a large-size and structurally intact rGO aerogel with an area of about 1  
 1061  $\text{m}^2$ . Reproduced with permission.<sup>79</sup> Copyright 2018 American Chemical Society. (K) Structure of rGO/BNC  
 1062 aerogel. Optical image (K1) and cross-section SEM image (K2) of rGO/BNC aerogel. Reproduced with  
 1063 permission.<sup>22</sup> Copyright 2016 Wiley-VCH. SEM images of the original smooth stainless-steel mesh surface  
 1064 (L1), and the PPy-coated mesh surface with microstructures (L2). Reproduced with permission.<sup>83</sup> Copyright  
 1065 2015 Wiley-VCH. (M) Structure of bilayer PDA/BNC aerogel. Optical image (M1), SEM images of top

1066 surface (M2) and cross section (M3) of PDA/BNC aerogel. Reproduced with permission.<sup>90</sup> Copyright 2017  
1067 Royal Society of Chemistry.

1068

1069

1070

1071

1072

1073

1074

1075

1076

1077

1078

1079

1080

1081

1082

1083

1084

1085

1086

1087

1088

1089

1090

1091

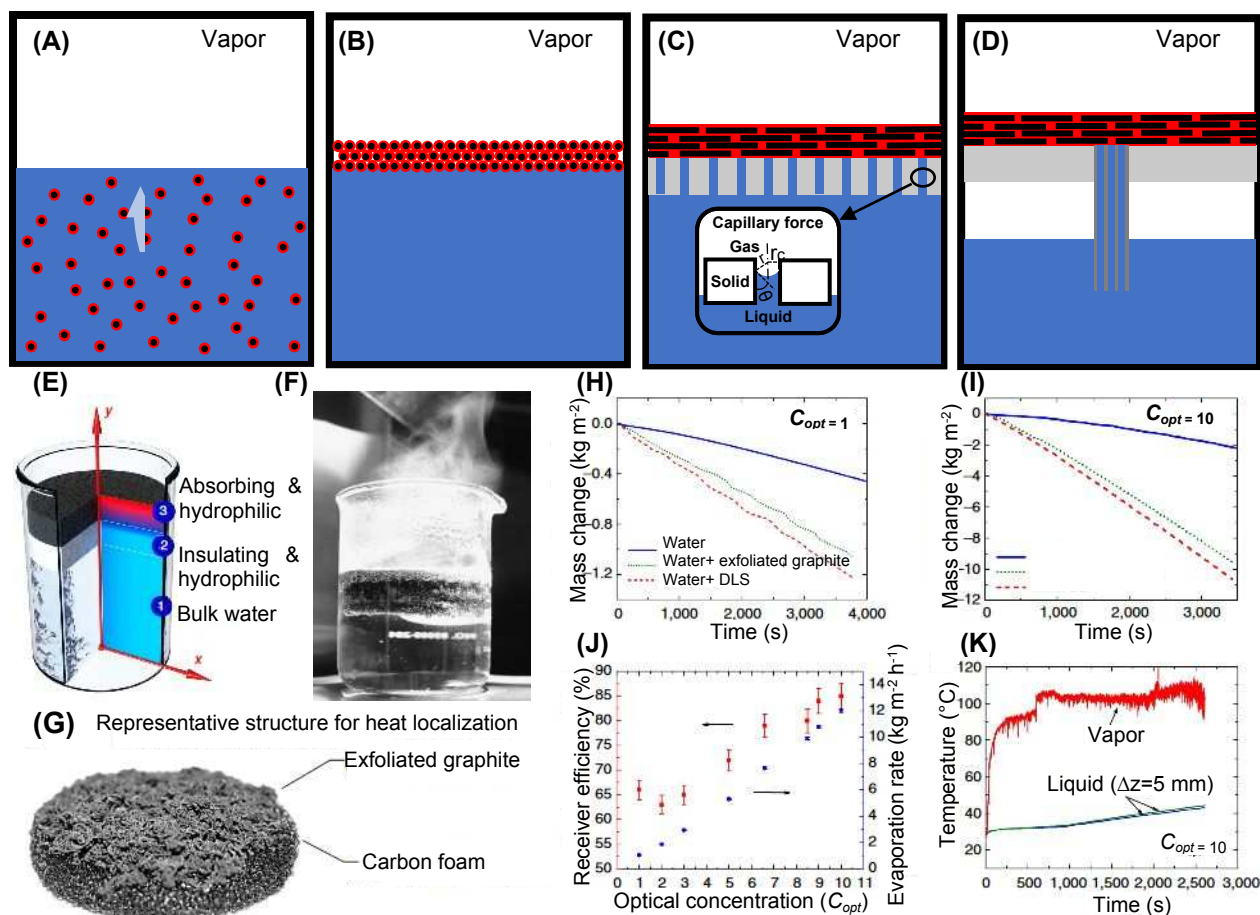
1092

1093

1094

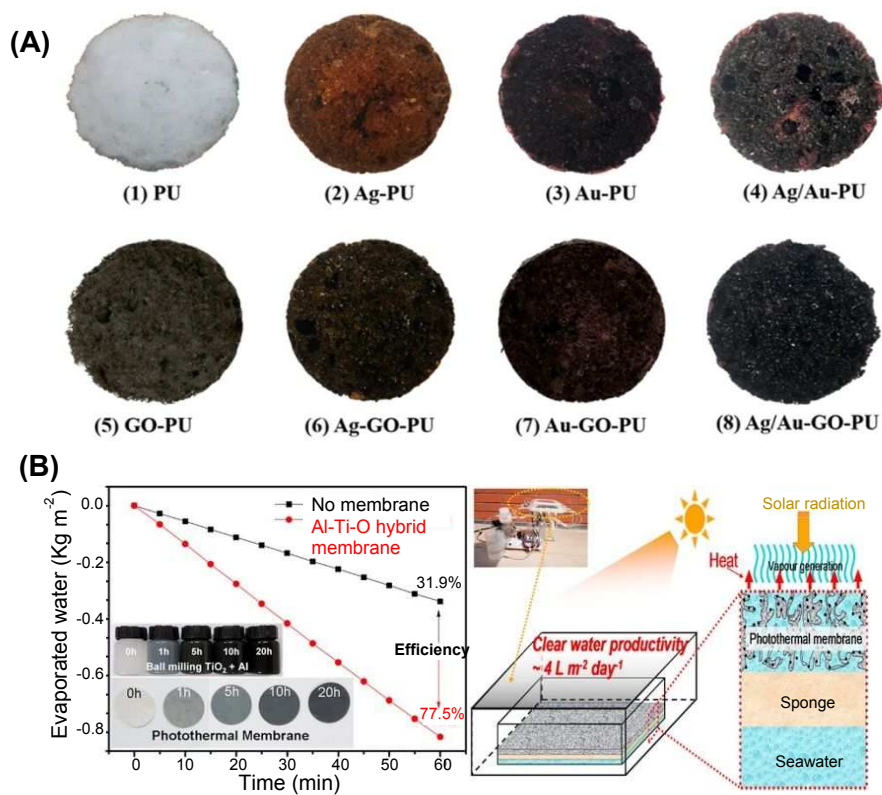
1095

1096



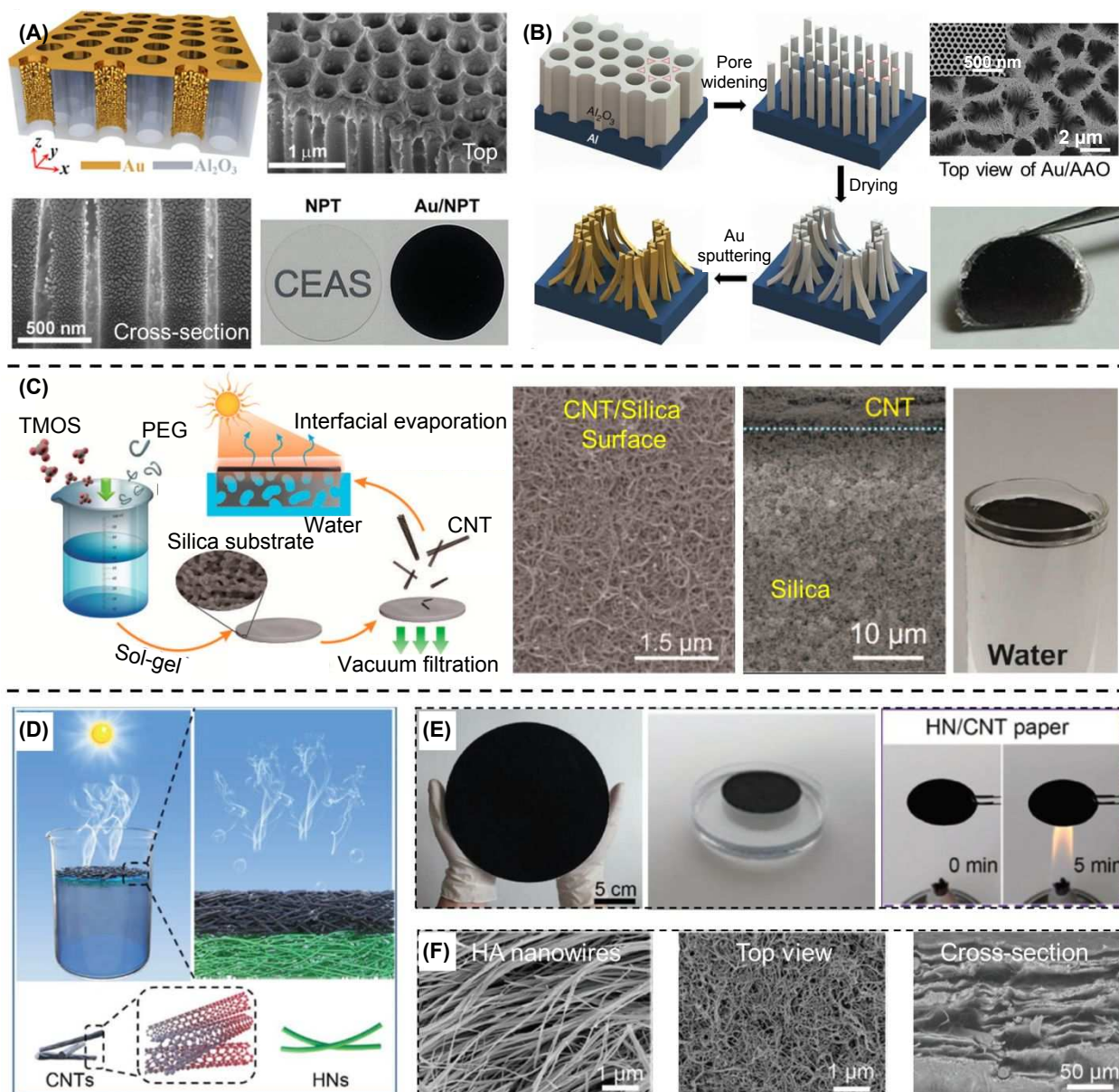
1097

1098 Figure 4. Schematic illustrations of (A) solar-driven evaporation system by bulk heating, (B) interfacial  
 1099 heating without heat insulating substrate, (C) interfacial heating with heat insulating substrate, and (D)  
 1100 interfacial heating with 1D water pathway. (E) Representative interfacial evaporator structure for localization  
 1101 of heat. (F) Photo of enhanced solar evaporation of the double-layer solar evaporator under 10 suns  
 1102 illumination. (G) Double-layer structure, consisting of carbon foam as a thermal insulating layer and  
 1103 exfoliated graphite as solar absorber. The evaporation mass losses of water with different structures under  
 1104 (H) 1 sun and (I) 10 suns irradiation. (J) The solar thermal efficiency of the evaporation process by the  
 1105 double-layer structure under different optical concentrations. (K) While the steam is generated, the  
 1106 underlying bulk liquid is at the ambient temperature. Reproduced with permission.<sup>21</sup> Copyright 2016  
 1107 Springer Nature Publishing AG.



1108

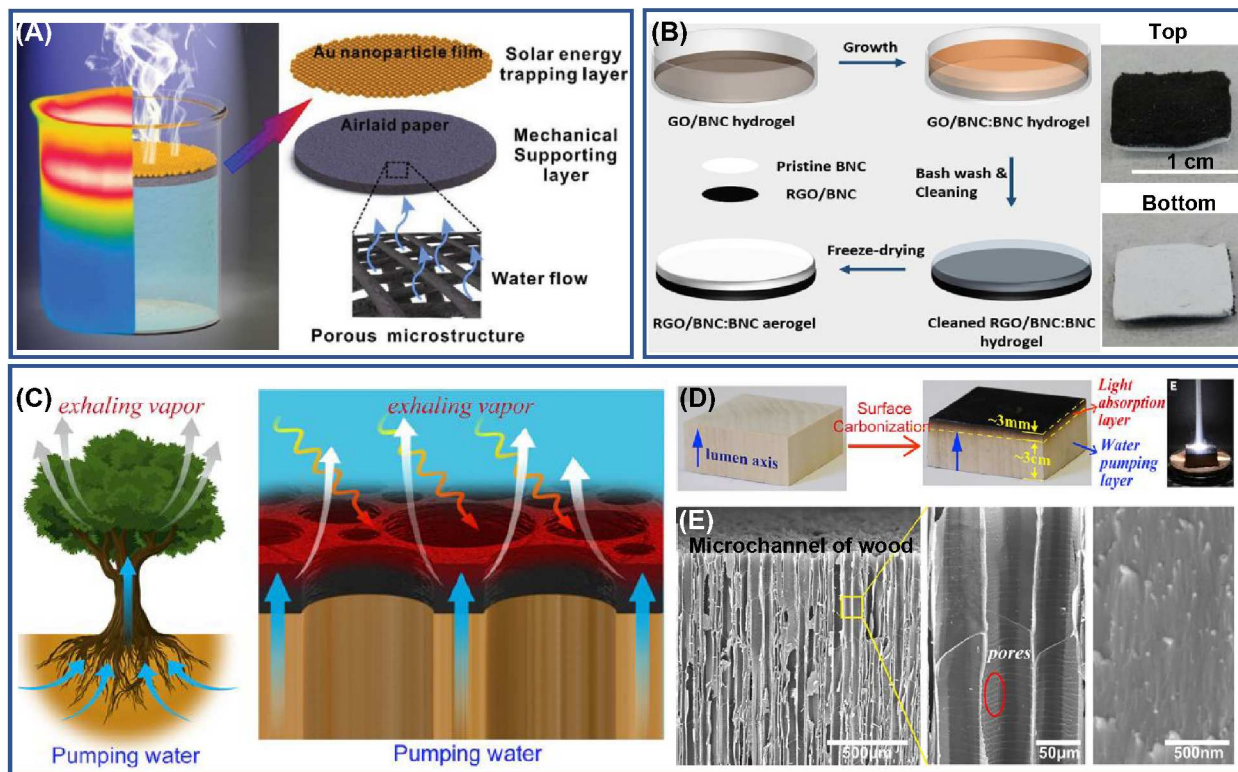
1109 **Figure 5.** Supporting layer based on synthetic polymers. (A) PU foam and PU foam-based solar  
 1110 evaporators. Reproduced with permission.<sup>111</sup> Copyright 2018 American Chemical Society. (B) Al-Ti-O-  
 1111 PVDF hybrid membrane as a solar evaporator. Reproduced with permission.<sup>114</sup> Copyright 2017 Elsevier.



1112

1113 **Figure 6.** Inorganic materials as supporting layers. (A) Self-assembled plasmonic absorber achieved by  
 1114 deposition of gold nanoparticles on AAO membrane. Reproduced with permission.<sup>49</sup> Copyright 2016  
 1115 American Association of Science. (B) Black gold/AAO membrane fabricated via pore-widening process  
 1116 and Au sputtering. Reproduced with permission.<sup>48</sup> Copyright 2015 Springer Nature Publishing AG. (C) Self-  
 1117 floating solar evaporators fabricated by coating CNTs on a microporous silica substrate. Reproduced with  
 1118 permission.<sup>100</sup> Copyright 2016 American Chemical Society. (D) Schematic illustration showing a bilayered  
 1119 solar evaporator based on hydroxyapatite nanowire paper and CNT. (E) Optical images showing the  
 1120 CNT/HNs (hydroxyapatite nanowires) paper and its fire resistance. (F) SEM images depicting the structures  
 1121 of HA nanowires and HNs paper. Reproduced with permission.<sup>118</sup> Copyright 2018 Wiley-VCH.

1122



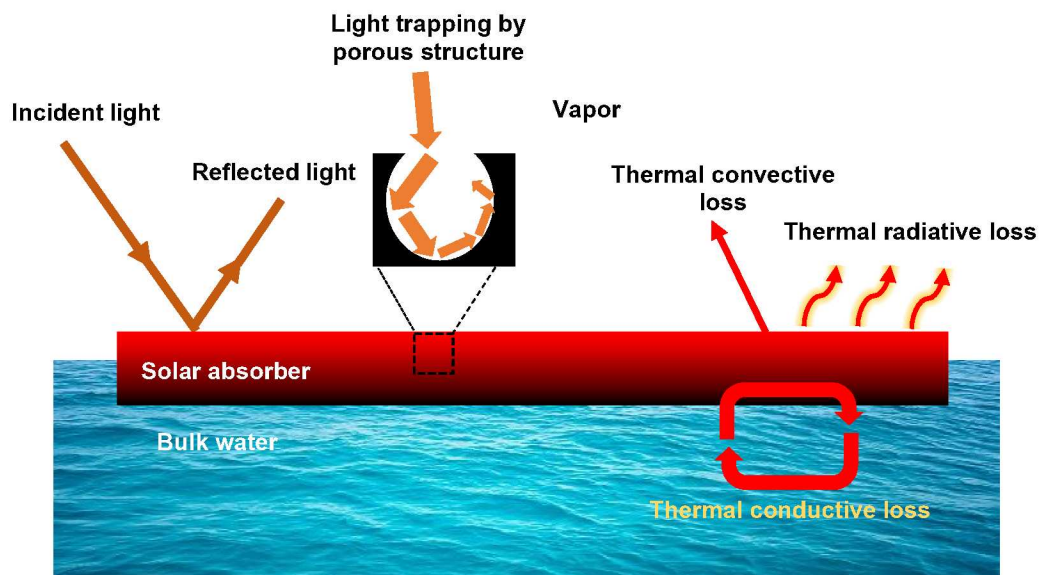
1123

1124 **Figure 7.** (A) AuNPs/air-laid paper bilayered solar evaporators. Reproduced with permission.<sup>34</sup> Copyright  
 1125 2018 Wiley-VCH. (B) Novel, scalable bilayered RGO/BNC:BNC aerogel as a solar evaporator, fabricated  
 1126 via in situ incorporation of RGO flakes into bacterial nanocellulose during its growth. Reproduced with  
 1127 permission.<sup>22</sup> Copyright 2018 Wiley-VCH. (C-E) Tree-inspired wood-based solar evaporators with unique  
 1128 microchannel network. Reproduced with permission.<sup>122</sup> Copyright 2017 Wiley-VCH. Reproduced with  
 1129 permission.<sup>125</sup> Copyright 2018 Cell Press.

1130

1131

1132



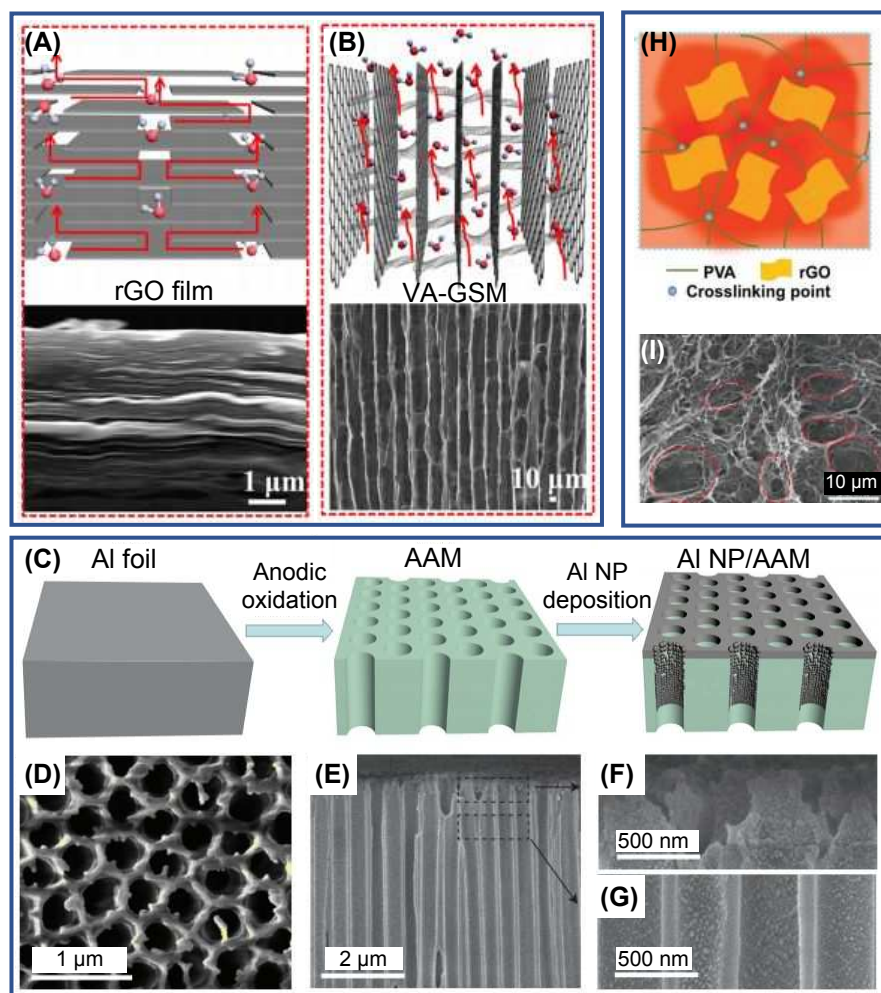
1133

1134 Figure 8. Schematic illustration depicting light's interaction with solar absorbers, and the corresponding  
1135 light-to-heat conversion and heat loss under solar illumination.

1136

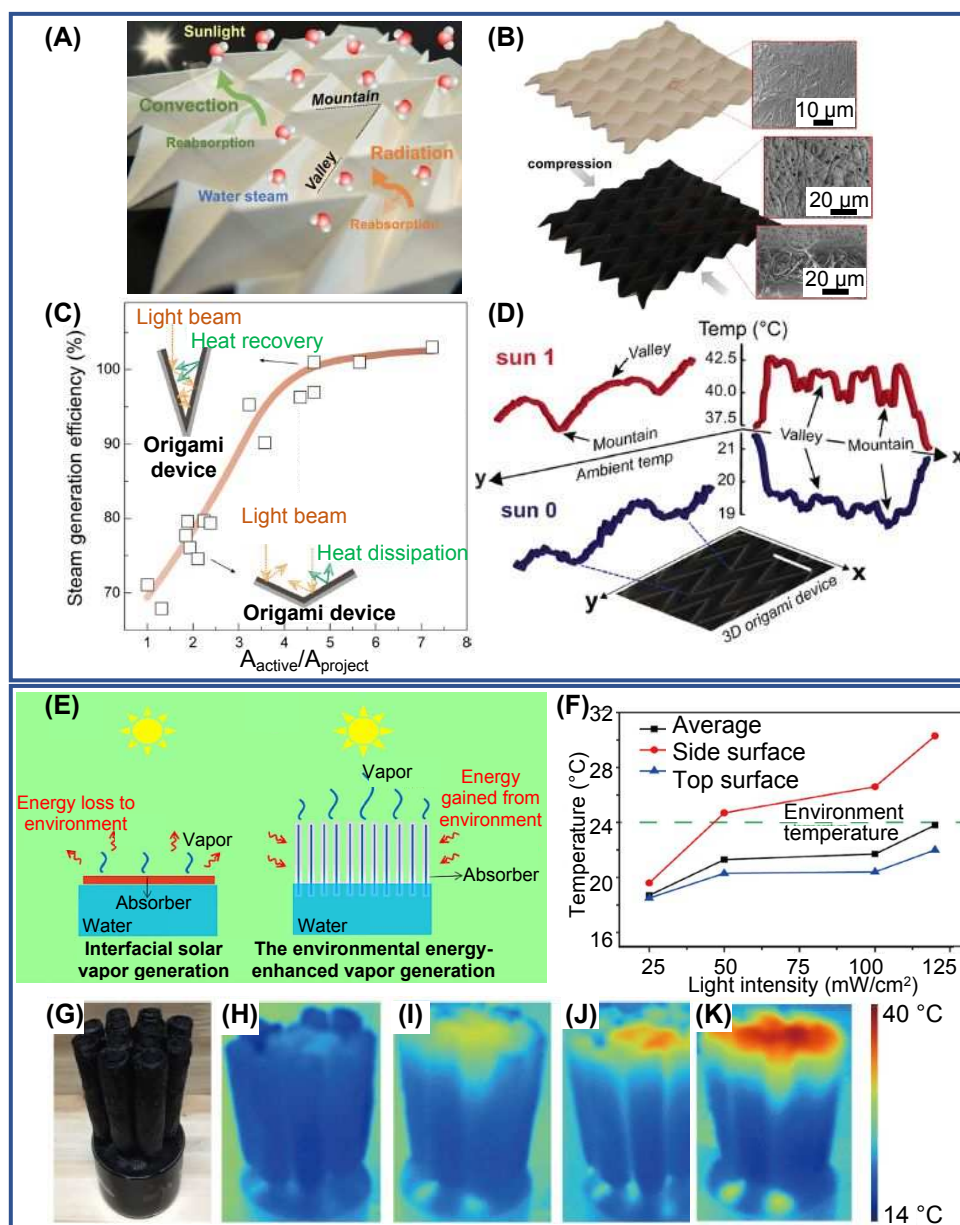
1137

1138



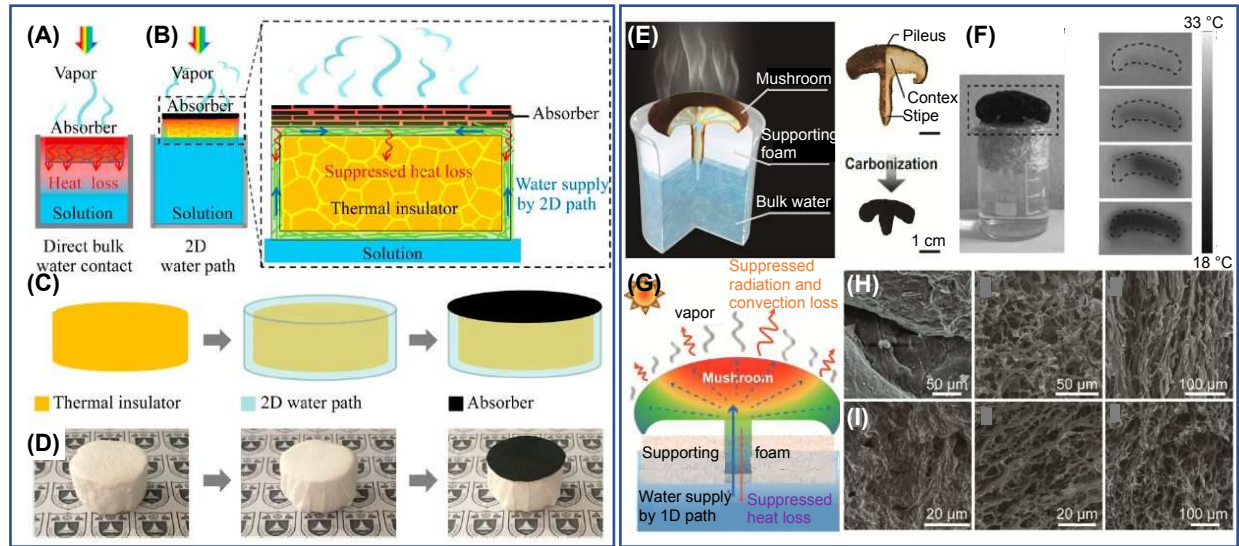
1139

1140 Figure 9. Schematic illustration and cross-section SEM images of the compact rGO film (A) and vertically  
 1141 aligned graphene sheets membrane (VA-GSM) (B) for solar steam generation. Reproduced with  
 1142 permission.<sup>77</sup> Copyright 2017 American Chemical Society. (C-F) Fabrication process and characterization  
 1143 of Al nanoparticles (NP)-based plasmonic solar evaporator. (C) Aluminum foils serve as the source material  
 1144 for the entire fabrication process, followed by anodic oxidation to fabricate aluminum oxide membrane (AAM)  
 1145 substrate. The Al NP/AAM structure formed after the NP deposition. High-resolution SEM images of the  
 1146 structure: Top view (D) and cross section (E). Magnified images of the cross-section areas indicated in (F)  
 1147 (G). Reproduced with permission.<sup>40</sup> Copyright 2016 Springer Nature Publishing AG. (H-I) The rGO/PVA  
 1148 aerogel. Schematic illustration showing rGO interpenetrating the PVA network (H) and cross-section SEM  
 1149 image of rGO/PVA aerogel (I). Reproduced with permission.<sup>69</sup> Copyright 2018 Royal Society of Chemistry.



1150

1151 Figure 10. (A-D) 3D origami solar steam generator. (A) Schematic illustration of Miura-ori tessellation  
 1152 structure for photothermal steam generation. (B) Optical images of the pristine cellulose membrane sheet  
 1153 and the composite-impregnated cellulose evaporator. The SEM images show the surface morphology of  
 1154 the pristine cellulose membrane and the composite-embedded cellulose sheets. (C) Steam generation  
 1155 efficiency under illumination as a function of areal density at a specific weight of 2.298–4.713  $\text{g}/\text{m}^2$ . (D)  
 1156 Spatial temperature distribution on the creased surface of the compressed 3D origami device, observed at  
 1157 the areal density of 2.5. The scale bar represents 1 cm. Reproduced with permission.<sup>121</sup> Copyright 2018  
 1158 American Chemical Society. (E-K) Schematic illustration and surface temperatures of the environmental  
 1159 energy-enhanced interfacial solar vapor generator. (E) Schematic illustrating the comparison between  
 1160 conventional interfacial solar vapor generation and environmental energy-enhanced interfacial solar vapor  
 1161 generation. (F) Temperatures of the top and side surfaces of the environmental energy-enhanced interfacial  
 1162 solar vapor generator under different light intensities. (G) Photograph of the environmental energy-  
 1163 enhanced interfacial solar vapor generator. (H–K) Infrared images of the environmental energy-enhanced  
 1164 interfacial solar vapor generator under (H) 25, (I) 50, (J) 100, and (K) 120  $\text{mW}/\text{cm}^2$  illumination, respectively.  
 1165 Reproduced with permission.<sup>102</sup> Copyright 2018 Cell Press.



1166

1167

1168

1169

1170

1171

1172

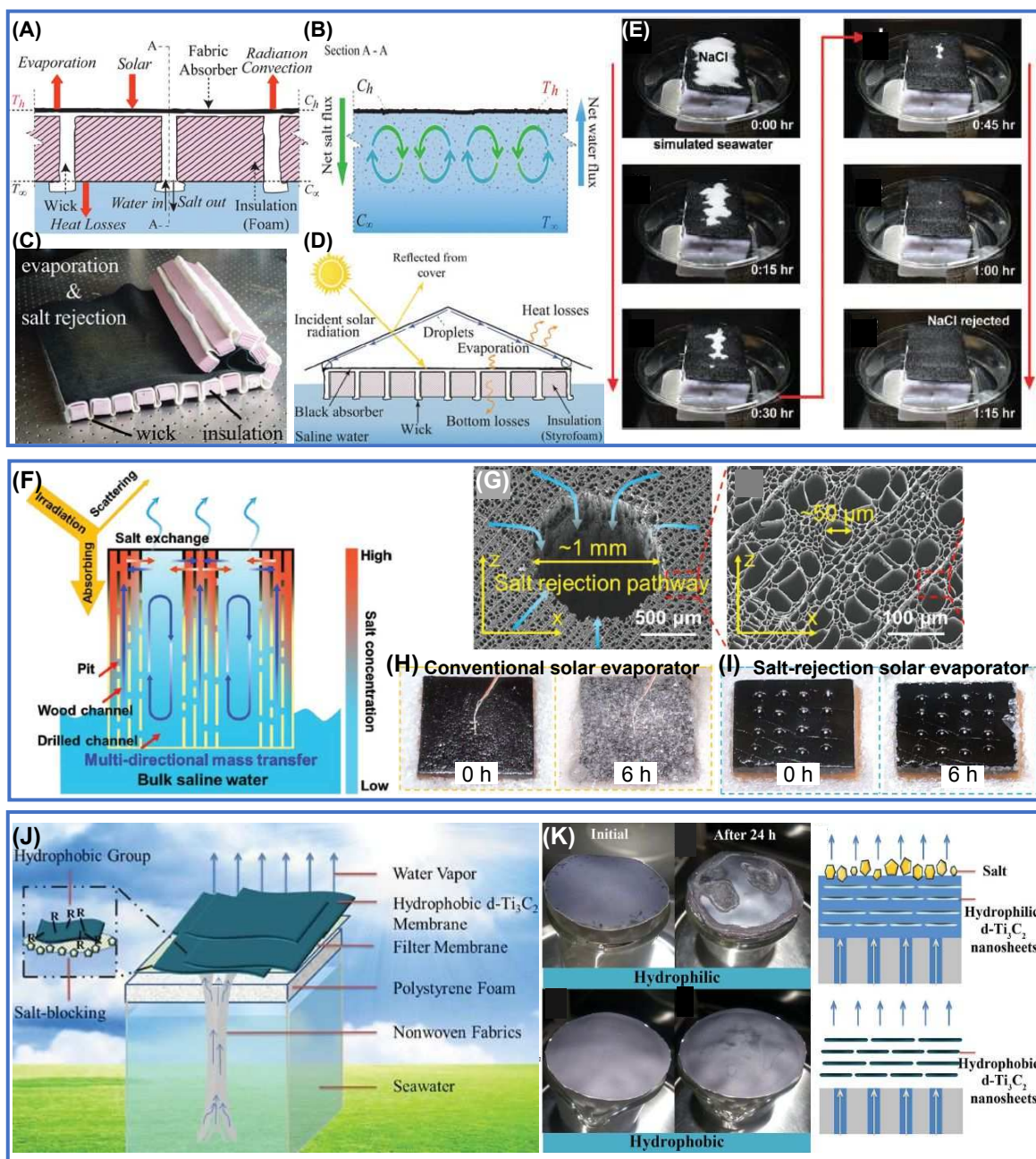
1173

1174

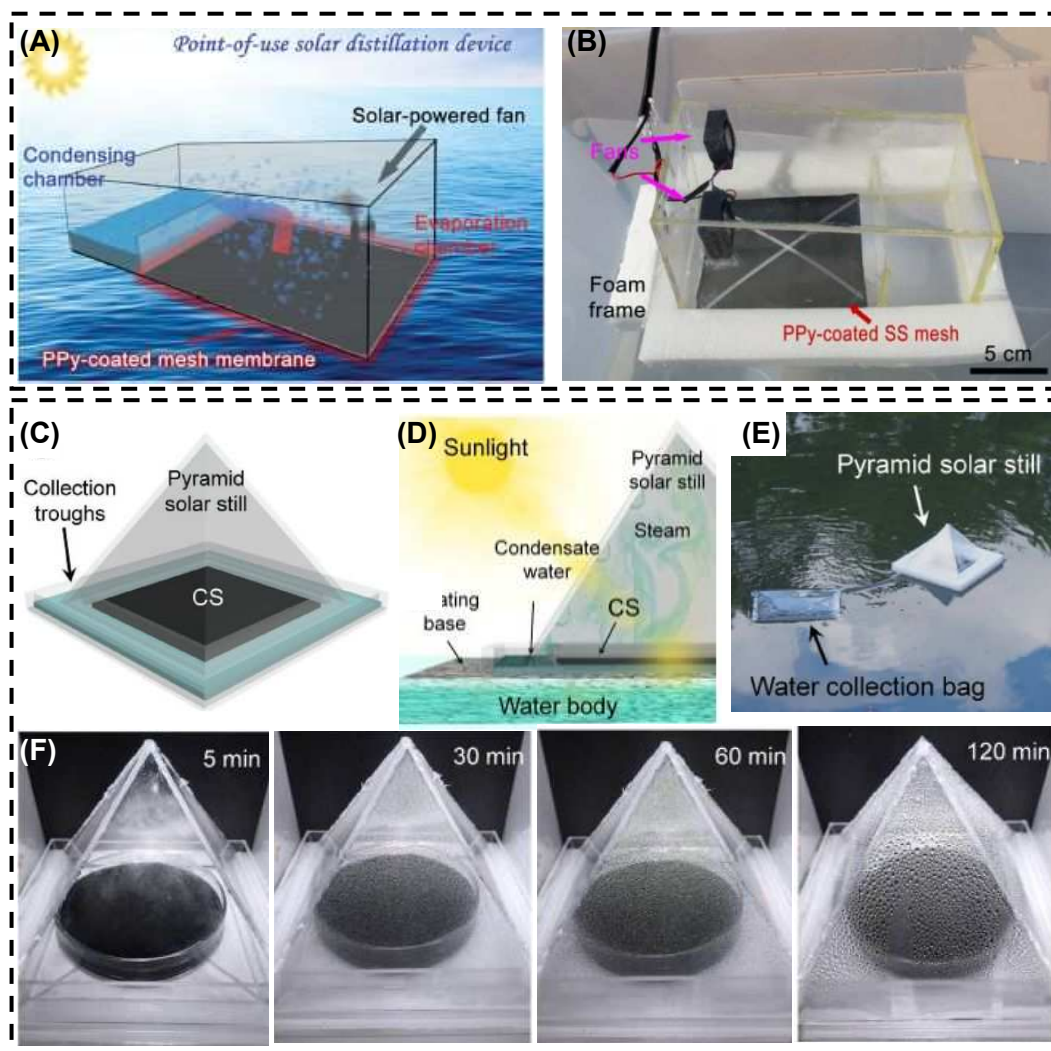
1175

1176

Figure 11. (A-D) Schematic illustration of solar evaporator with 2D water pathways. Schematic illustrations showing conventional solar steam generation with direct water contact (A) and suppressed heat loss with a 2D water supply (B). Fabrication steps (C) and corresponding photographs (D) of solar desalination devices: PS foam, cellulose paper wrapping, and GO film on top surface. Reproduced with permission.<sup>96</sup> Copyright 2016 National Academy of Sciences. (E-H) Mushroom-based solar steam generation with a 1D water pathway. (E) Schematic illustration and photographs of a mushroom-based solar steam-generation device. (F) The infrared photographs in order from top to bottom, correspond to  $t = 0, 60, 180,$  and  $360$  s after the dried carbonized mushroom touched the water. (G) Schematic illustration of solar evaporation in a mushroom-based structure. (H) SEM images of the pileus, context, and stipe of a mushroom before (H) and after (I) carbonization, respectively. Reproduced with permission.<sup>104</sup> Copyright 2017 Wiley-VCH.



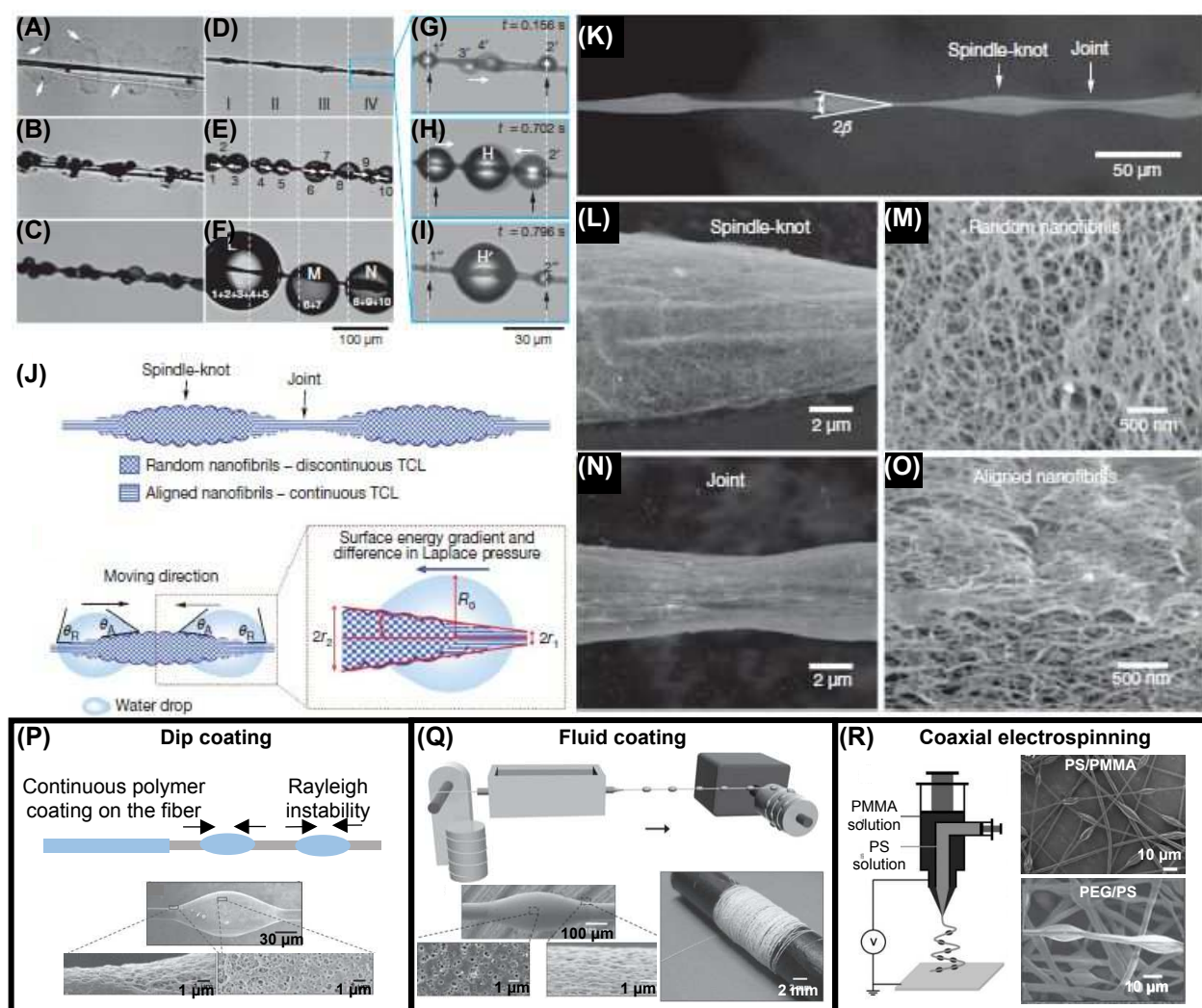
1177  
 1178 Figure 12. (A-D) Schematic illustrating structure of salt-rejecting solar evaporator with a black fabric solar  
 1179 absorber, a white fabric wicking water, and PS foam as an insulator. The white fabric delivers water and  
 1180 removes excess salt. (E) Photographs showing the progression of salt rejection from the evaporation  
 1181 structure placed in a reservoir of 3.5 wt% NaCl under 1 sun illumination. Reproduced with permission.<sup>130</sup>  
 1182 Copyright 2018 Royal Society of Chemistry. (F) Schematic illustration of multidirectional mass transfer in a  
 1183 wood-based solar evaporator. (G) SEM images of the drilled channels and microchannels on the wood-  
 1184 based evaporator. Photographs showing (H) salt blockage at the surface of the conventional solar  
 1185 evaporator, and (I) the salt-free surface of the self-regenerating evaporator after 6 hours continuous testing  
 1186 in 20 wt% NaCl solution with a solar irradiance of 1 sun. Reproduced with permission.<sup>134</sup> Copyright 2019  
 1187 Wiley-VCH. (J) Schematic illustration showing the hydrophobic d-Ti<sub>3</sub>C<sub>2</sub> (delaminated Ti<sub>3</sub>C<sub>2</sub>) membrane  
 1188 based solar desalination device. (K) Photographs and schematic illustration of the hydrophilic and  
 1189 hydrophobic d-Ti<sub>3</sub>C<sub>2</sub> membranes before and after 24 hours solar desalination. Reproduced with  
 1190 permission.<sup>135</sup> Copyright 2018 Royal Society of Chemistry.



1191  
 1192 Figure 13. Schematic illustration (A) and photographs (B) of a floating solar distillation device with PPy-  
 1193 coated stainless steel (SS) mesh membrane and plastic cover. Reproduced with permission.<sup>83</sup> Copyright  
 1194 2015 Wiley-VCH. Schematic illustration depicting the structure of a pyramid solar still (C) and water  
 1195 collection under sunlight (D). Photographs of a pyramid solar still floating on water (E) and condensed vapor  
 1196 on the roof of the pyramid at different evaporation times (F). Reproduced with permission.<sup>139</sup> Copyright  
 1197 2018 Wiley-VCH.

1198  
 1199  
 1200  
 1201  
 1202  
 1203  
 1204

1205



1206

1207 Figure 14. (A-O) Directional water collection by spider silk fiber. (A-H) In situ optical microscopic  
 1208 observations of directional water collection on spider silk fiber in mist. (K-O) Structure of wet-rebuilt spider  
 1209 silk. (K) Environmental SEM images of periodic spindle-knots linked with slender joints. Low-magnification  
 1210 (L) and zoomed images (M) show that a spindle-knot is randomly interwoven with nanofibrils. Low-  
 1211 magnification (N) and high-magnification images (O) of the joint, which is composed of nanofibrils  
 1212 aligned relatively parallel to the silk axis. (J) Mechanism of directional water collection on wet-rebuilt spider silk by  
 1213 wettability and Laplace pressure difference. Reproduced with permission.<sup>155</sup> Copyright 2010 Springer  
 1214 Nature Publishing AG. Artificial spider silk fiber with periodic spindle-knot structure, fabricated by dip coating  
 1215 (P), fluid coating (Q) and coaxial-electrospinning method (R). Reproduced with permission.<sup>157-159</sup> Copyright  
 1216 2011 Wiley-VCH. Copyright 2012 Wiley-VCH. Copyright 2011 Wiley-VCH.

1217

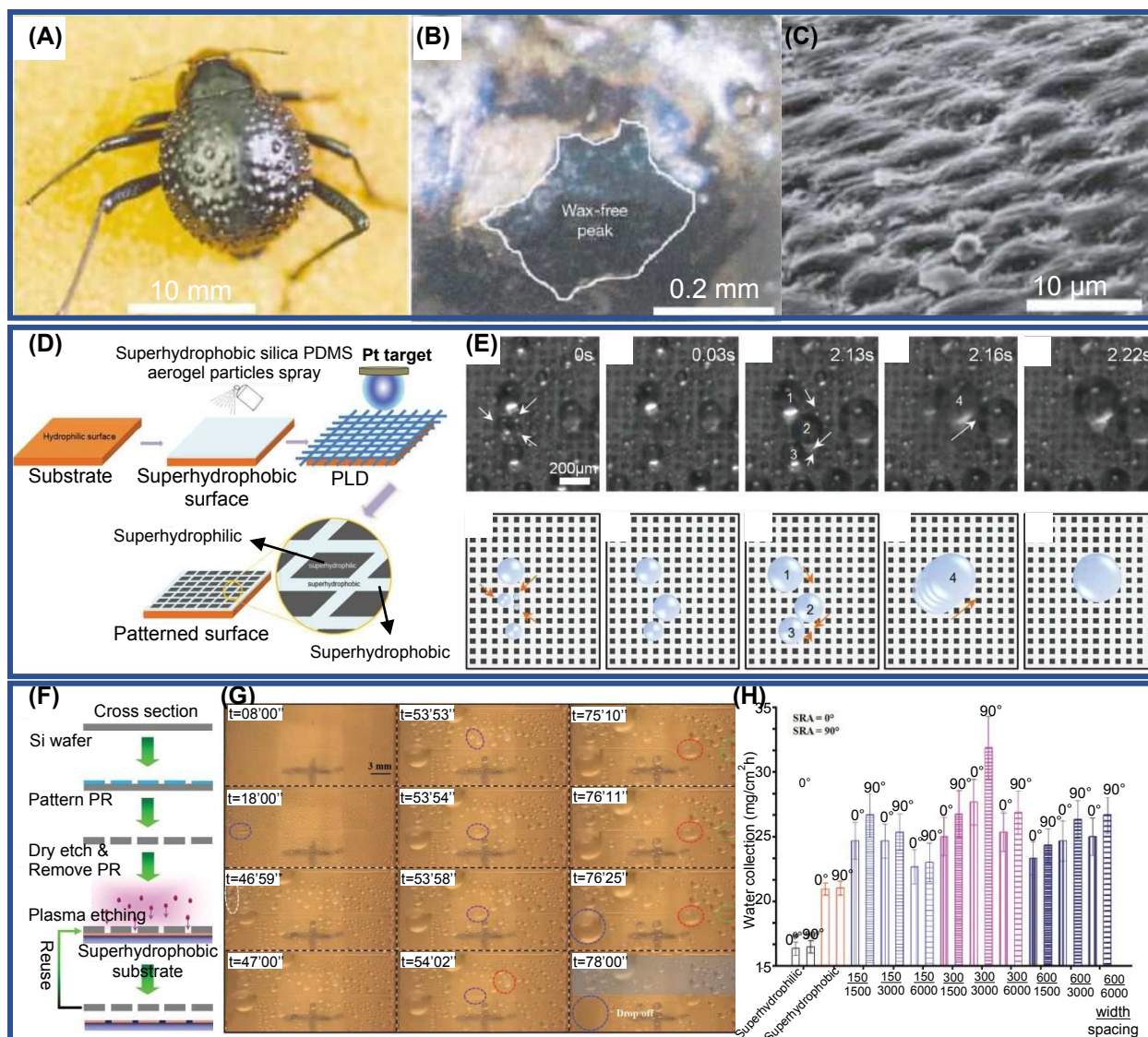
1218

1219

1220

1221

1222



1223

1224 Figure 15. (A-C) Water-capturing surface of the fused overwings (elytra) of the desert beetle *Stenocara sp.*

1225 (A) Adult female desert beetle. Peaks and troughs are evident on the surface of the elytra in a dorsal view.

1226 (B) A 'bump' on the elytra, stained with Red O for 15 min and then with 60% isopropanol for 10 min, a

1227 procedure that tests for waxes. Depressed areas of the otherwise black elytra are stained positively (waxy,

1228 colored), whereas the peaks of the bumps remain unstained (wax-free; black). (C) SEM of the textured

1229 surface of the depressed areas. Reproduced with permission.<sup>160</sup> Copyright 2001 Springer Nature Publishing

1230 AG. (D-E) Desert beetle-inspired hybrid micro-square patterned surface for water collection. (D) Schematic

1231 illustration of the construction of the *Stenocara* beetle-inspired functional surface with a

1232 superhydrophilic/superhydrophobic pattern. (E) In situ and direct observation of water vapor condensation,

1233 water droplet growth, and the rolling of water droplets on the sample. Reproduced with permission.<sup>166</sup>

1234 Copyright 2017 Wiley-VCH. (F-H) Beetle-inspired hybrid micro-strip patterned surface for water collection.

1235 (F) A process flow diagram illustrating the fabrication procedure of the Si-stencil and hybrid

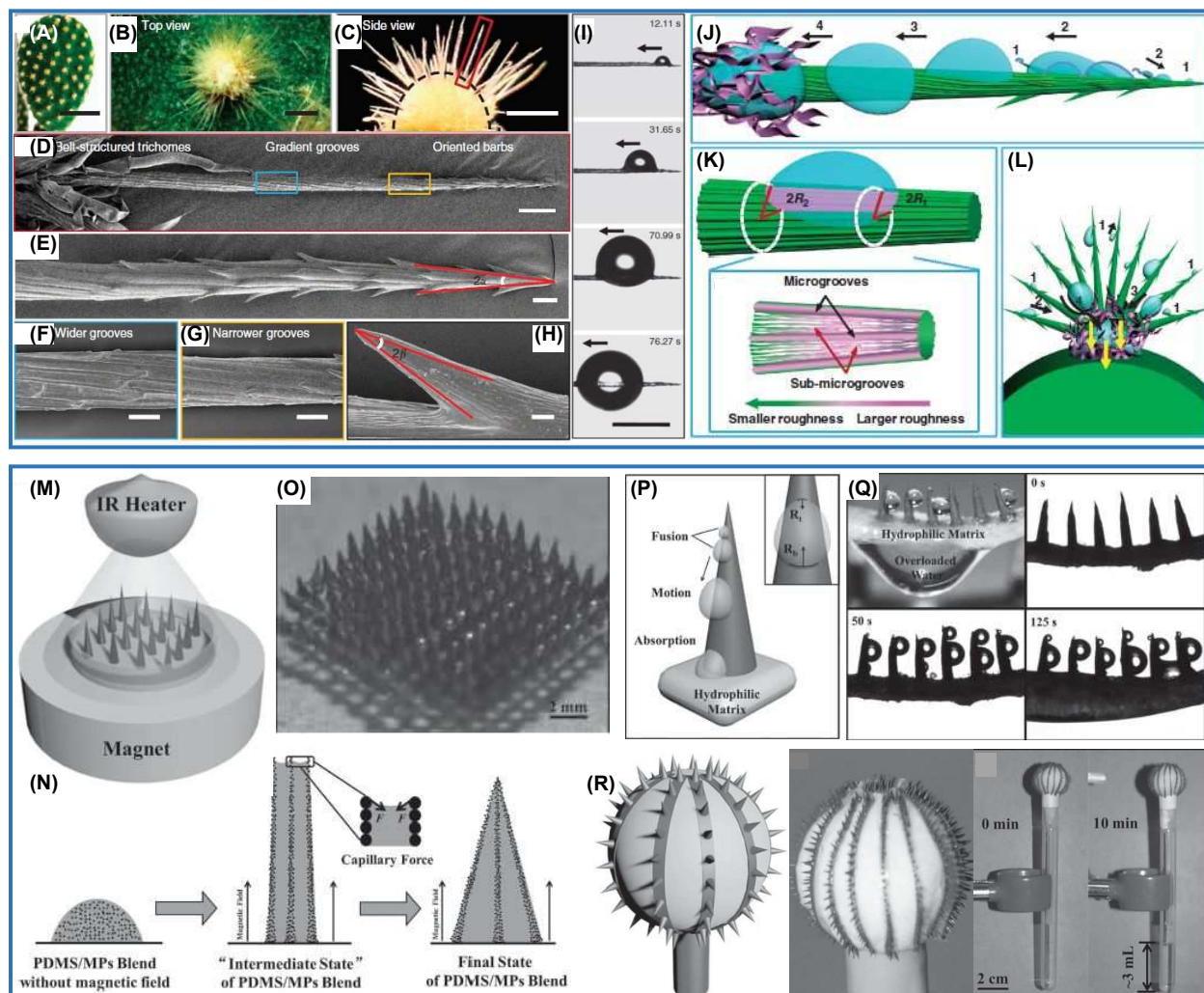
1236 superhydrophobic substrate. (G) In situ observation by optical microscopy of fog collection on hybrid and

1237 anisotropic surfaces with 300 width and 6000 μm spacing. (H) Water collection efficiency of 11 different

1238 surfaces with SRA = 0° and 90°. The anisotropic substrate has a track width = 150, 300, and 600 μm, with

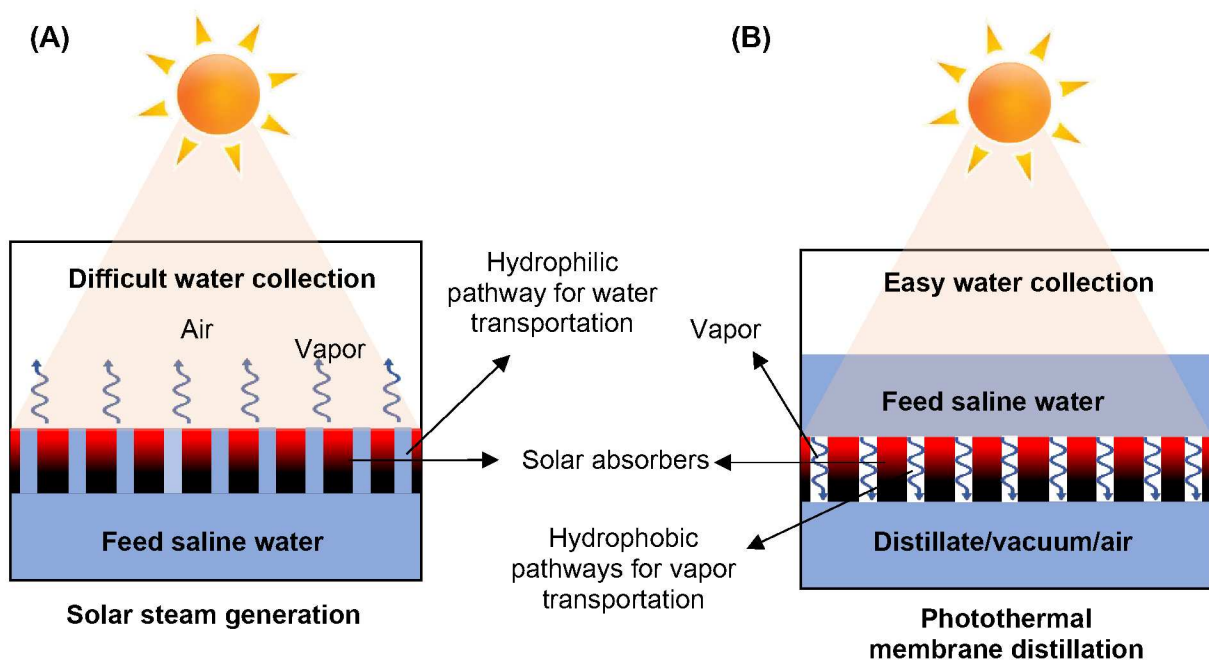
1239 three different track distances (1500, 3000, and 6000 μm). Reproduced with permission.<sup>167</sup> Copyright 2017

1240 Wiley-VCH.



1241

1242 Figure 16. (A-L) Water collection by cacti. (A-H) Optical images and SEM images of the structure the cacti.  
 1243 Scale bars, 5 cm (A), 500  $\mu\text{m}$  (B, C), 100  $\mu\text{m}$  (D), 20  $\mu\text{m}$  (E–G), and 2  $\mu\text{m}$  (H). (I) In situ optical microscopic  
 1244 observations of directional water collection on cactus spine. (J-L) The mechanism of efficient fog collection  
 1245 on the cacti. Reproduced with permission.<sup>168</sup> Copyright 2012 Springer Nature Publishing AG. (M-R) Cacti-  
 1246 inspired microtip pattern for water collection. (M) Schematic representation of the proposed magnetic  
 1247 particle-assisted molding for the fabrication of cacti spine-like conical micro-tip arrays. (N) Diagram of the  
 1248 micro-tip formation mechanism. (O) Photograph of a square array of micro-tips grown on a geometric  
 1249 patterned PS substrate. (P) Illustration of the “fusion” and “motion” process, and the difference of the inner  
 1250 radius of a water droplet placed on a conical tip. (Q) Behavior of fog collection by the microtip pattern. (R)  
 1251 Illustration of the cactus-inspired device and photographs of the cactus-inspired continuous fog collector for  
 1252 water collection. Reproduced with permission.<sup>171</sup> Copyright 2014 Wiley-VCH.



1253

1254 Figure 17. Similarities and differences between solar steam generation and photothermal membrane  
 1255 distillation.

1256

1257

1258

1259

1260

1261

1262

1263

1264

1265

1266

1267

1268

1269

1270

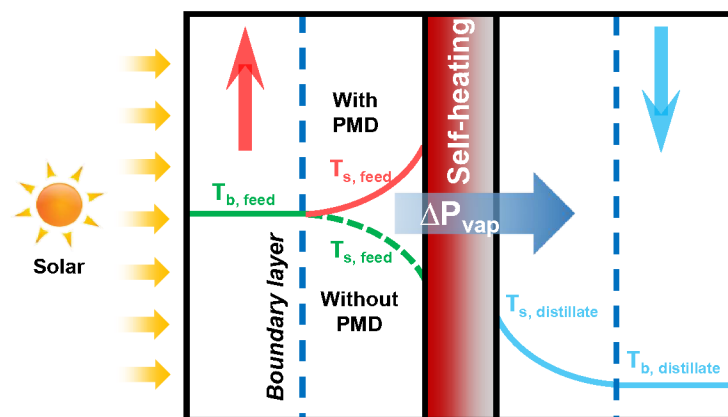
1271

1272

1273

1274

1275



1276

1277 **Figure 18.** Schematic illustration showing the mechanism of photothermal membrane distillation (PMD)

1278 and its effect on temperature polarization of conventional MD.

1279

1280

1281

1282

1283

1284

1285

1286

1287

1288

1289

1290

1291

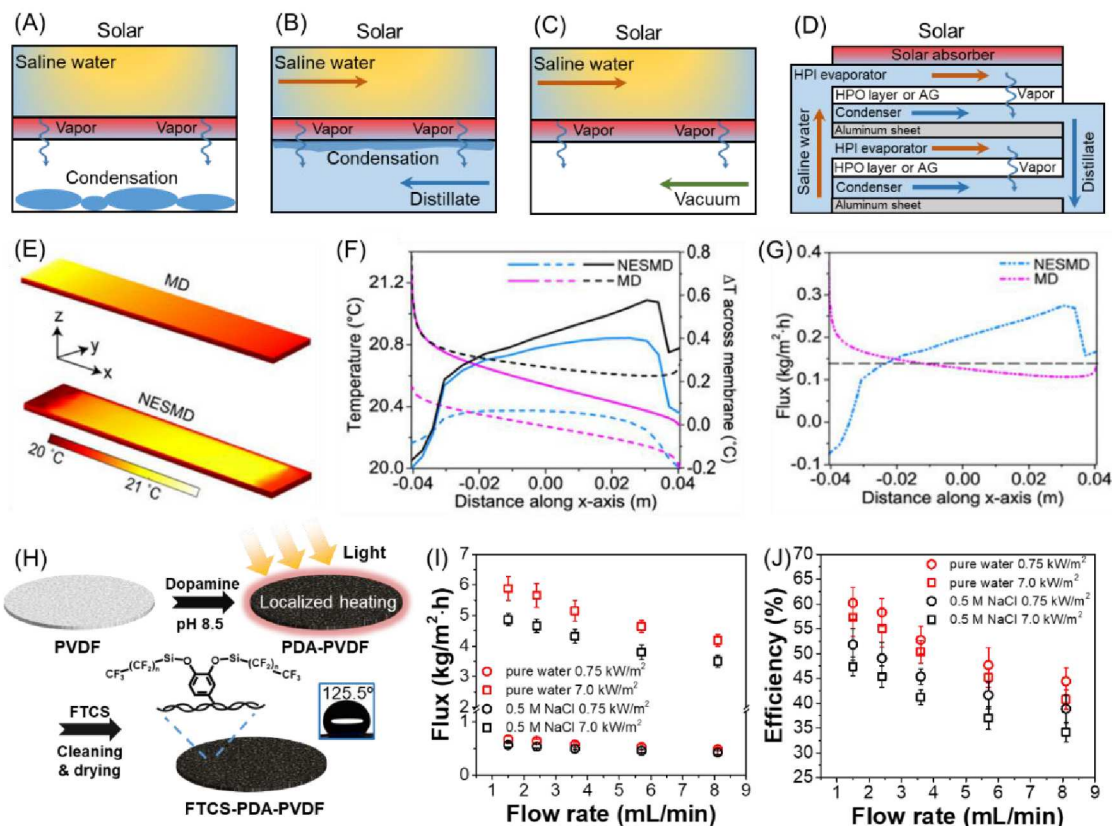
1292

1293

1294

1295

1296



1297

1298 **Figure 19.** Representative PMD modules: (A) passive MD without pumping systems, (B) PMD in direct  
 1299 contact membrane distillation configuration (DCMD), (C) PMD in vacuum membrane distillation  
 1300 configuration (VMD), (D) PMD with multiple latent heat recovery layers. (E) Calculated temperature  
 1301 distributions at the membrane surface for MD (top) and nanophotonics-enabled solar membrane distillation  
 1302 (NESMD) (bottom). (F) Theoretical membrane temperature at the feed (solid) and distillate (dotted) sides  
 1303 for NESMD (blue) and MD (magenta), and theoretical  $\Delta T$  across the membrane (right axis, black) for  
 1304 NESMD (solid) and MD (dotted). (G) Calculated flux for NESMD at 0.7 kW/m<sup>2</sup> solar illumination (dot-dashed  
 1305 blue) and MD (dotted magenta). Dashed gray line: average flux. Reproduced with permission.<sup>177</sup>  
 1306 Copyright 2017 National Academy of Sciences. (H) Synthesis of the FTCS–PDA–PVDF membrane. Water  
 1307 flux (I) and efficiency (J) of the solar-driven DCMD system using the FTCS–PDA–PVDF membrane with  
 1308 varying feed flow rates, using both pure water and 0.5 M NaCl saline water. Reproduced with permission.<sup>108</sup>  
 1309 Copyright 2018 Royal Society of Chemistry.

1310

1311

1312

1313

1314

1315

1316

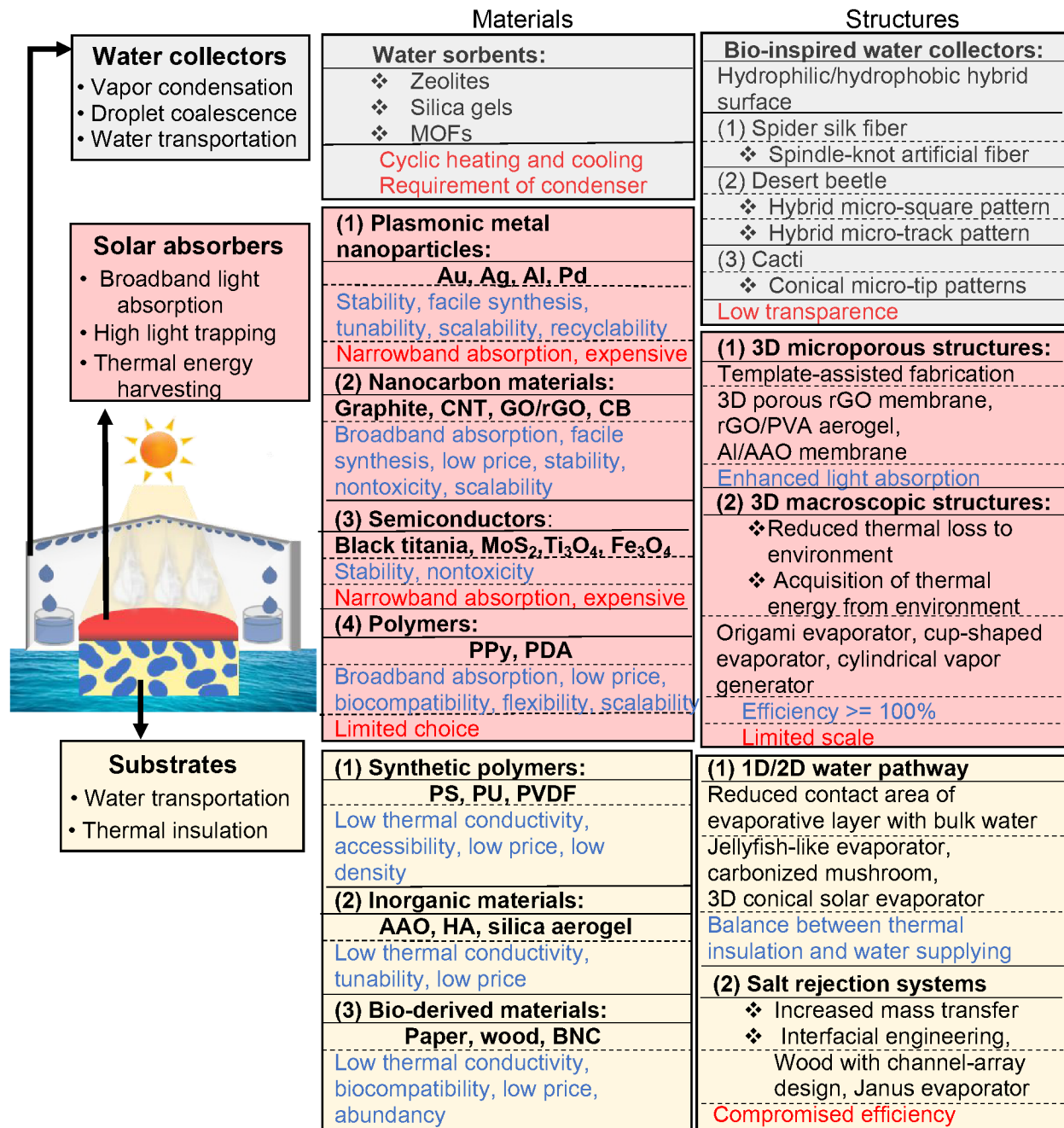
1317

1318

1319

1320

1321



1322

1323 **Figure 20.** Summary of materials choice and structural designs for three key components for solar  
 1324 evaporators, based on the design principles discussed in this review.

1325

1326

1327

**1328 Acknowledgement**

1329 We acknowledge support from the National Science Foundation Environmental Engineering  
1330 Program (CBET1604542). The authors thank Professor James C. Ballard for careful review of the  
1331 manuscript.

1332 **References**

- 1333 1. L. M. Fry, J. R. Mihelcic and D. W. Watkins, *Environmental Science & Technology*, 2008,  
1334 **42**, 4298-4304.
- 1335 2. S. Sindhu, V. Nehra and S. Luthra, *Renewable and Sustainable Energy Reviews*, 2017,  
1336 **73**, 496-511.
- 1337 3. T. Oki and S. Kanae, *science*, 2006, **313**, 1068-1072.
- 1338 4. WATER SCARCITY, <https://www.worldwildlife.org/threats/water-scarcity>.
- 1339 5. *World Water*, 2019.
- 1340 6. *IDA Desalination Yearbook 2018–2019*, Media Analytics Ltd.: Oxford, UK, 2019.
- 1341 7. A. E. Childress and M. Elimelech, *Journal of membrane science*, 1996, **119**, 253-268.
- 1342 8. C. Fritzmann, J. Löwenberg, T. Wintgens and T. Melin, *Desalination*, 2007, **216**, 1-76.
- 1343 9. L. F. Greenlee, D. F. Lawler, B. D. Freeman, B. Marrot and P. Moulin, *Water research*,  
1344 2009, **43**, 2317-2348.
- 1345 10. L. Tian, J. Luan, K.-K. Liu, Q. Jiang, S. Tadeballi, M. K. Gupta, R. R. Naik and S.  
1346 Singamaneni, *Nano letters*, 2015, **16**, 609-616.
- 1347 11. J. Ortiz, J. Sotoca, E. Exposito, F. Gallud, V. Garcia-Garcia, V. Montiel and A. Aldaz,  
1348 *Journal of Membrane Science*, 2005, **252**, 65-75.
- 1349 12. M. Sadrzadeh and T. Mohammadi, *Desalination*, 2008, **221**, 440-447.
- 1350 13. G. Liu, J. Shen, Q. Liu, G. Liu, J. Xiong, J. Yang and W. Jin, *Journal of membrane science*,  
1351 2018, **548**, 548-558.
- 1352 14. A. D. Khawaji, I. K. Kutubkhanah and J.-M. Wie, *Desalination*, 2008, **221**, 47-69.
- 1353 15. D. Zhao, J. Xue, S. Li, H. Sun and Q.-d. Zhang, *Desalination*, 2011, **273**, 292-298.
- 1354 16. E. Delyannis, *Solar energy*, 2003, **75**, 357-366.
- 1355 17. O. Neumann, A. S. Urban, J. Day, S. Lal, P. Nordlander and N. J. Halas, *ACS nano*, 2012,  
1356 **7**, 42-49.
- 1357 18. A. Kabeel and S. El-Agouz, *Desalination*, 2011, **276**, 1-12.
- 1358 19. D. Zhao, H. Duan, S. Yu, Y. Zhang, J. He, X. Quan, P. Tao, W. Shang, J. Wu and C. Song,  
1359 *Scientific reports*, 2015, **5**, 17276.
- 1360 20. P. Zhang, Q. Liao, H. Yao, Y. Huang, H. Cheng and L. Qu, *Energy Storage Materials*,  
1361 2018.
- 1362 21. H. Ghasemi, G. Ni, A. M. Marconnet, J. Loomis, S. Yerci, N. Miljkovic and G. Chen, *Nature*  
1363 *communications*, 2014, **5**, 4449.
- 1364 22. Q. Jiang, L. Tian, K. K. Liu, S. Tadeballi, R. Raliya, P. Biswas, R. R. Naik and S.  
1365 Singamaneni, *Advanced materials*, 2016, **28**, 9400-9407.
- 1366 23. P. Tao, G. Ni, C. Song, W. Shang, J. Wu, J. Zhu, G. Chen and T. Deng, *Nature Energy*,  
1367 2018, **1**.
- 1368 24. A. Raza, J.-Y. Lu, S. Alzaim, H. Li and T. Zhang, *Energies*, 2018, **11**, 253.
- 1369 25. J. U. Kim, S. Lee, S. J. Kang and T.-i. Kim, *Nanoscale*, 2018, **10**, 21555-21574.
- 1370 26. G. Liu, J. Xu and K. Wang, *Nano Energy*, 2017, **41**, 269-284.
- 1371 27. A. O. Govorov and H. H. Richardson, *Nano today*, 2007, **2**, 30-38.
- 1372 28. A. Stepanovich.
- 1373 29. C. A. Gueymard, *Solar energy*, 2004, **76**, 423-453.
- 1374 30. P. Wang, *Environmental Science: Nano*, 2018, **5**, 1078-1089.
- 1375 31. S. Tadeballi, J. Yim, S. Cao, Z. Wang, R. R. Naik and S. Singamaneni, *Small*, 2018, **14**,  
1376 1702382.
- 1377 32. P. K. Jain, X. Huang, I. H. El-Sayed and M. A. El-Sayed, *Accounts of chemical research*,  
1378 2008, **41**, 1578-1586.
- 1379 33. Q. Jiang, Y. J. Chandar, S. Cao, E. D. Kharasch, S. Singamaneni and J. J. Morrissey,  
1380 *Advanced Biosystems*, 2017, **1**, 1700096.

- 1381 34. Y. Liu, S. Yu, R. Feng, A. Bernard, Y. Liu, Y. Zhang, H. Duan, W. Shang, P. Tao and C.  
1382 Song, *Advanced Materials*, 2015, **27**, 2768-2774.
- 1383 35. X. Wang, Y. He, X. Liu, G. Cheng and J. Zhu, *Applied energy*, 2017, **195**, 414-425.
- 1384 36. A. Politano, P. Argurio, G. Di Profio, V. Sanna, A. Cupolillo, S. Chakraborty, H. A. Arafat  
1385 and E. Curcio, *Advanced Materials*, 2017, **29**, 1603504.
- 1386 37. M. Shang, N. Li, S. Zhang, T. Zhao, C. Zhang, C. Liu, H. Li and Z. Wang, *ACS Applied*  
1387 *Energy Materials*, 2017, **1**, 56-61.
- 1388 38. Y. Lin, Z. Chen, L. Fang, M. Meng, Z. Liu, Y. Di, W. Cai, S. Huang and Z. Gan,  
1389 *Nanotechnology*, 2018, **30**, 015402.
- 1390 39. P. Fan, H. Wu, M. Zhong, H. Zhang, B. Bai and G. Jin, *Nanoscale*, 2016, **8**, 14617-14624.
- 1391 40. L. Zhou, Y. Tan, J. Wang, W. Xu, Y. Yuan, W. Cai, S. Zhu and J. Zhu, *Nature Photonics*,  
1392 2016, **10**, 393.
- 1393 41. M. Zhu, Y. Li, F. Chen, X. Zhu, J. Dai, Y. Li, Z. Yang, X. Yan, J. Song and Y. Wang,  
1394 *Advanced Energy Materials*, 2018, **8**, 1701028.
- 1395 42. Z. Fang, Y.-R. Zhen, O. Neumann, A. Polman, F. J. García de Abajo, P. Nordlander and  
1396 N. J. Halas, *Nano letters*, 2013, **13**, 1736-1742.
- 1397 43. Z. Wang, Y. Liu, P. Tao, Q. Shen, N. Yi, F. Zhang, Q. Liu, C. Song, D. Zhang and W.  
1398 Shang, *Small*, 2014, **10**, 3234-3239.
- 1399 44. L. Tian, E. Chen, N. Gandra, A. Abbas and S. Singamaneni, *Langmuir*, 2012, **28**, 17435-  
1400 17442.
- 1401 45. S. Tadepalli, Z. Wang, J. Slocik, R. R. Naik and S. Singamaneni, *Nanoscale*, 2017, **9**,  
1402 15666-15672.
- 1403 46. L. Tian, K.-K. Liu, M. Fei, S. Tadepalli, S. Cao, J. A. Geldmeier, V. V. Tsukruk and S.  
1404 Singamaneni, *ACS applied materials & interfaces*, 2016, **8**, 4031-4041.
- 1405 47. J. Luan, J. J. Morrissey, Z. Wang, H. G. Derami, K.-K. Liu, S. Cao, Q. Jiang, C. Wang, E.  
1406 D. Kharasch and R. R. Naik, *Light: Science & Applications*, 2018, **7**, 29.
- 1407 48. K. Bae, G. Kang, S. K. Cho, W. Park, K. Kim and W. J. Padilla, *Nature communications*,  
1408 2015, **6**, 10103.
- 1409 49. L. Zhou, Y. Tan, D. Ji, B. Zhu, P. Zhang, J. Xu, Q. Gan, Z. Yu and J. Zhu, *Science*  
1410 *Advances*, 2016, **2**, e1501227.
- 1411 50. C. Liu, J. Huang, C. E. Hsiung, Y. Tian, J. Wang, Y. Han and A. Fratilocchi, *Advanced*  
1412 *Sustainable Systems*, 2017, **1**, 1600013.
- 1413 51. L. Zhu, M. Gao, C. K. N. Peh and G. W. Ho, *Materials Horizons*, 2018, **5**, 323-343.
- 1414 52. X. Liu, H. Cheng, Z. Guo, Q. Zhan, J. Qian and X. Wang, *ACS applied materials &*  
1415 *interfaces*, 2018, **10**, 39661-39669.
- 1416 53. X. Liu, B. Hou, G. Wang, Z. Cui, X. Zhu and X. Wang, *Journal of Materials Research*,  
1417 2018, **33**, 674-684.
- 1418 54. G. Zhu, J. Xu, W. Zhao and F. Huang, *ACS applied materials & interfaces*, 2016, **8**, 31716-  
1419 31721.
- 1420 55. X. Yang, Y. Yang, L. Fu, M. Zou, Z. Li, A. Cao and Q. Yuan, *Advanced Functional Materials*,  
1421 2018, **28**, 1704505.
- 1422 56. D. Ghim, Q. Jiang, S. Cao, S. Singamaneni and Y.-S. Jun, *Nano energy*, 2018, **53**, 949-  
1423 957.
- 1424 57. Z. Guo, G. Wang, X. Ming, T. Mei, J. Wang, J. Li, J. Qian and X. Wang, *ACS applied*  
1425 *materials & interfaces*, 2018, **10**, 24583-24589.
- 1426 58. W. Zhang, W. Zhu, S. Shi, N. Hu, Y. Suo and J. Wang, *Journal of Materials Chemistry A*,  
1427 2018, **6**, 16220-16227.
- 1428 59. D. Ding, W. Huang, C. Song, M. Yan, C. Guo and S. Liu, *Chemical Communications*, 2017,  
1429 **53**, 6744-6747.
- 1430 60. R. Chen, Z. Wu, T. Zhang, T. Yu and M. Ye, *RSC Advances*, 2017, **7**, 19849-19855.

- 1431 61. J. Wang, Y. Li, L. Deng, N. Wei, Y. Weng, S. Dong, D. Qi, J. Qiu, X. Chen and T. Wu, *Advanced Materials*, 2017, **29**, 1603730.  
1432
- 1433 62. X. Chen, L. Liu, Y. Y. Peter and S. S. Mao, *Science*, 2011, **331**, 746-750.  
1434 63. X. Liu, G. Zhu, X. Wang, X. Yuan, T. Lin and F. Huang, *Advanced Energy Materials*, 2016,  
1435 **6**, 1600452.
- 1436 64. M. Gao, L. Zhu, C. K. Peh and G. W. Ho, *Energy & Environmental Science*, 2019.  
1437 65. S. M. Sajadi, N. Farokhnia, P. Irajizad, M. Hasnain and H. Ghasemi, *Journal of Materials  
1438 Chemistry A*, 2016, **4**, 4700-4705.
- 1439 66. C. Chen, Y. Li, J. Song, Z. Yang, Y. Kuang, E. Hitz, C. Jia, A. Gong, F. Jiang and J. Zhu,  
1440 *Advanced materials*, 2017, **29**, 1701756.
- 1441 67. F. Jiang, H. Liu, Y. Li, Y. Kuang, X. Xu, C. Chen, H. Huang, C. Jia, X. Zhao and E. Hitz,  
1442 *ACS applied materials & interfaces*, 2017, **10**, 1104-1112.
- 1443 68. P. Mu, Z. Zhang, W. Bai, J. He, H. Sun, Z. Zhu, W. Liang and A. Li, *Advanced Energy  
1444 Materials*, 2019, **9**, 1802158.
- 1445 69. X. Zhou, F. Zhao, Y. Guo, Y. Zhang and G. Yu, *Energy & Environmental Science*, 2018,  
1446 **11**, 1985-1992.
- 1447 70. X. Feng, J. Zhao, D. Sun, L. Shanmugam, J.-K. Kim and J. Yang, *Journal of Materials  
1448 Chemistry A*, 2019.
- 1449 71. H. Ren, M. Tang, B. Guan, K. Wang, J. Yang, F. Wang, M. Wang, J. Shan, Z. Chen and  
1450 D. Wei, *Advanced materials*, 2017, **29**, 1702590.
- 1451 72. X. Hu, W. Xu, L. Zhou, Y. Tan, Y. Wang, S. Zhu and J. Zhu, *Advanced materials*, 2017,  
1452 **29**, 1604031.
- 1453 73. A. Guo, X. Ming, Y. Fu, G. Wang and X. Wang, *ACS applied materials & interfaces*, 2017,  
1454 **9**, 29958-29964.
- 1455 74. Y. Liu, J. Chen, D. Guo, M. Cao and L. Jiang, *ACS applied materials & interfaces*, 2015,  
1456 **7**, 13645-13652.
- 1457 75. S. Tadepalli, H. Hamper, S. H. Park, S. Cao, R. R. Naik and S. Singamaneni, *ACS  
1458 Biomaterials Science & Engineering*, 2016, **2**, 1084-1092.
- 1459 76. Y. Wang, C. Wang, X. Song, S. K. Megarajan and H. Jiang, *Journal of Materials Chemistry  
1460 A*, 2018, **6**, 963-971.
- 1461 77. P. Zhang, J. Li, L. Lv, Y. Zhao and L. Qu, *ACS nano*, 2017, **11**, 5087-5093.  
1462 78. Y. Li, T. Gao, Z. Yang, C. Chen, W. Luo, J. Song, E. Hitz, C. Jia, Y. Zhou and B. Liu,  
1463 *Advanced Materials*, 2017, **29**, 1700981.
- 1464 79. H. Yang, Z. Li, B. Lu, J. Gao, X. Jin, G. Sun, G. Zhang, P. Zhang and L. Qu, *ACS nano*,  
1465 2018, **12**, 11407-11416.
- 1466 80. C. Wang, Y. Wang, X. Song, M. Huang and H. Jiang, *Advanced Sustainable Systems*,  
1467 2019, **3**, 1800108.
- 1468 81. D. Hao, Y. Yang, B. Xu and Z. Cai, *Applied Thermal Engineering*, 2018, **141**, 406-412.  
1469 82. X. Huang, Y.-H. Yu, O. L. de Llergo, S. M. Marquez and Z. Cheng, *RSC Advances*, 2017,  
1470 **7**, 9495-9499.
- 1471 83. L. Zhang, B. Tang, J. Wu, R. Li and P. Wang, *Advanced Materials*, 2015, **27**, 4889-4894.  
1472 84. F. Zhao, X. Zhou, Y. Shi, X. Qian, M. Alexander, X. Zhao, S. Mendez, R. Yang, L. Qu and  
1473 G. Yu, *Nature nanotechnology*, 2018, **13**, 489.
- 1474 85. Y. Wang, C. Wang, X. Song, M. Huang, S. K. Megarajan, S. F. Shaikat and H. Jiang,  
1475 *Journal of Materials Chemistry A*, 2018, **6**, 9874-9881.
- 1476 86. X. Wu, G. Y. Chen, W. Zhang, X. Liu and H. Xu, *Advanced Sustainable Systems*, 2017,  
1477 **1**, 1700046.
- 1478 87. D. Hao, Y. Yang, B. Xu and Z. Cai, *ACS Sustainable Chemistry & Engineering*, 2018, **6**,  
1479 10789-10797.
- 1480 88. X. Wu, L. Wu, J. Tan, G. Y. Chen, G. Owens and H. Xu, *Journal of Materials Chemistry  
1481 A*, 2018, **6**, 12267-12274.

- 1482 89. L. Zong, M. Li and C. Li, *Nano energy*, 2018, **50**, 308-315.
- 1483 90. Q. Jiang, H. G. Derami, D. Ghim, S. Cao, Y.-S. Jun and S. Singamaneni, *Journal of Materials Chemistry A*, 2017, **5**, 18397-18402.
- 1484
- 1485 91. Y. Liu, K. Ai and L. Lu, *Chemical reviews*, 2014, **114**, 5057-5115.
- 1486 92. H. Gholami Derami, Q. Jiang, D. Ghim, S. Cao, Y. J. Chandar, J. J. Morrissey, Y.-S. Jun and S. Singamaneni, *ACS Applied Nano Materials*, 2019, **2**, 1092-1101.
- 1487
- 1488 93. M. Ye, J. Jia, Z. Wu, C. Qian, R. Chen, P. G. O'Brien, W. Sun, Y. Dong and G. A. Ozin, *Advanced Energy Materials*, 2017, **7**, 1601811.
- 1489
- 1490 94. L. Cui, P. Zhang, Y. Xiao, Y. Liang, H. Liang, Z. Cheng and L. Qu, *Advanced Materials*, 2018, **30**, 1706805.
- 1491
- 1492 95. Y. Yang, R. Zhao, T. Zhang, K. Zhao, P. Xiao, Y. Ma, P. M. Ajayan, G. Shi and Y. Chen, *ACS nano*, 2018, **12**, 829-835.
- 1493
- 1494 96. X. Li, W. Xu, M. Tang, L. Zhou, B. Zhu, S. Zhu and J. Zhu, *Proceedings of the National Academy of Sciences*, 2016, **113**, 13953-13958.
- 1495
- 1496 97. K.-K. Liu, Q. Jiang, S. Tadepalli, R. Raliya, P. Biswas, R. R. Naik and S. Singamaneni, *ACS applied materials & interfaces*, 2017, **9**, 7675-7681.
- 1497
- 1498 98. L. Shi, Y. Wang, L. Zhang and P. Wang, *Journal of Materials Chemistry A*, 2017, **5**, 16212-16219.
- 1499
- 1500 99. X. Wang, Y. He, G. Cheng, L. Shi, X. Liu and J. Zhu, *Energy Conversion and Management*, 2016, **130**, 176-183.
- 1501
- 1502 100. Y. Wang, L. Zhang and P. Wang, *ACS Sustainable Chemistry & Engineering*, 2016, **4**, 1223-1230.
- 1503
- 1504 101. Z. Yin, H. Wang, M. Jian, Y. Li, K. Xia, M. Zhang, C. Wang, Q. Wang, M. Ma and Q.-s. Zheng, *ACS applied materials & interfaces*, 2017, **9**, 28596-28603.
- 1505
- 1506 102. X. Li, J. Li, J. Lu, N. Xu, C. Chen, X. Min, B. Zhu, H. Li, L. Zhou and S. Zhu, *Joule*, 2018, **2**, 1331-1338.
- 1507
- 1508 103. G. Xue, K. Liu, Q. Chen, P. Yang, J. Li, T. Ding, J. Duan, B. Qi and J. Zhou, *ACS applied materials & interfaces*, 2017, **9**, 15052-15057.
- 1509
- 1510 104. N. Xu, X. Hu, W. Xu, X. Li, L. Zhou, S. Zhu and J. Zhu, *Advanced Materials*, 2017, **29**, 1606762.
- 1511
- 1512 105. M. Zhu, J. Yu, C. Ma, C. Zhang, D. Wu and H. Zhu, *Solar Energy Materials and Solar Cells*, 2019, **191**, 83-90.
- 1513
- 1514 106. J. Fang, J. Liu, J. Gu, Q. Liu, W. Zhang, H. Su and D. Zhang, *Chemistry of Materials*, 2018, **30**, 6217-6221.
- 1515
- 1516 107. J. Wu, K. R. Zodrow, P. B. Szemraj and Q. Li, *Journal of Materials Chemistry A*, 2017, **5**, 23712-23719.
- 1517
- 1518 108. X. Wu, Q. Jiang, D. Ghim, S. Singamaneni and Y.-S. Jun, *Journal of Materials Chemistry A*, 2018, **6**, 18799-18807.
- 1519
- 1520 109. Y. Zeng, J. Yao, B. A. Horri, K. Wang, Y. Wu, D. Li and H. Wang, *Energy & Environmental Science*, 2011, **4**, 4074-4078.
- 1521
- 1522 110. Y. Li, T. Gao, Z. Yang, C. Chen, Y. Kuang, J. Song, C. Jia, E. M. Hitz, B. Yang and L. Hu, *Nano Energy*, 2017, **41**, 201-209.
- 1523
- 1524 111. F. S. Awad, H. D. Kiriachchi, K. M. AbouZeid, Ü. Özgür and M. S. El-Shall, *ACS Applied Energy Materials*, 2018, **1**, 976-985.
- 1525
- 1526 112. G. Wang, Y. Fu, A. Guo, T. Mei, J. Wang, J. Li and X. Wang, *Chemistry of Materials*, 2017, **29**, 5629-5635.
- 1527
- 1528 113. S. Ma, C. P. Chiu, Y. Zhu, C. Y. Tang, H. Long, W. Qarony, X. Zhao, X. Zhang, W. H. Lo and Y. H. Tsang, *Applied Energy*, 2017, **206**, 63-69.
- 1529
- 1530 114. L. Yi, S. Ci, S. Luo, P. Shao, Y. Hou and Z. Wen, *Nano Energy*, 2017, **41**, 600-608.
- 1531 115. R. Li, L. Zhang, L. Shi and P. Wang, *ACS Nano*, 2017, **11**, 3752-3759.

- 1532 116. S. Yu, Y. Zhang, H. Duan, Y. Liu, X. Quan, P. Tao, W. Shang, J. Wu, C. Song and T.  
1533 Deng, *Scientific reports*, 2015, **5**, 13600.
- 1534 117. L. Zhou, S. Zhuang, C. He, Y. Tan, Z. Wang and J. Zhu, *Nano Energy*, 2017, **32**, 195-200.
- 1535 118. Z. C. Xiong, Y. J. Zhu, D. D. Qin, F. F. Chen and R. L. Yang, *Small*, 2018, **14**, 1803387.
- 1536 119. J. Lou, Y. Liu, Z. Wang, D. Zhao, C. Song, J. Wu, N. Dasgupta, W. Zhang, D. Zhang and  
1537 P. Tao, *ACS applied materials & interfaces*, 2016, **8**, 14628-14636.
- 1538 120. J. Fang, Q. Liu, W. Zhang, J. Gu, Y. Su, H. Su, C. Guo and D. Zhang, *Journal of Materials  
1539 Chemistry A*, 2017, **5**, 17817-17821.
- 1540 121. S. Hong, Y. Shi, R. Li, C. Zhang, Y. Jin and P. Wang, *ACS applied materials & interfaces*,  
1541 2018, **10**, 28517-28524.
- 1542 122. M. Zhu, Y. Li, G. Chen, F. Jiang, Z. Yang, X. Luo, Y. Wang, S. D. Lacey, J. Dai and C.  
1543 Wang, *Advanced Materials*, 2017, **29**, 1704107.
- 1544 123. Q. Jiang and S. Singamaneni, *Joule*, 2017, **1**, 429-430.
- 1545 124. M. Keshavarz Hedayati and M. Elbahri, *Materials*, 2016, **9**, 497.
- 1546 125. C. Chen, Y. Kuang and L. Hu, *Joule*, 2019.
- 1547 126. X. Li, R. Lin, G. Ni, N. Xu, X. Hu, B. Zhu, G. Lv, J. Li, S. Zhu and J. Zhu, *National Science  
1548 Review*, 2017, **5**, 70-77.
- 1549 127. Y. Shi, R. Li, Y. Jin, S. Zhuo, L. Shi, J. Chang, S. Hong, K.-C. Ng and P. Wang, *Joule*,  
1550 2018, **2**, 1171-1186.
- 1551 128. C. Finnerty, L. Zhang, D. L. Sedlak, K. L. Nelson and B. Mi, *Environmental science &  
1552 technology*, 2017, **51**, 11701-11709.
- 1553 129. Y. Shi, C. Zhang, R. Li, S. Zhuo, Y. Jin, L. Shi, S. Hong, J. Chang, C. Ong and P. Wang,  
1554 *Environmental science & technology*, 2018, **52**, 11822-11830.
- 1555 130. G. Ni, S. H. Zandavi, S. M. Javid, S. V. Boriskina, T. A. Cooper and G. Chen, *Energy &  
1556 Environmental Science*, 2018, **11**, 1510-1519.
- 1557 131. Z. Liu, H. Song, D. Ji, C. Li, A. Cheney, Y. Liu, N. Zhang, X. Zeng, B. Chen and J. Gao,  
1558 *Global Challenges*, 2017, **1**, 1600003.
- 1559 132. Y. Xia, Q. Hou, H. Jubaer, Y. Li, Y. Kang, S. Yuan, H. Liu, L. Zhang, L. Gao and H. Wang,  
1560 *Energy & Environmental Science*, 2019.
- 1561 133. T. A. Cooper, S. H. Zandavi, G. W. Ni, Y. Tsurimaki, Y. Huang, S. V. Boriskina and G.  
1562 Chen, *Nature communications*, 2018, **9**, 5086.
- 1563 134. Y. Kuang, C. Chen, S. He, E. M. Hitz, Y. Wang, W. Gan, R. Mi and L. Hu, *Advanced  
1564 Materials*, 2019, 1900498.
- 1565 135. J. Zhao, Y. Yang, C. Yang, Y. Tian, Y. Han, J. Liu, X. Yin and W. Que, *Journal of Materials  
1566 Chemistry A*, 2018, **6**, 16196-16204.
- 1567 136. W. Xu, X. Hu, S. Zhuang, Y. Wang, X. Li, L. Zhou, S. Zhu and J. Zhu, *Advanced Energy  
1568 Materials*, 2018, **8**, 1702884.
- 1569 137. Y. Yang, H. Zhao, Z. Yin, J. Zhao, X. Yin, N. Li, D. Yin, Y. Li, B. Lei and Y. Du, *Materials  
1570 Horizons*, 2018, **5**, 1143-1150.
- 1571 138. S. Gao, X. Dong, J. Huang, J. Dong, F. D. Maggio, S. Wang, F. Guo, T. Zhu, Z. Chen and  
1572 Y. Lai, *Global Challenges*, 2019, 1800117.
- 1573 139. L. Zhu, M. Gao, C. K. N. Peh, X. Wang and G. W. Ho, *Advanced Energy Materials*, 2018,  
1574 **8**, 1702149.
- 1575 140. Y. Ito, Y. Tanabe, J. Han, T. Fujita, K. Tanigaki and M. Chen, *Advanced Materials*, 2015,  
1576 **27**, 4302-4307.
- 1577 141. B. Su, Y. Tian and L. Jiang, *Journal of the American Chemical Society*, 2016, **138**, 1727-  
1578 1748.
- 1579 142. D. Attinger, C. Frankiewicz, A. R. Betz, T. M. Schutzius, R. Ganguly, A. Das, C.-J. Kim  
1580 and C. M. Megaridis, *MRS Energy & Sustainability*, 2014, **1**.
- 1581 143. Z. Wang, M. Elimelech and S. Lin, *Environmental science & technology*, 2016, **50**, 2132-  
1582 2150.

- 1583 144. N. Miljkovic and E. N. Wang, *MRS bulletin*, 2013, **38**, 397-406.
- 1584 145. D. E. Kim, H. S. Ahn and T.-S. Kwon, *Applied Thermal Engineering*, 2017, **110**, 412-423.
- 1585 146. J. Zhong, C. Huang, D. Wu and Z. Lin, *International Journal of Heat and Mass Transfer*, 2019, **128**, 860-864.
- 1586
- 1587 147. D. K. Nandakumar, Y. Zhang, S. K. Ravi, N. Guo, C. Zhang and S. C. Tan, *Advanced Materials*, 2019, 1806730.
- 1588
- 1589 148. E.-P. Ng and S. Mintova, *Microporous and Mesoporous Materials*, 2008, **114**, 1-26.
- 1590 149. J. Canivet, A. Fateeva, Y. Guo, B. Coasne and D. Farrusseng, *Chemical Society Reviews*, 2014, **43**, 5594-5617.
- 1591
- 1592 150. H. Kim, S. Yang, S. R. Rao, S. Narayanan, E. A. Kapustin, H. Furukawa, A. S. Umans, O. M. Yaghi and E. N. Wang, *Science*, 2017, **356**, 430-434.
- 1593
- 1594 151. N. C. Burtch, H. Jasuja and K. S. Walton, *Chemical reviews*, 2014, **114**, 10575-10612.
- 1595 152. S. Zhang, J. Huang, Z. Chen and Y. Lai, *Small*, 2017, **13**, 1602992.
- 1596 153. H. Zhu, Z. Guo and W. Liu, *Chemical communications*, 2016, **52**, 3863-3879.
- 1597 154. K.-C. Park, P. Kim, A. Grinthal, N. He, D. Fox, J. C. Weaver and J. Aizenberg, *Nature*, 2016, **531**, 78.
- 1598
- 1599 155. Y. Zheng, H. Bai, Z. Huang, X. Tian, F.-Q. Nie, Y. Zhao, J. Zhai and L. Jiang, *Nature*, 2010, **463**, 640.
- 1600
- 1601 156. M. Zhang and Y. Zheng, *Materials Today: Proceedings*, 2016, **3**, 696-702.
- 1602 157. X. Tian, H. Bai, Y. Zheng and L. Jiang, *Advanced Functional Materials*, 2011, **21**, 1398-1402.
- 1603
- 1604 158. H. Dong, N. Wang, L. Wang, H. Bai, J. Wu, Y. Zheng, Y. Zhao and L. Jiang, *ChemPhysChem*, 2012, **13**, 1153-1156.
- 1605
- 1606 159. H. Bai, R. Sun, J. Ju, X. Yao, Y. Zheng and L. Jiang, *small*, 2011, **7**, 3429-3433.
- 1607 160. A. R. Parker and C. R. Lawrence, *Nature*, 2001, **414**, 33.
- 1608 161. J. Guadarrama-Cetina, A. Mongruel, M.-G. Medici, E. Baquero, A. Parker, I. Milimouk-Melnychuk, W. González-Viñas and D. Beysens, *The European Physical Journal E*, 2014, **37**, 109.
- 1609
- 1610
- 1611 162. T. Nørgaard and M. Dacke, *Frontiers in zoology*, 2010, **7**, 23.
- 1612 163. E. Kostal, S. Stroj, S. Kasemann, V. Matylitsky and M. Domke, *Langmuir*, 2018, **34**, 2933-2941.
- 1613
- 1614 164. X. Zeng, L. Qian, X. Yuan, C. Zhou, Z. Li, J. Cheng, S. Xu, S. Wang, P. Pi and X. Wen, *ACS nano*, 2016, **11**, 760-769.
- 1615
- 1616 165. L. Zhai, M. C. Berg, F. C. Cebeci, Y. Kim, J. M. Milwid, M. F. Rubner and R. E. Cohen, *Nano Letters*, 2006, **6**, 1213-1217.
- 1617
- 1618 166. Z. Yu, F. F. Yun, Y. Wang, L. Yao, S. Dou, K. Liu, L. Jiang and X. Wang, *Small*, 2017, **13**, 1701403.
- 1619
- 1620 167. J. Wu, L. Zhang, Y. Wang and P. Wang, *Advanced Materials Interfaces*, 2017, **4**, 1600801.
- 1621 168. J. Ju, H. Bai, Y. Zheng, T. Zhao, R. Fang and L. Jiang, *Nature communications*, 2012, **3**, 1247.
- 1622
- 1623 169. X. Heng, M. Xiang, Z. Lu and C. Luo, *ACS applied materials & interfaces*, 2014, **6**, 8032-8041.
- 1624
- 1625 170. J. Ju, X. Yao, S. Yang, L. Wang, R. Sun, Y. He and L. Jiang, *Advanced Functional Materials*, 2014, **24**, 6933-6938.
- 1626
- 1627 171. M. Cao, J. Ju, K. Li, S. Dou, K. Liu and L. Jiang, *Advanced Functional Materials*, 2014, **24**, 3235-3240.
- 1628
- 1629 172. A. Deshmukh, C. Boo, V. Karanikola, S. Lin, A. P. Straub, T. Tong, D. M. Warsinger and M. Elimelech, *Energy Environ. Sci.*, 2018.
- 1630
- 1631 173. A. Alkudhiri, N. Darwish and N. Hilal, *Desalination*, 2012, **287**, 2-18.
- 1632 174. L. Martínez-Díez and M. Vázquez-González, *AIChE journal*, 1996, **42**, 1844-1852.
- 1633 175. F. E. Ahmed, R. Hashaikeh and N. Hilal, *Desalination*, 2019, **453**, 54-76.

- 1634 176. P. Westerhoff, P. Alvarez, Q. Li, J. Gardea-Torresdey and J. Zimmerman, *Environmental*  
1635 *Science: Nano*, 2016, **3**, 1241-1253.
- 1636 177. P. D. Dongare, A. Alabastri, S. Pedersen, K. R. Zodrow, N. J. Hogan, O. Neumann, J. Wu,  
1637 T. Wang, A. Deshmukh and M. Elimelech, *Proceedings of the National Academy of*  
1638 *Sciences*, 2017, **114**, 6936-6941.
- 1639 178. L. Camacho, L. Dumée, J. Zhang, J.-d. Li, M. Duke, J. Gomez and S. Gray, *Water*, 2013,  
1640 **5**, 94-196.
- 1641 179. Y.-S. Jun, X. Wu, D. Ghim, Q. Jiang, S. Cao and S. Singamaneni, *Accounts of Chemical*  
1642 *Research*, 2019.
- 1643 180. M. Fujiwara, *Desalination*, 2017, **404**, 79-86.
- 1644 181. M. Fujiwara and T. Imura, *ACS nano*, 2015, **9**, 5705-5712.
- 1645 182. M. Fujiwara and M. Kikuchi, *Water research*, 2017, **127**, 96-103.
- 1646 183. G. Xue, Q. Chen, S. Lin, J. Duan, P. Yang, K. Liu, J. Li and J. Zhou, *Global Challenges*,  
1647 2018, **2**, 1800001.
- 1648 184. E. Chiavazzo, M. Morciano, F. Viglino, M. Fasano and P. Asinari, *arXiv preprint*  
1649 *arXiv:1702.05422*, 2017.
- 1650 185. Y. Z. Tan, H. Wang, L. Han, M. B. Tanis-Kanbur, M. V. Pranav and J. W. Chew, *Journal*  
1651 *of Membrane Science*, 2018, **565**, 254-265.
- 1652 186. L. Huang, J. Pei, H. Jiang and X. Hu, *Desalination*, 2018, **442**, 1-7.
- 1653 187. X. Li, G. Ni, T. Cooper, N. Xu, J. Li, L. Zhou, X. Hu, B. Zhu, P. Yao and J. Zhu, *Joule*,  
1654 2019.
- 1655